Corso di Laurea Magistrale in Fisica

Università di Pisa

Dipartimento di Fisica
"Enrico Fermi"

Search for CP violation in $D^0 \to K^0_S K^0_S$ decays at LHCb

Candidato:
Lorenzo Pica

Relatore:
Prof. Giovanni Punzi

Anno Accademico 2018/2019

Ai miei genitori.

Contents

Introduction

CP is the discrete symmetry given by the combined application of the spatial parity (P) and the charge conjugation operation (C). CP is known to be a broken symmetry, at this could potentially explain the asymmetry between matter and anti-matter present in the Universe, as inferred from astronomical observations. The first experimental evidence for CP–violating effects (CPV) was found in weak transitions of the *strange* quark in year 1964, through precision measurements of the neutral kaon system. A crucial contribution to the understanding of CPV was given by the BaBar and the Belle experiments, that observed for the first time the presence of large CPV in transitions of another *down*–type quark, the *bottom*, confirming its description within the Standard Model through a single complex phase in the Cabibbo-Kobayashi-Maskawa (CKM) matrix, and providing accurate measurements of its elements.

However, CPV in decays of *up*–type quarks has remained elusive until very recently. Amongst them, only the *charm* quark offers concrete possibilities of observation of CPV effects, because the *up* quark only produces light mesons (like π^0 and η) that do not oscillate, while the *top* quark decays too quickly to form any meson states. But even in *charm* hadrons CPV is difficult to observe, due to the smallness of effects expected ($O \sim 10^{-3} - 10^{-4}$), that are not even precisely calculable. Only in March of this year CPV has finally been observed in the charm sector by the LHCb experiment at LHC, measuring the integrated decay asymmetry difference of $D^0 \to K^+K^-$ and $D^0 \to \pi^+\pi^-$ decays as $(-15.4 \pm 2.9) \times 10^{-4}$.

This event significantly boosted the interest in charm CPV measurements. The large observed value (at the upper end of the range of Standard Model expectations), gives hope that significant effects may be found also in other channels, and that precise enough measurements can be made to investigate this new field in detail. Hopefully this will help reducing model uncertainties and clarifying the theoretical picture, eventually leading to understanding if CPV in charm also fits within the successful CKM model, or is coming from a different source (possibly separate from *down*–type quarks).

One of the most promising candidates for further $\mathcal{A}^{CP}$ measurements is the $D^0 \to K^0_S K^0_S$ decay, as it is possible for $\mathcal{A}^{CP}$ to take particularly large values ($\simeq 1\%$). However, this is balanced by the greater experimental difficulty of this mode, due to the pair of long-lived neutral particles in the final state. This represents a particular challenge at LHCb because the detector was not designed with this aim in mind, and it is more tuned to shorter–lived decays of heavy flavored hadrons; K^0_S mesons often decay outside of the acceptance of the precision vertex detector of LHCb (VELO), resulting in inferior resolution and greater difficulty in triggering. However, the LHCb can count on a huge production of charm particles and excellent detector performance – that were the very reason for its success in achieving the first observation in the $D^0 \to K^+K^-$ and $D^0 \to \pi^+\pi^-$ modes – so it is worth investigating its potential also in this interesting mode.

The aim of my thesis is to look for ways to enhance the sensitivity of LHCb to this decay mode, both with currently available data and in view of the upcoming run to start in 2021, by exploiting the sample more fully than has been done in the past. I concentrated on the sizable sample collected by LHCb since 2017, that has not yet been analyzed by the experiment, and has some novel features. First, the online selection of this sample is different from the past, in that it has increased efficiency for those decays occurring outside the VELO acceptance ("Downstream" decays). While such samples have been used in past measurements, they have different features in this new samples that require different analysis methods; in addition, they represent a larger proportion of the sample, increasing their relative importance in the result. Moreover, it is in principle possible to further enhance their collection efficiency in future runs, which underlines the importance of determining the limits of their actual usability.

For this purpose I have introduced a novel analysis methodology tuned to the specifics of this particular decay. While a standard LHCb analysis procedure is to apply cuts to reject charm decays coming from the decay of a bottom hadron ("secondaries"), keeping only those promptly produced in the *pp* collision, I have studied the possibility of keeping also the secondaries in the analysis to increase the available yields. The motivation is that those selection cuts are much more inefficient in the $D^0 \rightarrow K^0_S K^0_S$ channel than in any other charm mode, due to the lower resolution caused by the lack of VELO information, causing a much larger loss of signal. Loosening the selection however brings together new difficulties that are absent in all other charm analyses in LHCb, that I had to tackle in my thesis work in order to prove this to be a viable strategy.

The most important issue is the additional asymmetry that affects secondary decays, due to the underlying production asymmetry of the bottom quark plus the cumulative effects of *CPV* in the bottom–hadron decays leading to the D^0 particle object of my study. To solve this problem, I have demonstrated the possibility of subtracting this confounding asymmetry by means of a special control sample of $D^0 \rightarrow K^+K^-$, collected by a dedicated trigger that had not been used before for this purpose. This required however to redesign completely the selection procedures of both samples to ensure the same proportion of secondaries, and evaluate and correct for the residual differences while keeping systematic uncertainties under control. In addition, the loss of information on the position of the vertex of origin of the D^0 decay also requires some changes in the approach to the measurement.

I conclude my work with an evaluation of the *CPV* resolution achievable with this new analysis approach, and a look at the prospects from future data taking runs.

Chapter 1

CP violation and charm

In this chapter I introduce the phenomenology of CP Violation in the Standard Model of particle physics, describing the three possible circumstances in which these effects arise. Then I focus on the CP violation in the charm sector and in the $D^0 \to K^0_S K^0_S$ decay.

1.1 *CP* symmetry

CP is a discrete symmetry given by the subsequent application of *P* and *C*. *P* is defined as the spatial parity and corresponds to the inversion of space handedness, transforming a system into its mirrored version (*e.g.* $\overrightarrow{x} \to -\overrightarrow{x}$ for a vector). *C* is the charge conjugation operation and it reverses every internal quantum number (*e.g.* $Q \to -Q$ for electric charge). The *CP* operation combines these effects, transforming a matter particle into an anti-matter one, and vice versa.
P and *C* symmetries are both completely violated by weak interactions, as was proven by Madame Wu in 1956 [42], with the discovery of *P* and *C* asymmetry effects in β-decay of ^{60}Co nuclei. Unlike weak interactions, strong and electromagnetic had never show any effect of *P* and *C* violation, despite several experimental searches.
After this experiment, instead of *P* and *C* individually, *CP* was assumed to be symmetry of the Universe. This remained true until 1964, when Cronin and Fitch discovered a violation of *CP* symmetry, in weak decays of K^0_L into pion pairs [24].
After this discovery *CP* Violation (*CPV*) has become one of the most appealing problems in physics. It gained attention when Sakharov proposed that *CPV* could explain the asymmetry between matter and anti-matter in the Universe that emerges from astronomical observations [36]. Since the observed *CPV* effects are too small to explain the significant asymmetry present in the Universe, this lead to the realization of multiple experiment and analyses during last decades, to search for new *CPV* sources.

1.2 The Cabibbo-Kobayashi-Maskawa matrix

The description of *CPV* was included within the Standard Model by Kobayashi and Maskawa, with the introduction in the description of the weak interaction of the Cabibbo-Kobayashi-Maskawa (CKM) matrix [21, 31]. This is a 3 x 3 unitary matrix, describing the coupling *W*-boson to quarks. Its presence is due to the discrepancy between weak-interaction and mass eigenstates and the CKM represents the base-changing matrix. In the mass eigenstates basis the interaction Lagrangian can be written as:

$$\mathcal{L}_{int} = -\frac{g_2}{\sqrt{2}} \, (\bar{u}_L, \bar{c}_L, \bar{t}_L) \, \gamma^\mu \, V_{CKM} \begin{pmatrix} d_L \\ s_L \\ b_L \end{pmatrix} \, W_\mu^\dagger \, + \, h.c. \tag{1.1}$$

The CKM matrix allows for *CP* asymmetry since it contains an irreducible complex phase in the process amplitude, that is non-invariant under *CP*. The phase is present because the matrix is a 3 x 3 (since it mixes three quark families), complex and unitary matrix and to describe it four parameters are necessary: three mixing angles (Eulero angles in the quark vectors space) and one complex phase.
The CKM matrix plays a central role in the SM, allowing to make a wide range of predictions and stringent tests on the theory; for these reasons several experiments were performed to determine its elements [38]. The current results give:

$$V_{CKM} = \begin{pmatrix} V_{ud} & V_{us} & V_{ub} \\ V_{cd} & V_{cs} & V_{cb} \\ V_{td} & V_{ts} & V_{tb} \end{pmatrix} =$$

$$= \begin{pmatrix} 0.97427 \pm 0.00014 & 0.22536 \pm 0.00061 & 0.00355 \pm 0.00015 \\ 0.22522 \pm 0.00061 & 0.97343 \pm 0.00015 & 0.0414 \pm 0.0012 \\ 0.00886^{+0.00033}_{-0.00032} & 0.0405^{+0.011}_{-0.0012} & 0.99914 \pm 0.00005 \end{pmatrix}$$

From the values of the matrix elements it is possible to discern the phenomenology of quark mixing. Diagonal elements take values close to one, so processes involving quarks of the same generation are always favored. Mixing between generations is not forbidden, as shown by the non-zero values of out-diagonal elements, but these processes happen less likely than processes between same family and with different probability for each transition. The probability to have a mix between the first and the second generation is $O\sim\ 10^{-1}$, bigger than the one to have a transition between the second and third ($O\sim\ 10^{-2}$) and the first and the third generation ($O\sim\ 10^{-3}$).
This hierarchy between CKM matrix elements is manifest when it is expressed through the Wolfenstein parametrization [41], with the introduction of four parameters, called A, λ, ρ, η:

$$V_{CKM} \ = \begin{pmatrix} 1-\lambda^2/2 & \lambda & A\lambda(\rho - i\eta) \\ -\lambda & 1-\lambda^2/2 & A\lambda^2 \\ A\lambda^3(1-\rho-i\eta) & -A\lambda^2 & 1 \end{pmatrix} + O(\lambda^4)$$

where λ is the expansion parameter, related to the Cabibbo angle ($\sin(\theta_c) = 0.232 \pm 0.002$).

1.3 Types of *CP* violation

To discuss the different types of *CP* violation and the related observables it is useful to introduce some definitions. M represents any charged or neutral hadron, and $\bar{M}$ is its *CP* conjugate state. These hadrons can decay into a multi-particle final state $|f\rangle$ or its *CP*-conjugate $|\bar{f}\rangle$. The amplitudes that describe these processes are defined as:

$$A_f = \langle f|\mathcal{H}|M\rangle, \quad \bar{A}_f = \langle f|\mathcal{H}|\bar{M}\rangle$$

$$A_{\bar{f}} = \langle \bar{f}|\mathcal{H}|M\rangle, \qquad \bar{A}_{\bar{f}} = \langle \bar{f}|\mathcal{H}|\bar{M}\rangle$$

where $\mathcal{H}$ is the weak interactions Lagrangian. For processes involving charged-mesons or baryons, *CP*-violating observables can be defined in terms of these amplitudes, through the ratio $|\bar{A}_{\bar{f}}/A_f|$.
In case of neutral flavored mesons the situation is different because of the possibility for these particles to oscillate between the two *CP*-conjugate states in a mixing process. Mixing is the phenomenon where a particle, produced as a flavor eigenstate (*e.g.* M) propagate as a superposition of M and $\bar{M}$,. This is due to the non-correspondence between flavor and mass eigenstates. Mass eigenstates $|M_1\rangle$ and $|M_2\rangle$ can be written as:

$$|M_1\rangle = p|M\rangle + q|\bar{M}\rangle$$

$$|M_2\rangle = p|M\rangle - q|\bar{M}\rangle$$

where p and q are the probabilities to find one *CP*-eigenstate or the other (*CPT* invariance is here assumed). Therefore a particle, produced with a given flavor (*e.g.* M), propagating as a mass eigenstate can be revealed as its *CP*-conjugated state, $\bar{M}$. In this case the parameter, similar to the one already shown, that allows to express *CP*-violating observables is $\lambda_f = (q/p)(\bar{A}_{\bar{f}}/A_f)$.
As already said the existence of *CPV* is due to the complex phase present in the CKM matrix. It is important to notice that this is not the only phase contributing to the decay process: in the decay amplitude those coming from amplitude contribution given by weak interaction change sign under *CP* application, but additional phases appear in decay amplitudes, usually due to final state strong interaction; these do not change sign under *CP* application.
It is useful to write the decay amplitude making explicit the presence of the two phases:

$$A_f = \sum_i |a_i|\, e^{i(\delta_i + \phi_i)}, \quad \bar{A}_{\bar{f}} = \sum_i |a_i|\, e^{i(\delta_i - \phi_i)} \tag{1.2}$$

where i runs over different processes that contribute to the decay, a_i are the process amplitudes, δ_i are the strong phases and ϕ_i are the weak phases.

1.3.1 *CPV* in the decay

The first analyzed type of *CPV* violation is the one that occurs in the decay of a particle (also defined as direct *CPV*), in particular this is the one that intervenes in the process considered in this work, the $D^0 \to K^0_S K^0_S$ decay. It is useful here to consider the decay of two *CP*-conjugated states decaying into the same final state, *CP* eigenstate: $M \to f$ and $\bar{M} \to f$. The *CPV* takes place when the magnitude of the two *CP*-conjugated amplitudes is not equal:

$$|\bar{A}_f/A_f| \neq 1 \tag{1.3}$$

and experimentally leads to a different probability for M and $\bar{M}$ to decay into a final state $|f\rangle$.
Since all observables are related to squared decay amplitude, single phases are not observable and only phase differences causes measurable effects. For this reason to have $|\bar{A}_f/A_f| \neq 1$ it is necessary to have at least two different processes that contributes to the

decay, with different weak and strong phases. If this occurs an interference term arises that gives measurable effects:

$$|A_f|^2 - |\bar{A}_f|^2 = -2\sum_{l,k} |a_l|\,|a_k| \sin(\delta_l - \delta_k)\sin(\phi_l - \phi_k) \tag{1.4}$$

that, it can be noticed, is different from zero only if at least two different δ_i and ϕ_i are present.
The golden observable of direct *CPV* is the asymmetry between the time-integrated decay width of the two states decaying into $|f\rangle$:

$$\mathcal{A}^{CP}(f) = \frac{\Gamma(M \to f) - \Gamma(\bar{M} \to f)}{\Gamma(M \to f) + \Gamma(\bar{M} \to f)}$$

where Γ is proportional to the squared amplitude:

$$\Gamma(M \to f) \propto |A_f|^2, \quad \Gamma(M \to \bar{f}) \propto |A_{\bar{f}}|^2$$

Therefore $\mathcal{A}^{CP}$ can written as:

$$\mathcal{A}^{CP} = \frac{|A_f|^2 - |A_{\bar{f}}|^2}{|A_f|^2 + |A_{\bar{f}}|^2}$$

and defining:

$$R_f = \left|\frac{\bar{A}_f}{A_f}\right|$$

it is equal to:

$$\mathcal{A}^{CP} = \frac{1 - R_f^2}{1 + R_f^2} \tag{1.5}$$

1.3.2 *CPV* in mixing

The second source of *CPV* is the one that occurs only in processes involving neutral flavored mesons, through the mixing process. It is present when the probability for one state M to oscillate into its *CP*-conjugated state $\bar{M}$ ($\mathcal{P}(M \to \bar{M})$) is different from the probability of the opposite process ($\mathcal{P}(\bar{M} \to M)$).
This is summarized in the adopted formalism by the condition:

$$|q/p| \neq 1 \tag{1.6}$$

The *CP* asymmetry can be measured in this case exploiting the charged-current semileptonic neutral meson decays $M, \bar{M} \to l^{\pm}X$, where the flavor of the decaying meson can be tagged trough the sign of the lepton present in the decay. The observable that allows to measure the *CP* asymmetry is based on the "wrong-sign" decays, given by the oscillations:

$$\mathcal{A}^{CP}(t) = \frac{d\Gamma/dt[\bar{M}_{phys}(t) \to l^+X] - d\Gamma/dt[M_{phys}(t) \to l^-X]}{d\Gamma/dt[\bar{M}_{phys}(t) \to l^+X] + d\Gamma/dt[M_{phys}(t) \to l^-X]} \tag{1.7}$$

where M_{phys} and $\bar{M}_{phys}$ are the mass eigenstates. This, similarly as done before, can be expressed as:

$$\mathcal{A}^{CP}(t) = \frac{1 - R_m^2}{1 + R_m^2} \tag{1.8}$$

defining:

$$R_m = \left|\frac{q}{p}\right|^2 \tag{1.9}$$

1.3.3 *CPV* in the interference

The last possible manifestation of *CPV* is given by the interference between the decay of M to a given final state f through direct decay or through mixing, where M oscillates to $\bar{M}$ and this state decays into f. Therefore this type of *CPV* is present only when M and $\bar{M}$ can both decay to a common final state f. The asymmetry corresponds to having a different probability between the two possible decays: $\mathcal{P}(M \to f) \neq \mathcal{P}(M \to \bar{M} \to f)$.
The necessary condition for this type of *CPV*, adopting the already defined variables is:

$$arg(\lambda_f) + arg(\lambda_{\bar{f}}) \neq 0$$

that in case the final state f is a *CP* eigenstate can be written as:

$$\mathcal{I}m(\lambda_f) \neq 0$$

Here the *CP*-asymmetry can be measured, for example, through the neutral meson decays into *CP*-eigenstate final states:

$$\mathcal{A}^{CP}(t) = \frac{d\Gamma/dt[\bar{M}_{phys}(t) \to f_{CP}] - d\Gamma/dt[M_{phys}(t) \to f_{CP}]}{d\Gamma/dt[\bar{M}_{phys}(t) \to f_{CP}] + d\Gamma/dt[M_{phys}(t) \to f_{CP}]} \tag{1.10}$$

1.4 The charm sector

The study of *CP* asymmetry in c-hadrons (particles containing at least one charm quark) is particularly interesting, since it provides the possibility to measure *CP* asymmetry effects in the decay of an up-type quark. This is only possible for the charm quark, because the two other up-type quarks do not provide any experimental useful observable, for different reasons: the up quark in the adronization creates π^0, that is a *CP* eigenstate, and the top quark decays before adronization.
This motivated multiple searches for *CPV* in several processes involving c-hadrons, but despite these, any evidence for *CPV* in the charm sector remained unobserved for decades, while the presence of *CP* asymmetries in down-quark systems (beauty and strange mesons) was a well-established fact since the *CPV* discovery.
The situation has changed only in March of this year, when the LHCb collaboration measured for the first time *CP* violation in the decay of a charm hadron, with a statistical significance larger than 5 standard deviations [9].

1.5 *CP* violation observation in D^0 decay

For the purpose of this analysis it is useful and interesting to briefly summarize how the measurement was performed and the result that has been achieved.
The measurement is performed on pp collisions, produced by LHC at a center of mass energy of 13 TeV, for a total integrated luminosity of 5.9 fb^{-1}. About 55 millions $D^0 \to K^+K^-$ and 17 millions $D^0 \to \pi^+\pi^-$ events were reconstructed by LHCb. The *CPV* has been observed in the observable:

$$\Delta\mathcal{A}^{CP} = \mathcal{A}^{CP}(K^+K^-) - \mathcal{A}^{CP}(\pi^+\pi^-) \tag{1.11}$$

where $\mathcal{A}^{CP}$ (K^+K^-) and $\mathcal{A}^{CP}$ $(\pi^+\pi^-)$ are the time-integrated *CP* asymmetries for decay in brackets. In these asymmetries the dominant contribution is the direct one, and $\Delta\mathcal{A}^{CP}$

corresponds with good approximation to $\Delta\mathcal{A}^{\rm dir} = \mathcal{A}^{\rm dir}(K^+K^-) - \mathcal{A}^{\rm dir}(\pi^+\pi^-)$, where $\mathcal{A}^{\rm dir}$ is the $\mathcal{A}^{CP}$ contribution given by the *CPV* that appears in the decay.
$\mathcal{A}^{CP}$ can be experimentally measured through the asymmetry between the number of D^0 and $\bar{D}^0$ decaying into the same final state f[1]. Therefore, to measure $\Delta\mathcal{A}^{CP}$ it is necessary to identify the flavor of the D^0 present in each event. This was inferred exploiting two particular decay chains through which D^0 is produced. The first is the one where the D^0 comes from a $D^*(2010) \to D^0\pi$ strong decay; here the sign of the pion can be used to extrapolate the D^0 flavor (π-tagged events). The other possibility is the $B \to D^0\mu\nu_\mu X$ decay, where a b-hadron produces a D^0 with a semileptonic decay, together with other products X, a neutrino and a muon, which sign can be used to determine the D^0 flavor (μ-tagged events). With this strategy it is possible to calculate the raw asymmetry ($\mathcal{A}^{raw}$), that is the asymmetry between the number of D^0 and $\bar{D}^0$ decaying into the same final state. This is done separately between π-tagged and μ-tagged events, with:

$$\mathcal{A}_{\rm raw}^{\pi-\rm tagged}(f) = \frac{N(D^{*+}(f) \to D^0\pi^+) - N(D^{*-}(f) \to \bar{D}^0\pi^-)}{N(D^{*+}(f) \to D^0\pi^+) + N(D^{*-}(f) \to \bar{D}^0\pi^-)} \tag{1.12}$$

$$\mathcal{A}_{\rm raw}^{\mu-\rm tagged}(f) = \frac{N(\overline{B} \to D^0(f)\mu^-\overline{\nu}_\mu X) - N(B \to \bar{D}^0\mu^+\nu_\mu X)}{N(\overline{B} \to D^0(f)\mu^-\overline{\nu}_\mu X) + N(B \to \bar{D}^0\mu^+\nu_\mu X)} \tag{1.13}$$

where the $D^*(2010)$ is expressed here as D^{*+} and D^{*-}.
These quantities do not directly correspond to $\mathcal{A}^{CP}$. In an environment as LHCb these asymmetries receive three different contributions:

$$\mathcal{A}_{\rm raw}^{\pi-\rm tagged}(f) \simeq \mathcal{A}^{CP}(f) + \mathcal{A}^{det}(\pi) + \mathcal{A}^{prod}(D^*) \tag{1.14}$$

$$\mathcal{A}_{\rm raw}^{\mu-\rm tagged}(f) \simeq \mathcal{A}^{CP}(f) + \mathcal{A}^{det}(\mu) + \mathcal{A}^{prod}(B) \tag{1.15}$$

where $\mathcal{A}^{CP}(f)$ is the physical *CP*-asymmetry, $\mathcal{A}^{det}$ is the asymmetry given by the different detection efficiency for opposite-sign π and μ and $\mathcal{A}^{prod}$ is the asymmetry introduced by the different cross section values for D^{*+} and D^{*-} or B^+ and B^-, due to the not-neutral pp initial state.
$\Delta\mathcal{A}^{CP}$ is a golden observable since it can be extracted from the difference between the $\mathcal{A}^{raw}$ values, separately for π- and μ-tagged events. This is possible because of two reasons:

- detection and production asymmetries that contribute to $\mathcal{A}^{raw}$ are independent of the final state *f*, therefore in the difference between the $\mathcal{A}^{raw}$ values they cancel each other, allowing the determination $\Delta\mathcal{A}^{CP}$;
- on the other side, the expected values for the $D^0 \to K^+K^-$ and $D^0 \to \pi^+\pi^-$ *CP* asymmetries are of the same order, but opposite in sign [27], preventing any cancellation effect in the $\mathcal{A}^{raw}$ difference.

With this strategy it was possible to extract $\Delta\mathcal{A}^{CP}$ directly from the measured $\mathcal{A}^{raw}$ values:

$$\Delta\mathcal{A}^{CP} = \mathcal{A}^{raw}(K^+K^-) - \mathcal{A}^{raw}(\pi^+\pi^-) \tag{1.16}$$

The number of signal events tagged with opposite flavor are extracted fitting mass distributions for D^* and D^0 candidates for π- and μ-tagged events, respectively. The signal

[1] f indicates the final state in which the D^0 decays, K^+K^- or $\pi^+\pi^-$.

yields correspond approximately to 44 and 9 million events for the π- and μ- tagged $D^0 \to K^+K^-$ events, respectively and 14 and 3 million events for the π- and μ- tagged $D^0 \to \pi^+\pi^-$ events, respectively. The results obtained are:

$$\Delta\mathcal{A}_{CP}^{\pi-\text{tagged}} = [-18.2 \pm 3.2(\text{stat.}) \pm 0.9(\text{syst.})] \cdot 10^{-4} \tag{1.17}$$

$$\Delta\mathcal{A}_{CP}^{\mu-\text{tagged}} = [-9 \pm 8(\text{stat.}) \pm 5(\text{syst.})] \cdot 10^{-4} \tag{1.18}$$

and combining these results with previous LHCb results the final obtained $\Delta\mathcal{A}^{CP}$ value is:

$$\Delta\mathcal{A}^{CP} = (-15.4 \pm 2.9) \cdot 10^{-4} \tag{1.19}$$

which is different from zero for 5.3 standard deviations. This result represents the first observation of *CP* violation in the decay of charm hadron.

1.6 Implications of the observations

The result described in the previous section represents a milestone in experimental particle physics, but it can not be considered an endpoint. Much is still to be understood regarding *CPV* in charm.

The Standard Model predicts that the $\Delta\mathcal{A}^{CP}$ should assume a value that lies in the $10^{-4} - 10^{-3}$ range [20, 26, 28, 17, 19, 23]. The measurement result seems to be compatible with it, even if it lies at the upper end of the expected range and it is not possible to definitively say if the measurement agrees with SM prediction, since this has too large uncertainty. *CPV* measurements in charm decays, can be a significant probe for the presence of contributions form particles not included in the SM. These, in fact, can give a measurable effect in the loop present in the penguin amplitude that determines the arising of *CPV*. These contributions can enhance the *CPV* size, adding unexpected contributions to the loop in penguin amplitude and increasing its magnitude. Any discrepancy in these observables can reveal Beyond Standard Model (BSM) contributions.

To evaluate the level of agreement present between SM predictions and experimental measurements it is necessary to achieve an improvement in theoretical knowledge, in order to obtain more precise predictions. This is not a simple result to achieve, since in the considered processes low energy hadron interactions are always involved, that can be analyzed only through non-perturbative QCD dynamics [35, 37].

In this view the achievement of other *CPV* parameters measurement is extremely desirable, since these can add information in two different ways. Firstly they represent different checks through which it is possible to test more stringently the theory, in order to better understand the complex scenario of *CPV* in charm decays. In addition they may provide an help in refining theoretical prediction by multiple comparisons with several experimental observables.

An example is in [37] regarding $\mathcal{A}^{CP}$ predictions in charm decays. Here the direct *CP* asymmetry in the decay of a D^0 into two hadrons (hh) final state is written as:

$$\mathcal{A}^{CP}{}_{hh} = 2\lambda^4 \frac{p_{hh}}{T_{hh}} \sin(\delta)\sin(\phi) \tag{1.20}$$

where λ is the expansion parameter in the CKM Wolfenstein parametrization, p_{hh} and T_{hh} are the penguin and tree amplitudes, respectively, and δ and ϕ are the strong and

weak phases as defined before.
Since in the decay of charm hadrons the penguin contribution is expected to be very small ($\sim 1\%$) with respect to the tree diagram, it is possible to assume that the latter dominates. This allows to determine a relevant relation between the asymmetry and the branching ratio:

$$\mathcal{A}^{CP}{}_{hh} \propto \frac{1}{\sqrt{BR(hh)}} \tag{1.21}$$

This relation stands for each decay channel and allows to make predictions of unknown variables, starting from measured values of both branching ratio and *CP* asymmetry. From this point it is simple to understand the central role played by the first *CPV* measuerement in c-hadrons decay, and the importance of achieving other similar results, in different processes. For example this allows to make a more precise prediction for $\Delta\mathcal{A}^{CP}$. In [37] a value for $\mathcal{A}^{CP}$ (K^+K^-) is predicted:

$$\mathcal{A}^{CP}(K^+K^-) \approx 5.5 \cdot 10^{-4} \tag{1.22}$$

Through Eq. 1.21 it is possible to predict the $\mathcal{A}^{CP}$ value for other decay channels:

$$\mathcal{A}^{CP}(\pi^+\pi^-) \approx \mathcal{A}^{CP}(K^+K^-)\sqrt{2.8} = -9.2 \cdot 10^{-4} \tag{1.23}$$

Exploiting this it is possible to determine an expected value for $\Delta\mathcal{A}^{CP}$:

$$\Delta\mathcal{A}^{CP} = 14.7 \cdot 10^{-4} \tag{1.24}$$

with which $\Delta\mathcal{A}^{CP}$ measurement is compatible within one standard deviation. It should be noted that this prediction is based on approximation, assumed by the author in [37], that allowed to determine the penguin amplitude and then $\mathcal{A}^{CP}$ for K^+K^- channel, but it gives anyway a first important estimate for the theoretical value and an example on how experimental measurements can add significant information. With the addition of more measurements the number of bounds that can be used will increase and there is hope that prediction will become increasingly precise, allowing a significant comparison between theory and measurements.

1.7 *CP* violation in $D^0 \to K^0_S K^0_S$ decay

1.7.1 $\mathcal{A}^{CP}$ $(K^0_S K^0_S)$

In this view the measurement of $\mathcal{A}^{CP}$ in $D^0 \to K^0_S K^0_S$ decays plays a significant role. This because here the *CP* asymmetry could be enhanced by the processes involved in the decay to a value that can be as large as 1.1% at 95% C.L. [35]. Therefore, as it has been a major candidate for discovery of *CPV* in charm sector, now it is hoped to be an additional *CPV* observation in the same sector.
This motivated several searches that looked for *CPV* evidence in $D^0 \to K^0_S K^0_S$ decays [5, 25, 40, 18]. The current status is summarized in Table 1.1.
The work here performed will follow the same line of the presented results, searching for *CPV* in $D^0 \to K^0_S K^0_S$ decays through the measurement of time-integrated *CP* asymmetry, in data collected by LHCb in 2017.
It is necessary to describe the phenomenology of *CPV* in $D^0 \to K^0_S K^0_S$ decays. This channel is part of the so-called Singly-Cabibbo-Suppressed (SCS) D^0 decay modes, since its

$\mathcal{A}^{CP}$(%)	Yield	Year	Collaboration
-23 ± 19	65 ± 14	2008	CLEO
-2.9 ± 5.2 ± 2.2	627 ± 33	2015	LHCb Run-1
-0.02 ± 1.53 ± 0.17	5399 ± 87	2016	Belle
4.3 ± 3.4 ± 1.0	974 ± 43	2018	LHCb Run-2 (2015-16)
-0.38 ± 1.46	*	*	World average

Table 1.1: Previous $\mathcal{A}^{CP}$ measurements in $D^0 \to K^0_S K^0_S$ decays, taken from [18, 5, 40, 25].

decay amplitude is proportional to $V_{us}V^*_{cs}$ or $V_{ud}V^*_{cd}$. Other decay channels are classified as Cabibbo-Favored (CF) or Doubly-Cabibbo-Suppressed (DCS) when the amplitude includes a factor that is $V_{ud}V^*_{cs}$ or $V_{us}V^*_{cd}$, respectively.
Here *CP* asymmetry receives contributions from all three possible sources already analyzed, since it appears in a neutral- flavored-meson system. Since the expected values for the asymmetries contributions are small ($O \sim$ %), the time integrated *CP*-asymmetry can be written as sum of different terms:

$$\mathcal{A}^{CP} = \mathcal{A}^{\rm dir} + \mathcal{A}^{\rm ind}\frac{\langle t\rangle}{\tau} \tag{1.25}$$

The first term is the one given by the direct *CPV* that arises in the D^0 decay; it varies for different decay modes and it is time independent. The second term is the *indirect CP* asymmetry, given by the sum of mixing and interference contributions; it is decay mode-independent and depends on time. For this reason, in case of a time-integrated measurement its contribution is wighted by a factor, given by the average decay time in the sample ($\langle t\rangle$) divided by D^0 lifetime (τ).

1.7.2 $\mathcal{A}^{\rm dir}$ expectations

To explain in a clear way how the $\mathcal{A}^{\rm dir}$ prediction is extracted it is useful to introduce the *topological diagram* approach. This approach is based on the identification of relations between different decay modes, based on the definition of topological amplitudes describing D-decays. These amplitudes are classified in function of the topology of the weak decay that takes place. This approach is powerful for two main reasons: the identified relations allow to fit directly branching ratios to measurements to extract theoretical parameters and vice versa, these can be exploited to have information about unknown decay rates from the measured ones.
The topological amplitudes that can be identified are classified in two main groups: tree and penguin amplitudes, and weak annihilation amplitudes. The first one includes: color-allowed (T) and color-suppressed (C) tree amplitudes, where there is an external and internal W-emission respectively, QCD-penguin amplitude (P), color-favored (P_{EW}) and color-suppressed (P^C_{EW}) electro-weak penguin amplitudes and the singlet QCD-penguin amplitude (S). The second one includes: W-exchange (E) and W-annihilation (A) amplitudes, QCD-penguin exchange (PE) and QCD-penguin annihilation (PA) amplitudes, electro-weak penguin exchange (PE_{EW}) and electro-weak penguin annihilation (PA_{EW}) amplitudes. Schematic representation of these is shown in Figure 1.1.

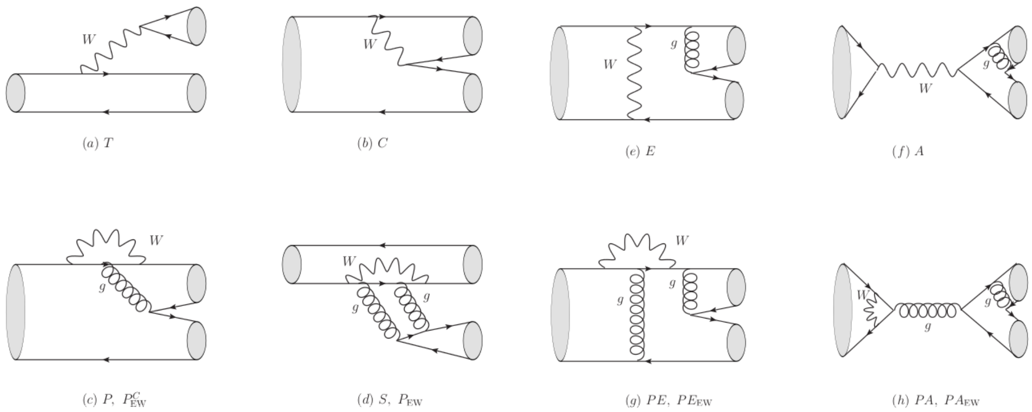

Figure 1.1: Possible D-decays representation through topological amplitudes. Taken from [22].

Adopting the topological diagram approach it is possible to write the decay amplitude for the $D^0 \to K^0_S K^0_S$ decay as [35]:

$$\frac{1}{2}[(\lambda_s - \lambda_d)\mathcal{A}_{sd} + \lambda_b \mathcal{A}_b] \tag{1.26}$$

where $\lambda_q = V^*_{cq} V_{uq}$ are the CKM matrix contribution to the amplitude and V_{ij} are CKM matrix elements. $\mathcal{A}_{sd}$ and $\mathcal{A}_b$ can be written in function topological amplitudes as:

$$\mathcal{A}_{sd} = \frac{E_1 + E_2 - E_3}{\sqrt{2}} \tag{1.27}$$

$$\mathcal{A}_b = \frac{2E + E_1 + E_2 + E_3 + PA}{\sqrt{2}} \tag{1.28}$$

E_1, E_2 and E_3 amplitudes represent processes that can proceed only through SU(3)-breaking. Their diagrams are reported in Figure 1.2.

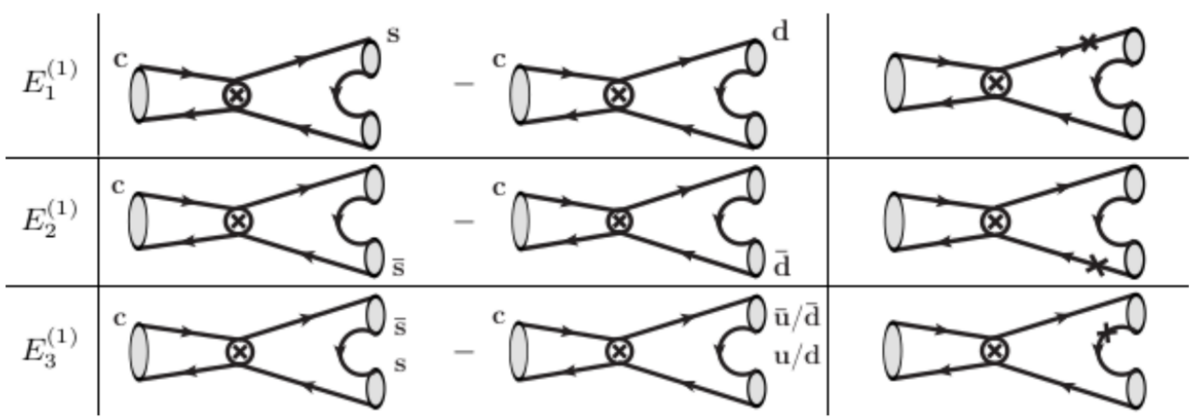

Figure 1.2: Topological amplitudes describing SU(3)-breaking processes. Taken from [34].

According to SM predictions *CPV* effects in this decay arise from the interference between $(\lambda_s - \lambda_d)\mathcal{A}_{sd}$ and $\lambda_b\mathcal{A}_b$ terms, that can be expressed as:

$$\mathcal{A}^{\mathrm{dir}} = \mathcal{I}m\frac{\lambda_b}{\lambda_s - \lambda_d}\mathcal{I}m\frac{\mathcal{A}_b}{\mathcal{A}_{sd}} \tag{1.29}$$

The first term comes from the CKM matrix elements and is equal to $\mathcal{I}m(\lambda_b/(\lambda_s - \lambda_d)) \sim 6 \cdot 10^{-4}$. It works as a suppression factor in *CP* asymmetry in charm decays and it shows why its measurement is so challenging. The second term in this channel can assume large values and suggests that *CP*-asymmetry can receive an enhancement, because of direct *CPV* contribution in $D^0 \to K^0_S K^0_S$ decays, represented by $\mathcal{A}^{\mathrm{dir}}$. An enhancement is possible because of the different processes contribution to $\mathcal{A}_{sd}$ and $\mathcal{A}_b$. $\mathcal{A}_{sd}$ goes only through SU(3)-breaking processes, as the ones represented by E_1, E_2 and E_3 amplitudes, that vanish in the SU(3) limit [34]. By contrast $\mathcal{A}_b$ also receives contributions from E and PA diagrams. Since these are not SU(3)-breaking processes, they do not vanish in the case of an exact SU(3) symmetry. It is this particular condition that makes the $D^0 \to K^0_S K^0_S$ decay channel so special, since *CP* asymmetry, given by direct contribution, can be significantly enhanced and can assume larger values with respect to other typical decay modes of charm hadrons.

1.7.3 $\mathcal{A}^{\mathrm{ind}}$ expectations

The second term that contributes to the $\mathcal{A}^{CP}$ is the indirect one. It can be expresses as:

$$\mathcal{A}^{\mathrm{ind}} = \mathcal{A}^{CP}{}_m + \mathcal{A}^{CP}{}_i \tag{1.30}$$

where $\mathcal{A}^{CP}{}_m$ and $\mathcal{A}^{CP}{}_i$ represent *CP* asymmetry in mixing and interference, respectively. $\mathcal{A}^{\mathrm{ind}}$ is proportional to $\mathcal{A}_\Gamma$, parameter that corresponds to the asymmetry between the effective D^0 and $\bar{D}^0$ decay widths :

$$\mathcal{A}^{\mathrm{ind}} = -\mathcal{A}_\Gamma \tag{1.31}$$

and

$$\mathcal{A}_\Gamma = \frac{\Gamma(D^0) - \Gamma(\bar{D}^0)}{\Gamma(D^0) + \Gamma(\bar{D}^0)} \tag{1.32}$$

Thanks to these relations and the knowledge on the $\mathcal{A}_\Gamma$ value it is possible to predict a value for indirect contribution to *CP* asymmetry. $\mathcal{A}_\Gamma$ has been measured to be $(-0.29 \pm 0.28) \cdot 10^{-3}$ [8, 2] and it is decay mode-independent. To correctly evaluate the $\mathcal{A}^{\mathrm{ind}}$ contribution it is necessary to take into account the $\langle t \rangle / \tau$. The average decay time on the D^0 depends on the experimental configuration; for LHCb it assumes a value that makes $\langle t \rangle / \tau$ to be $O \sim 1$.Therefore the $\mathcal{A}^{\mathrm{ind}}$ contribution assumes a value that is much smaller than the expected sensitivity of this analysis and it can be therefore neglected.
From the expected values for $\mathcal{A}^{\mathrm{dir}}$ and $\mathcal{A}^{\mathrm{ind}}$ it is simple to understand that for purposes of our analysis the time integrated *CP* asymmetry can be expressed as:

$$\mathcal{A}^{CP} \simeq \mathcal{A}^{\mathrm{dir}} \tag{1.33}$$

and $\mathcal{A}^{\mathrm{dir}}$ is the only contribution that will be take into account from here.

Before explaining how $\mathcal{A}^{CP}$ $(K^0_S K^0_S)$ measurement is performed in LHCb it is essential to discuss the general structure of the LHCb detector.

Chapter 2

The LHCb detector

In this chapter I will start briefly describing the CERN accelerator complex. Then I will focus my attention on LHCb, the only experiment located at the Large Hadron Collider designed for the analysis of the decays of heavy-flavor hadrons, describing both the detector and trigger system design.

2.1 The Large Hadron Collider

The Large Hadron Collider (LHC) is a circular hadron accelerator, located at CERN (*Conseil Européen pour la Recherche Nucléaire*) laboratories, near Geneva. It is located in a 27 km long circular tunnel, placed 100 m underground, across the France-Swiss border, where the Large Electron Positron collider (LEP) was previously housed. Along the circumference four major experiments are present: ALICE, ATLAS, CMS and LHCb. Particles move in the accelerator in two beams, circulating in opposite directions along the ring and made collide where experiments are located. The beams are not continuous, but organized in *bunches* of about 10^{11} particles each, equally time spaced for a multiple of 25 ns, producing a bunch-crossing rate of about 40 MHz. Beams are maintained in orbit through superconducting NbTi dipole magnets, keep at an operating temperature of 1.9 K through a liquid helium cooling system. To simultaneously bend two different beams, both composed of positive particles, in each magnet two different cavities are present, that provide a magnetic field of 8.3 T, with opposite direction. The LHC can accelerate protons and heavy ions and provide collisions between these in different data-taking periods. The maximum center-of-mass-energy (E_{cm}) at which the LHC can produce pp collision is 14 TeV. In the first two runs this energy has not been reached: the E_{cm} during Run 1 was equal to 7 TeV in 2010 and 2011 and to 8 TeV in 2012, during Run 2, in 2015-2018, the E_{cm} of collision was increased up to 13 TeV. These energies are not reached through a single acceleration process in the LHC; protons are extracted from hydrogen ionization and bring to the maximum energy through multiple accelerations, that take place in the CERN accelerator complex, shown in Figure 2.1.

The accelerator can provide an instantaneous luminosity $\mathcal{L} = 10^{34}\,\mathrm{cm}^{-2}\,\mathrm{s}^{-1}$. This high[1] $\mathcal{L}$ value allows the search for rare processes, one of the LHC main purposes, since the rate of a process is given by:

$$\frac{dN}{dt} = \mathcal{L} \times \sigma(\sqrt{s}) \tag{2.1}$$

[1] With respect to other hadron colliders.

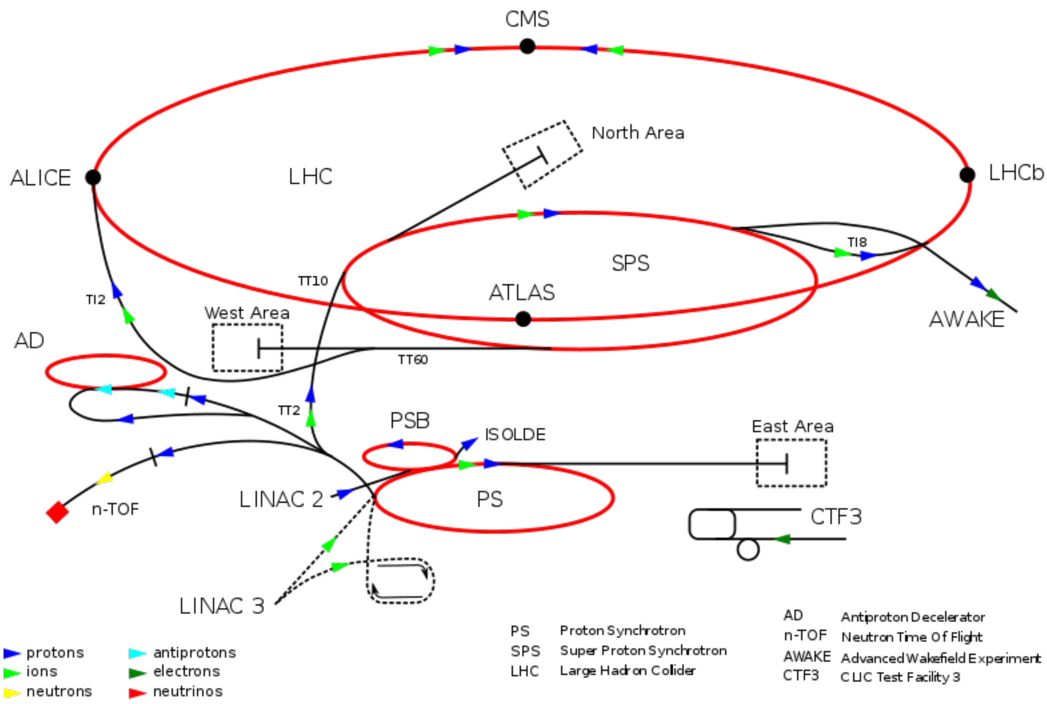

Figure 2.1: Schematic representation of CERN accelerator complex.

where $\sigma(\sqrt{s})$ is the cross section of the process at the center-of-mass energy $\sqrt{s}$. The $\mathcal{L}$ value is different at the LHCb interaction point, since it is focused on the study of charm and bottom hadrons, that are produced with higher rate than events interesting for other experiment. Because of the difference in processes cross section the nominal $\mathcal{L}$ value is counterproductive for the LHCb data taking, since it can cause high particle occupancy in the detector. For this reason in correspondence of the LHCb experiment the luminosity is reduced to a value of $(2-4)\cdot 10^{32}\,\mathrm{cm}^{-2}\,\mathrm{s}^{-1}$ moving the beams apart transversely and hence reducing their overlap at the collision. With this $\mathcal{L}$ the number of pp interactions per bunch crossing is reduced to less than 2.

2.2 The LHCb detector

LHCb is one of the four major experiments located along the LHC circumference. Its main purpose is the search for indirect evidence of physics Beyond the Standard Model. The search is performed measuring, with a precision never reached before, CP violation parameters and rare decays of charm and bottom hadrons. In fact, it is the only one focused, and specifically designed, to reveal particles composed by b and c quarks and study heavy-flavor physics.
It is a single arm forward spectrometer, with a forward angular coverage from approximately 10 mrad to 300 (250) mrad in the horizontal (vertical) plane, corresponding to a pseudorapidity[2] interval of $1.8 < \eta < 4.9$ [12]. This particular geometry makes LHCb complementary to other *general purpose* experiments located at LHC (for example CMS covers a pseudorapidity range $|\eta < 2.4|$) and furnishes a heavy-flavor particles produc-

[2]Pseudorapidity is defined as $\eta = -\log(\tan\theta/2)$ and θ is the angle between the particle flight direction and the beam axis.

tion rate never reached before. In fact, in an environment as LHC, b-hadrons are mainly produced in a parallel direction to the beams one, both forwardly and backwardly, in $b\bar{b}$ pairs *via* strong interactions, as shown in Figure 2.2. The LHCb geometrical acceptance covers most of the forward peak and allows to collect about 27% of the produced b hadrons. To perform b and c hadrons study, LHCb has two main necessities: it needs to

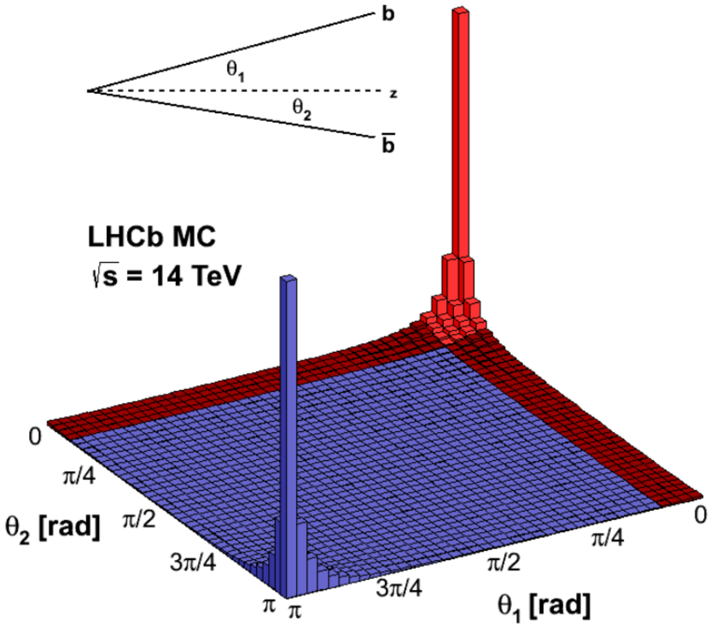

Figure 2.2: $b\bar{b}$ production cross section as a function of the polar angle of the two particles, with respect to the beam axis, in pp collisions simulated with PYTHIA. The LHCb acceptance is displayed in red.

measure with good precision momentum, and hence mass, of charged particles produced in the collisions and also to recognize all the different the kind of particles that flow in the apparatus. These two needs are filled by the two subsystems composing the LHCb detector: the tracking system and the particle identification system. The former is composed by a dipole magnet and three different detectors: the VErtex LOcator (VELO), the Tracker Turcensis (TT) and three tracking stations (T1-T3). The latter is composed by several detectors exploiting different technologies: two Ring Imaging Čerenkov (RICH), two calorimeters and the muon system, composed by five different detectors. These elements together constitute the entire LHCb detector, shown in Figure 2.3. The detector is equipped with a readout system, that communicates the measured quantities from each component, allowing the reconstruction of the event. It has a maximum rate corresponding to 1 MHz. Because of the difference between this and the LHC bunch-crossing rate, LHCb has to put a significant limit on the particle occupancy that can be managed. This was kept under control decreasing the $\mathcal{L}$ in the LHCb beams-intersection point, as explained before.

2.2.1 Tracking system

The LHCb tracking system main purpose is to measure with good precision the trajectory of charged particles (defined as tracks) produced in the pp interactions. Through these it

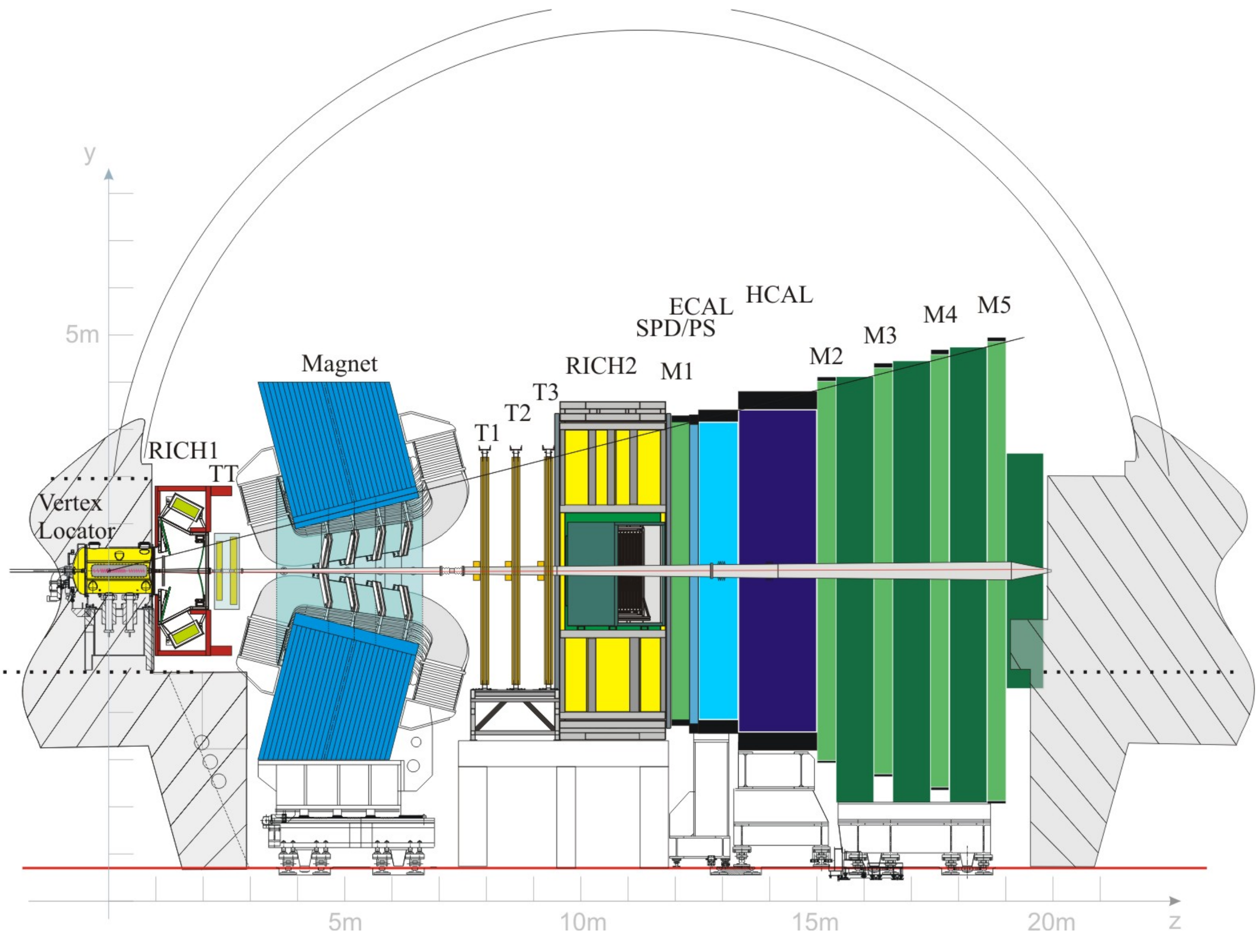

Figure 2.3: Schematic representation of the LHCb detector side view. A right-handed coordinate system is adopted in LHCb and shown: the x axis points toward the center of the LHC ring, the y axis point to upwards and the z axis coincides with the beam flight direction. Image taken from [12].

is possible to determine quantities as charge, vertex position and, with the presence of a magnetic field, particle momentum and mass.

Dipole magnet

The dipole magnet present in the detector bends the trajectories of charged particles, allowing the measurement of their momentum. It is a warm magnet, composed by two saddle-shaped coils, placed with a small angle with respect to the beam axis, in order to follow the LHCb angular acceptance; its structure can be seen in Figure 2.4. The magnet produces an approximately vertical magnetic field. Its intensity varies along the z-direction as it is shown in Figure 2.4 and it is measured before data-taking periods with Hall probes, since its precise knowledge is essential to have a good momentum and mass resolution. B_y has a maximum strength of 1.1 T and a total bending power of about 4 Tm. No tracking detectors are immersed in the magnetic field, but some of them are placed in a region where the B_y is different from zero. This happens for the nearer components, hence the VELO and mostly the tracking stations. The LHCb magnet has the possibility to reverse the direction of the magnetic field, feature absent

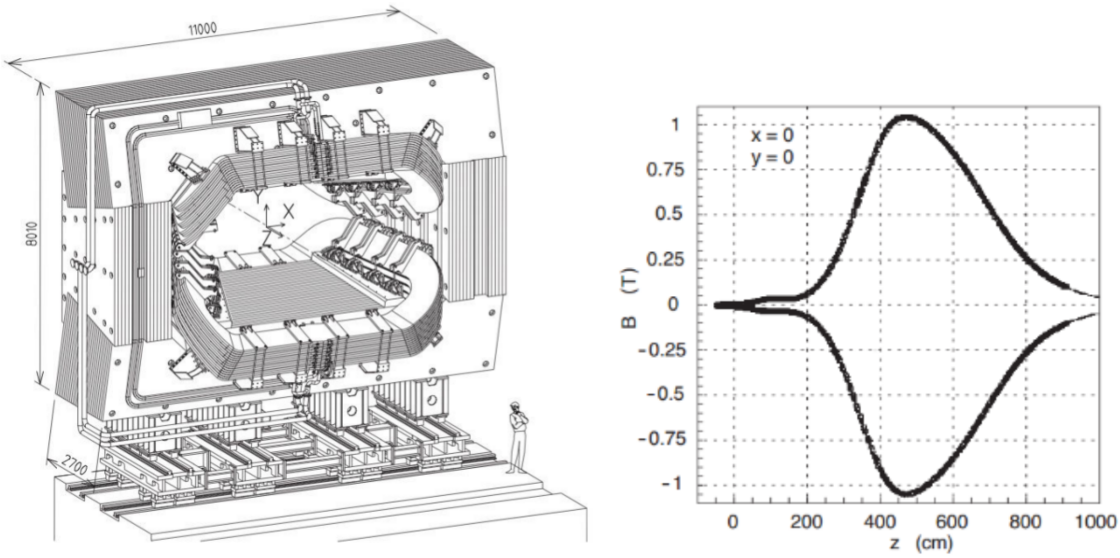

Figure 2.4: Representation of the LHCb dipole magnet structure on the left, lengths are in mm. On the right the variation of the magnetic field vertical component in function of the z coordinate. Figures taken from [12].

in the other LHC experiments. Therefore two data-taking configurations are present, with opposite magnet polarity, referred as *MagUp* and *MagDown*. In each configuration particles with a certain charge preferentially enter the detector acceptance, while the other with opposite charge are swap away from the magnet, and this can create large detection asymmetries. The presence of these asymmetries should be avoided collecting data in both configurations, if samples collected with opposite polarity has approximately the same size and the detector operating conditions are stable enough. This is done periodically switching the magnet polarity, indicatively every two weeks, during data-taking.

The Vertex Locator

The VErtex LOcator (VELO) [1] is the LHCb silicon-strip vertex detector. Its main purpose is to reveal the charged particle tracks close to the interaction point, allowing the measurement of the Primary Vertex (PV) position (pp interaction) and to reveal the presence of any displaced vertex. The latter is crucial for LHCb purposes, since it is the signature of an heavy-flavor hadron decay. These hadrons decay away from the interaction point because of their typical $c\tau$ values, that are $c\tau \sim 500\,\mu\text{m}$ and $c\tau \sim 100 - 300\,\mu\text{m}$, respectively for b-hadrons and neural, or charged, c-hadrons. To clearly distinguish primary and secondary vertexes the VELO has to reach a sensitivity similar to the $c\tau$ values.
The detector is composed by 21 disk-shaped silicon layers, positioned perpendicularly to the beam direction, each divided in two retractile halves, defined as modules. Its structure can be seen in Figure 2.5. Each module has two different series of silicon strip sensors in each face, with different geometry, one with radial (ϕ-sensors) and one with azimuthal (R-sensors) segmentation. Strips cover the region going from a radius of 8 mm to 42 mm from the disk center, for both geometrical configurations. The R-sensors are a series of azimuthal strips of constant radius, with a pitch that increases with radius, from 38 µm to

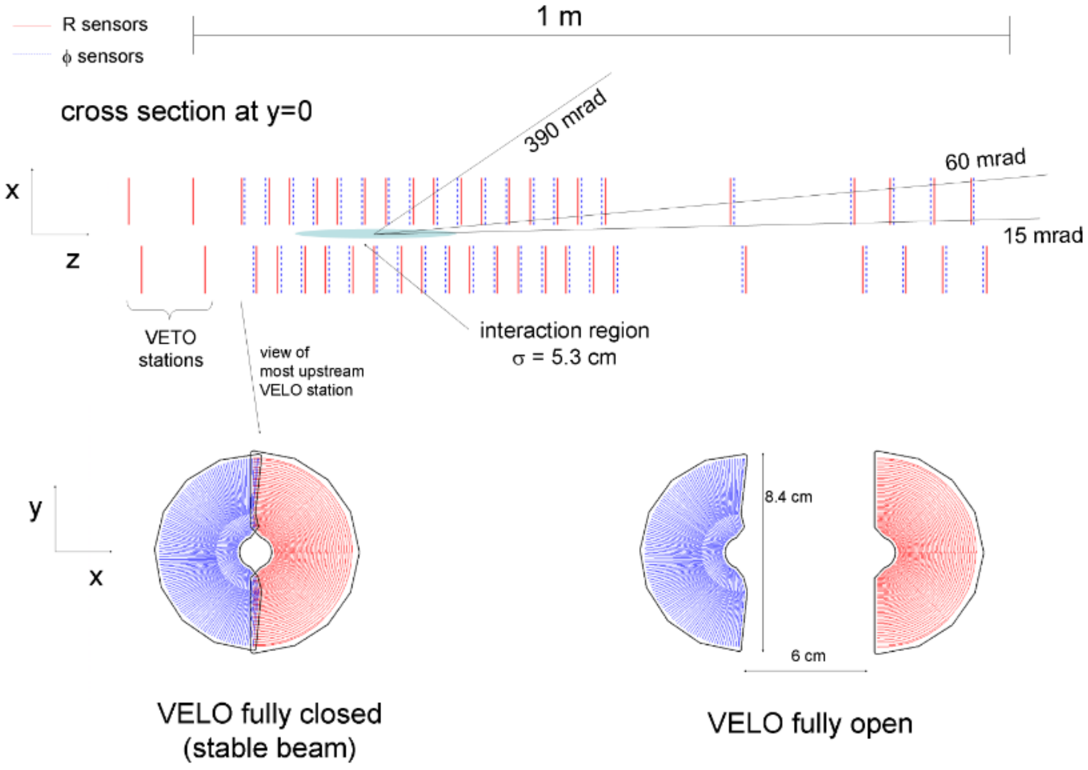

Figure 2.5: Representation of VELO structure. On top is present the (x,z)-plan view, where the modules position can be seen. On bottom the front-view of a modules pair is shown, in both close and open configurations.

101.6 μm. This pitch design allows a good-position measurement for the first track hits[3] and balances the occupancy between the inner and the outer region. The ϕ-sensors have a radial configuration and are divided in two concentric sections, the border is located at a radius equal to 17.25 mm. Also here the pitch increases radially from the center, with a discontinuity going from one region to the other. The module structure can be seen in Figure 2.6. With this configuration the VELO can provide a raw hit resolution equal to $\simeq 10 - 25\,\mu$m.

The modules can be damaged in case of high radiation and for this reason they can be moved away (open configuration). This happens, for example, of unstable beams during injection. In working configuration modules are then put closer (closed configuration) and partially overlap.

Each detector half is encased in an aluminum shielding case. This material was chosen because of its relatively small radiation length, in order to avoid deviation effects given by the interaction of particles with matter before detector crossing. The case has two purposes: it protects the VELO from the high-frequency electric field, given from the beam bunched structure, and it maintains the vacuum inside the detector. The two cases share the RF-foil, where they are merged, that has a highly corrugated structure, in order to allow the overlap of the two VELO halves when in working condition, as can be seen

[3] An hit is the measurement of the particle trajectory when it crosses one VELO module.

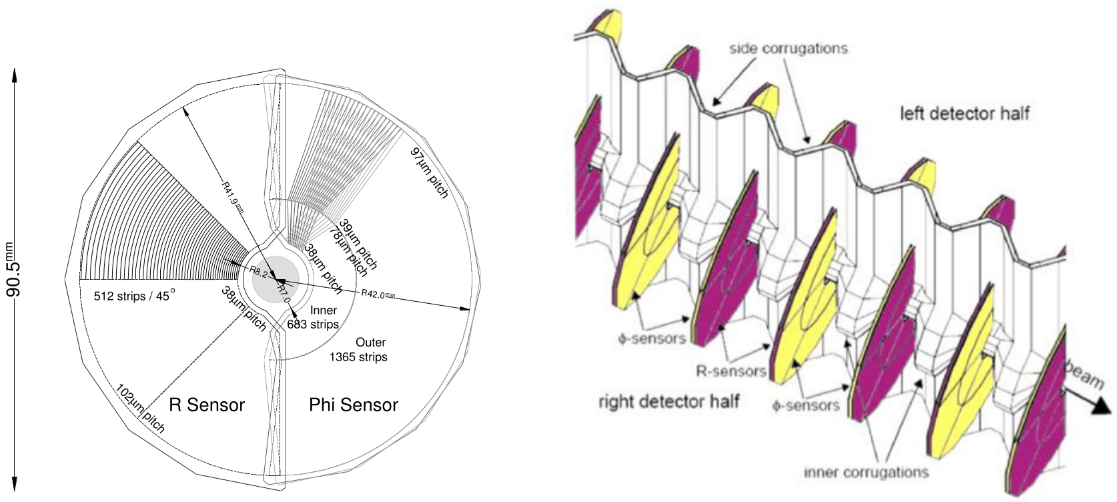

Figure 2.6: On the left representation of VELO modules silicon strip sensors, for both R- and ϕ-configurations. On the right the inner view of the RF-boxes, in closed working configuration; the cases edges are not represented to show the overlap between the modules. R- and ϕ-sensors are coloured in yellow and purple, respectively. Figures taken from [4].

in Figure 2.6.

Tracker Turcensis

The Tracker Turcensis (TT) is a silicon microstrip tracker [16]. It is located upstream the magnet, for two main purposes: it reconstructs the trajectories of low-momentum particles, that are deflected from the detector acceptance by the magnet and can not be reconstructed with detectors downstream of it, and it reconstructs tracks of particles that have a long lifetime and are more likely to decay downstream of the VELO, without giving any hit on it, as K^0_S or Λ. It covers the full detector acceptance with a sensitive area 150 cm wide and 130 cm high.
It is composed by four different layers, matched in pairs, positioned at a distance of 30 cm along the beam axis. The four layers are arranged in a configuration defined as x-u-v-x. The first and the last layer, the x ones, have vertical strips, while the u and the v are slightly rotated, by $\pm 5°$, respectively. This layers structure is shown in Figure 2.7. This arrangement allows to avoid the insurgence of fake hits in the detector, present in case of a 90° rotation between layers. This can be better understood looking at Figure 2.8. The TT provides a single-hit resolution that is $\simeq 50\,\mu$m.

T-stations

The T-stations are three tracking detectors (T1-T3), located immediately downstream the magnet to reveal tracks of charged particles and determine their momentum through the bending provided by the magnet. Each station is composed by four detection planes, approximately 6 m wide and 4.5 m high. The plans consist of two different sub-detectors, with different technology: the Inner Tracker (IT) and the Outer Tracker (OT). The first covers the region near the beam pipe and shares the same silicon-strip technology of the TT. The second one covers the external region of the plan and is a straw-tube detector.

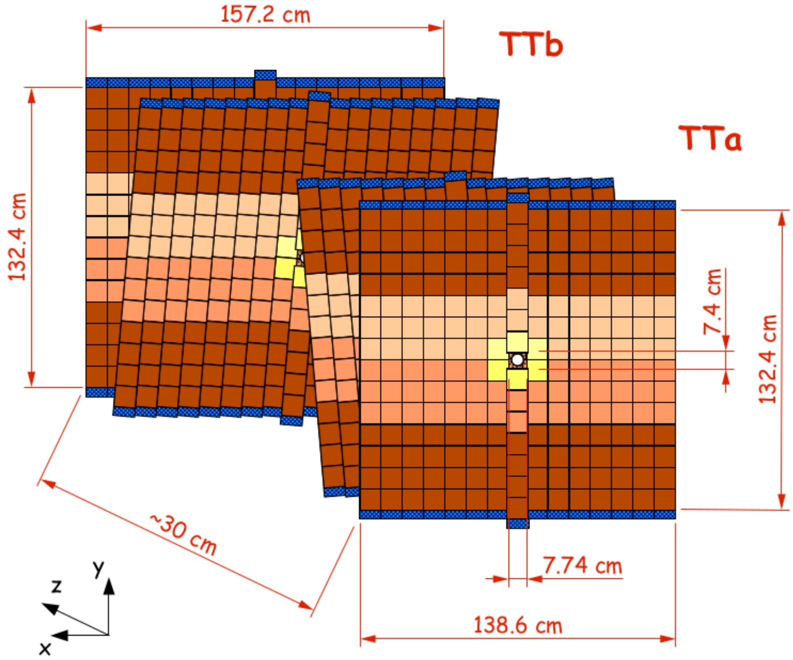

Figure 2.7: Schematic representation of the TT detector

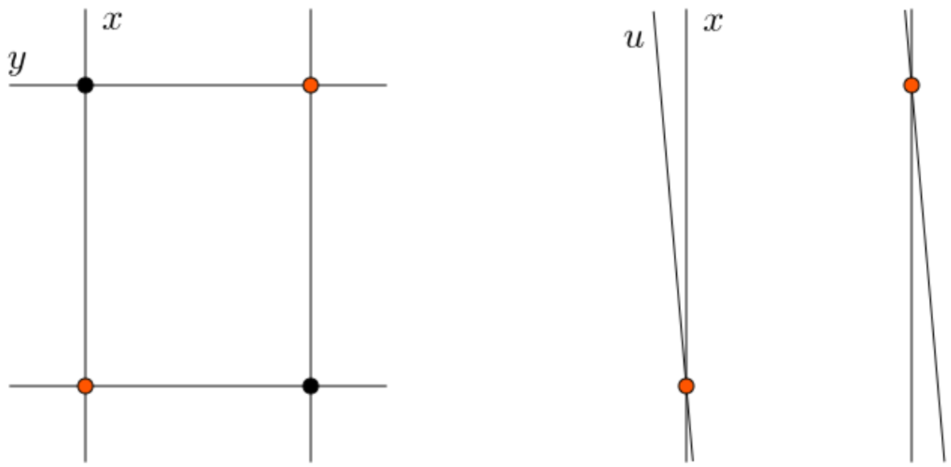

Figure 2.8: TT hits determination in case of a 90° rotation between layers (left) and 5° rotation (right). The same hits in x-layers in the two different configurations creates, in case of an orthogonal arrangement, the appearance of two additional fake hits, represented in black; this, on the contrary, does not happen in the adopted configuration.

This choice allows to keep the cost of the system low and at the same time have a good track resolution in the region near the pipe, where most of the particles flow. The four plans constituting a station have the same x-u-v-x arrangement as the TT one, for both IT and OT and for the same reason. The stations structure can be seen in Figure 2.9.

Inner Tracker

The Inner Tracker is the detector composing the T-stations located in the region around the beam pipe. It has a cross-structure, approximately 125 cm wide and 40 cm high,

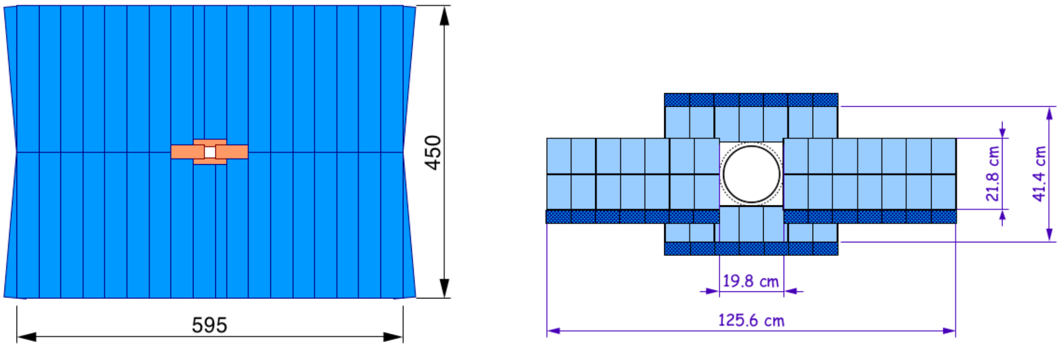

Figure 2.9: Schematic representation of the frontal view of a T-station (lengths in cm), on the left. The Inner Tracker is drawn orange, the Outer Tracker is in blue. On the right it is represented the magnified view of Inner Tracker only, in case of an x plane.

covering an acceptance of $\simeq 150 - 200\,\text{mrad}$ in the x-z plane and $\simeq 40 - 60\,\text{mrad}$ in the y-z plane. It is a micro-strip silicon [16] detector as the TT, as already said, and it provides the same single-hit resolution of $\simeq 50\,\mu\text{m}$.

Outer Tracker

The Outer Tracker (OT) [3] composes the external part of the T-stations. It is a gaseous ionization detector consisting of straw-tubes operating as proportional counters. Each plan is composed of two staggered straw rows, as shown in Figure 2.10. This configuration

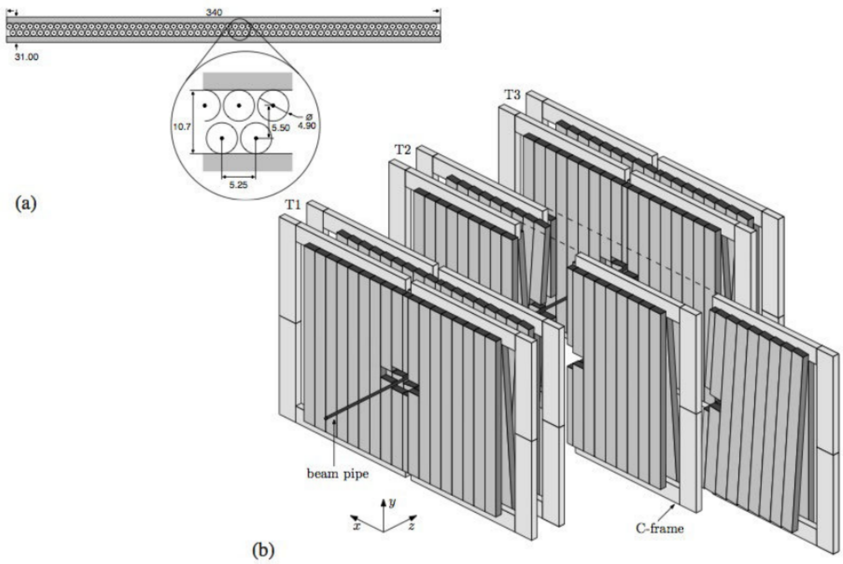

Figure 2.10: Structure of straw tubes composing a plan in a T-station in (a). Schematic representation of the Outer Tracker in (b). Figure taken from [14].

excludes the presence of a non-sensitive zone between two straws. The drift tubes are 2.4 m long and made of Kapton-XC coated with aluminum. They have an inner diameter of 4.9 mm and are filled with a gas mixture of $Ar/CO_2\,/O_2$ (70%/28.5%/1.5%), which guarantees a drift time below 50 ns. The anode is a golden plated tungsten wire and has a diameter of 25 μm. In working condition the wire is put at a voltage of 1550 V with respect to the tube. In the OT the drift time measurement provides a single-hit spatial resolution of $\simeq 200$ μm in each detection plane.

2.2.2 Track reconstruction

Particle trajectories are identified in LHCb through a pattern recognition algorithm that matches the hits in the detectors composing the tracking system already explained to form a single track. Depending on the decay topology and the particles involved in it, the reconstruction can be performed with different detectors. This can significantly affect the resolution on the position that can be achieved, since there are large differences between detectors performances.
Different track types are defined, depending on the detectors crossed:

- as **Long tracks** are detected particles that crossed the entire tracking system; these are reconstructed exploiting the VELO and T-stations, adding information provided by TT when available;
- as **Downstream tracks** are reconstructed particles that produced hits only in the TT and T-stations; long-living particles as K^0_S or Λ can be reconstructed in this way, when they decay after the VELO acceptance;
- **VELO tracks** are reconstructed exploiting VELO hits only; these are exploited in the PV reconstruction and as seeds for Long and Upstream tracks;
- as **Upstream tracks** are detected particles that produces hits in the VELO and the TT only, since are deflected from the detector acceptance by the magnetic field;
- as **T tracks** are reconstructed particles that produced hits only in the T-stations.

In this analysis both Long and Downstream tracks are exploited; a scheme for the track reconstruction is shown in Figure 2.11.

2.2.3 Particle identification system

As mentioned before this system is composed by five different detectors: two RICH detectors, two calorimeters and the muon system. Its purpose is to provide the identification of every particle that flows in the detector. This is possible through the analysis of the signal pattern that the particle created in the detectors with its passage. Each RICH allows the separation mostly between pions and kaons, calorimeters determine the presence of hadrons, electrons and photons and muons presence is revealed through the muon chambers.

Ring Imaging Čerenkov

The two Ring Imaging Čerenkov detectors present in the experiment (RICH 1 and RICH 2) allow the separation between pions, kaons and protons. RICH1 is located upstream the magnet, covering the full detector acceptance, the RICH2 is downstream the last tracking station and has an an angular acceptance going from 15 to 120 (100) mrad in the bending

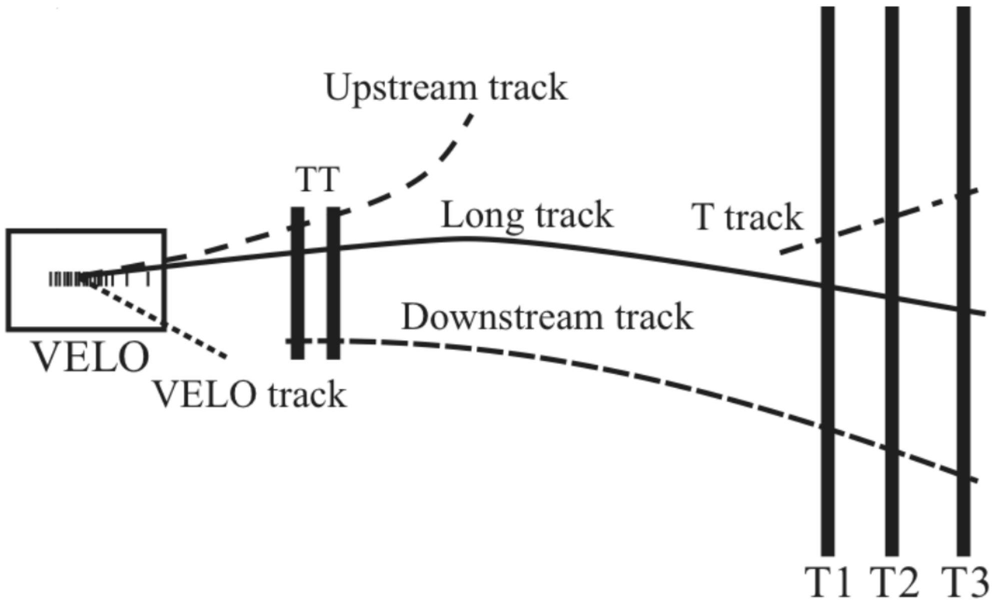

Figure 2.11: Scheme of the tracks definition in LHCb, depending on the detectors exploited.

(non-bending) plane. The separation is based on the measurement of the angle emission of Čerenkov radiation. It is emitted by charged particles passing through a medium with a refraction index $n \neq 1$ and with a velocity that makes $\beta > 1/n$. When this happens the particle emits photons with a fixed angle (θ_c) with respect to the flight direction, given by:

$$\cos\theta_c = \frac{1}{\beta n} = \frac{1}{n}\sqrt{1 + \left(\frac{mc}{p}\right)^2} \tag{2.2}$$

From this relation the particle mass can be determined, allowing its identification as can be seen in Figure 2.12.

In both RICHs two kinds of mirrors are present, to allow θ_c measurement: spherical and flat mirrors. The first ones allows ring-imaging, while the second ones direct radiation to the Hybrid Photon Detectors (HPD) aimed to detect light. The HPD can detect emitted Čerenkov light with a wavelength λ between 200 and 600 nm. These are located out of the detector acceptance and encased in a magnetic shield that allows their correct activity. The two RICHs are filled with two different substances, that allows Čerenkov light emission. In RICH1 both aerogel ($n = 1.03$) and C_4F_{10} ($n = 1.0014$) are present, while RICH2 is filled with CF_4 ($n = 1.0005$). The adoption of different radiators tunes each RICH on a different particle momentum range. RICH1 is designed to identify particles with low momentum, in the $1 - 60\,\mathrm{GeV}/c$ range, while RICH 2 is optimized for particles with an higher momentum, hence in the $15 - 100\,\mathrm{GeV}/c$ range. The two RICHs, working simultaneously, allow the identification of charged particles with a momentum in the $1 - 100\,\mathrm{GeV}$ range. For pion-kaon with momenta up to 30 GeV/c the separation is 90% efficient.

Calorimeters system

The LHCb calorimetric system [13] allows the identification of hadron, electrons and photons and provides a raw measurement of their energy and position. These informations

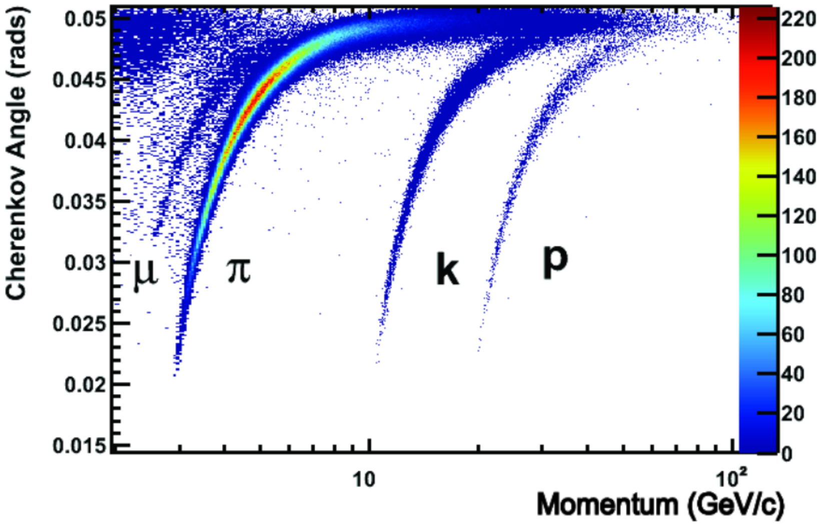

Figure 2.12: Relation between θ_c and the particle momentum for RICH1. Figure taken from [10].

are essential in the LHCb trigger, where they are exploited in the lowest level (L0, as will be explained later). This because, even if raw, they can be rapidly accessed, giving early information about the event. All calorimeter detectors share the same readout technology: wavelength-shifting fibers carry the light produced in the scintillator layer to photomultipliers.
The calorimeter system is composed by four different sub-detectors. The first two elements are the Scintillator Pad Detector (SPD) and the PreShower detector (PS). These are two scintillating planes, both with a width equal to 2 radiation length (X_0) and 0.1 nuclear interaction lengths (λ_{int}), separated by a 15 mm thick lead converter. The SPD allows the distinction between neutral and charged particles, while the PS separates between electromagnetic showers from hadron. The other two sub-detectors are the electromagnetic calorimeter (ECAL) and the hadron calorimeter (HCAL), both placed between the first and the second muon station, covering an angular acceptance of 25-300 (25-250) mrad in the bending (non-bending) plane. The ECAL is composed by alternate scintillator (4 mm) and lead (2 mm) layers, for an overall thickness of 25 X_0, allowing a complete electromagnetic shower containment and a good energy resolution, equal to $\sigma_E/E(\text{GeV}) = 10\%/\sqrt{E(\text{GeV})}$. It is divided in three regions, with different cell sizes depending on the distance from the beam axis, as can be seen in Figure 2.13. The HCAL is made of alternate scintillator (4 mm) and iron (16 mm) layers, for an overall thickness of 5.6 λ_{int}. It provides an energy resolution equal to $\sigma_E/E(\text{GeV}) = 70\%/\sqrt{E(\text{GeV})}$. This value is due to the poor thickness, that does not allow the complete shower containment and hence energy measurement. For this reason the HCAL is exploited only for trigger purposes and not for off-line analysis.

Muon system

The muon system [11] purposes are to reveal the presence of muons in the event and to measure their transverse momentum. These informations are exploited both in the trigger

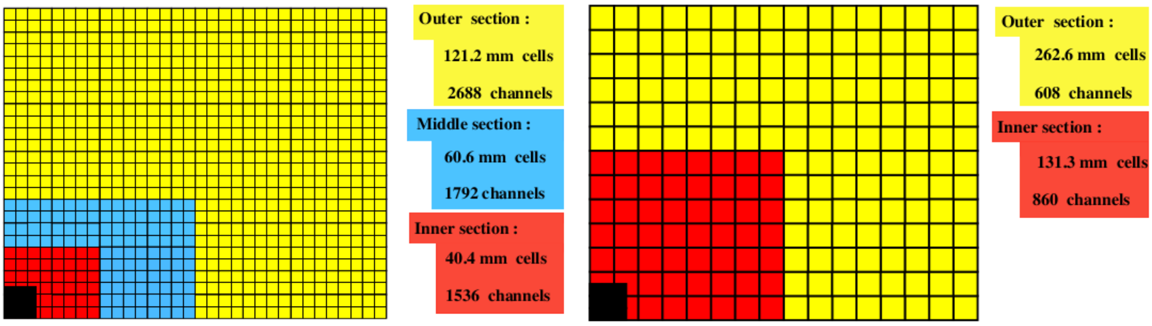

Figure 2.13: Schematic representation of ECAL (left) and HCAL (right) cell segmentation. Figure taken from [12].

and in the off-line analysis.
The system is based on five different detectors, labeled as (M1-M5), covering an angular acceptance from 20 (16) mrad to 306 (258) mrad in the bending (non-bending) plane. The structure is shown in Figure 2.14. Each station is divided in four different quadrants,

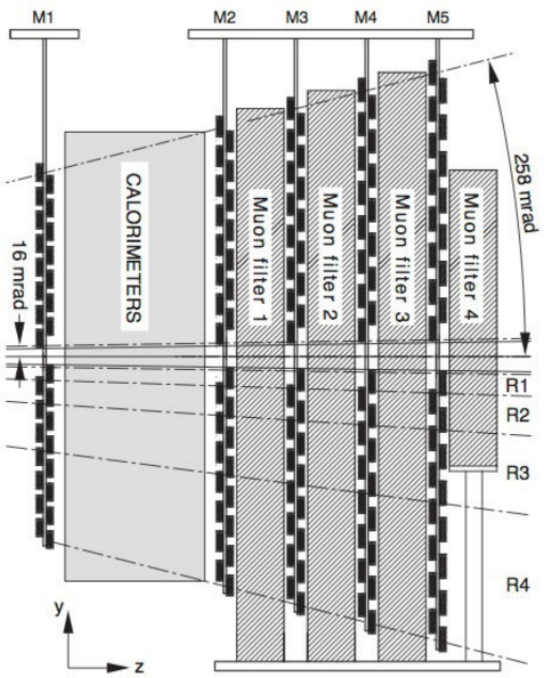

Figure 2.14: Schematic representation of muon system. Figure taken from [12].

each divided again in four concentric regions (R1-R4), where R1 is the one closer to the beam pipe and R4 is the farthest. The M2-M5 stations are located downstream of the calorimeters, alternated with 80 cm thick iron absorber planes, resulting in an overall thickness of about 20 X_0. The iron aims to select muons with high momentum; to cross the entire detector for a muon is required a minimum momentum of about 6 GeV/c. The first station, M1, is located between the RICH2 and the calorimeters, where the multiple-scattering effects are less significant. In this configuration M1 improves the transverse momentum measurement of downstream stations. Two different technologies are adopted in the muon system: triple gas electron multiplier and multi-wire proportional chamber detectors, both based on Ar, CO_2 and CF_4 mixture, with different proportions. The former is adopted in the R1 region of the M1 station only, since it ensures the radiation tolerance necessary for the present high particle density. In all other detectors the latter is adopted. This system provides a transverse momentum resolution of about 20% for stand-alone muon reconstruction.

2.3 LHCb trigger

A trigger consists in an algorithm aimed to select events, interesting for the analysis that has to be performed, between background events, anyway produced in the collisions. The presence of a trigger algorithm is necessary when it is impossible to save information about all produced events, because of limited data-flow and storage dimension. In the case of LHCb these limitations are both present, since the high number of produced events makes impossible the record of all of them and the detector has a limited readout rate, as previously mentioned.
The LHCb trigger [29] is designed to distinguish and select events containing b- and c-hadrons, experiment analyzes target, from the huge number of background processes, containing mostly light quarks. The selection is based principally on the larger flight distance of heavy-flavor hadrons and on the relatively high transverse momentum of interesting events. To set an order-of-magnitude scale it can be said that light-quark processes are produced in LHC with a rate similar to the one of the collisions, hence 40 MHz. On the other hand, the production rate of events containing any b-hadron decay corresponds to ~ 15 kHz and circa 20 times larger for c-hadron decay. In addition only a small fraction of the considered heavy-flavor decay are useful, reducing the rate of these events to few Hz. Consequently the trigger represents one of the essential components necessary to perform a successful analysis for the LHCb experiment.
The trigger processes events in two sequential steps. The first one is an hardware-based low level trigger, defined Level-0 trigger (L0), the second one is a software-based system, called High-Level Trigger (HLT). The overall trigger performance allows to reduce the events rate from 40 MHz of the bunch crossing to 12.5 kHz; the data-flow in the trigger is reported in Figure 2.15.

2.3.1 Level-0 trigger

L0 is a completely-custom hardware system, based on FPGA technology. This choice was driven by the necessity for a fast system, able to work at the LHC bunch-crossing rate. In fact, L0 purpose is to reduce the events rate from the initial 40 MHz, to a value smaller than 1.1 MHz, that is the maximum rate at which the detector can be read out.
The event selection is based on three different trigger decisions, corresponding to different requirements: L0 pileup, L0 calorimeter and L0 muon. The logic *or* between these conditions defines the L0 global decision. When at least one of the mentioned conditions is satisfied, and hence the L0 global is positive, the event is selected and the entire detector information is read out and transferred to the subsequent trigger step. Because of the bunch-crossing rate, the L0 decision has to be taken in a really short time, corresponding to the buffer fixed latency time in which the detector information is temporarily stored, that is equal to 4 μs. Because of this, the L0 trigger decision is based on simple

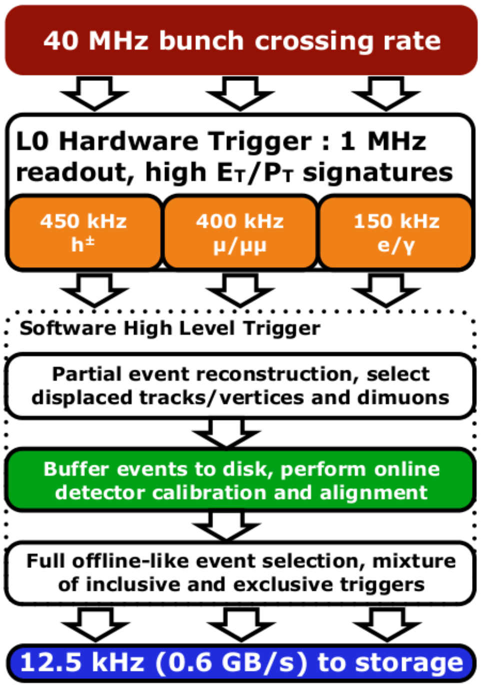

Figure 2.15: Data-flow structure in the LHCb trigger. The reported values represent the accepted rates for each stage.

information, that can be rapidly accessed through the read out of fast sub-detectors, as calorimeters and muon stations.

L0 pileup

The first trigger condition exploits VELO information to estimate the number of primary vertices present in each bunch crossing and the backward charged particle multiplicity. The events selected by this L0 line are not interesting for off-line analysis (events with too high track multiplicity are usually vetoed using the SPD signal, for example) but are exploited in the luminosity measurement.

L0 muon

The L0 muon decision exploits information furnished from muon stations to determine whether the event is interesting or not. Firstly the five muon stations determine the presence of at least one muon in the event, and the first two (M1 and M2) provide the measurement of the muon transverse momentum, too. After this, the most energetic muons are identified in each quadrant and, depending on their transverse momentum, the event can be accepted or rejected, if it satisfies at least one of two different requirements:

- in L0 muon a threshold is set on the highest transverse momentum of muon in the event;
- in L0 dimuon a threshold is set on $\sqrt{p_{\mathrm{T}}(\mu_1) \cdot p_{\mathrm{T}}(\mu_2)}$, where μ_1 and μ_2 are the two muons with highest transverse momentum in the event.

L0 calorimeter

This trigger decision is based on a first transverse momentum estimate of electrons, photons and hadrons, provided by the calorimeter system detectors. The transverse momentum estimate is done through the energy deposited by a particle in the calorimeter and through the deposit position. Every calorimeter layer is divided into clusters of 2×2 cells. This clusters dimension is chosen to completely include a single particle energy deposit and avoiding at the same time the overlap of different deposits. For each cluster a transverse energy is identified, defined as:

$$E_{\mathrm{T}} = \sum_{i=1}^{4} E_i \sin \theta_i \tag{2.3}$$

where i runs over the four cells that define a cluster, E_i is the energy deposit in each cell and θ_i is the angle between the beam axis and the direction identified by the cell center and the nominal interaction point. The E_{T} values extracted from each calorimeter are then summed up, to give the overall E_{T} estimate for the particle.
The event is accepted whether it has an E_{T} greater than a certain threshold value, different for hadrons (L0 hadron), electrons (L0 electron) and photons (L0 photon). The particle is identified through the pattern of the released energy in each layer, as explained before. The requirement for a minimum value for hadron transverse energy selects more likely particles (typically pions) coming from the decay of b- and c-hadrons, since these have, on average, higher transverse momentum than particles coming from decay of particles composed only by light quarks.

2.3.2 High Level Trigger

For events that pass at least one of the L0 trigger requirements, HLT receives the full detector information. HLT is a software-based system, consisting on a C++ executable, that runs on each processor of the Event Filter Farm (EFF) computer array. HLT performs an analysis similar to the off-line one, based on a partial event reconstruction. The complete off-line analysis can not be run on each event by HLT, because of the needed computing time: for off-line analysis, which consists of complete event reconstruction, a processing time of at least 2 s is necessary, while for on-line processing the available time is considerably shorter, worthing at maximum 50 ms.
To increase the event selection efficiency in this condition the HLT is divided in two sequential stages, defined as HLT1 and HLT2.

HLT1

HLT1 purpose is to reduce the event rate to a value of about 30 kHz. Events selection is based on the event tracks reconstruction performed in the VELO. It is exploited to identify in the analyzed events the present primary vertexes and also to measure their position. Relying on these information it is possible to search for tracks that have large Impact Parameter (IP)[4], that is typically the sign of the presence, in the decay, of an heavy-flavor hadron. These tracks are processed by several different algorithms, defined

[4]Distance of closest approach between the PV and the direction identified by the momentum of the particle, as will be defined later.

as *trigger lines*, that apply each one a different set of cuts, based on the tracks quality reconstruction, IP and p_{T}.

HLT2

In HLT2 a more similar analysis to the off-line one is performed, based on a complete event reconstruction, possible thanks to the significant event rate reduction performed by HLT1. At this trigger stage all the detector information is exploited (track reconstruction and particle identification) and consequently it is possible to identify different event types, through the kind of decay topology and particle involved in the process. Relying on this capability, also HLT2 is divided in several and different trigger lines. Each one is aimed to the selection of a certain kind of decay events as, for example, different decay D^0 channels. The overall output rate after this final step is about 12.5 kHz.

The reported value for the final output rate of is limited by the disk storage space available. For certain trigger lines, aimed to the collection of specific decay events, this imposes the application of a pre-scaling procedure, hence the random selection of a fraction of the triggered events. This allows the collection of events that have, for example, smaller *BR*, but it significantly limits the overall number of collected events on disk. This reflects, on the application of a limit on the statistical significance that can be achieved.
Charm physics is affected by the output rate constrain, since it has, as explained before, a larger event rate with respect to other event types, as beauty physics. It is an important target in LHCb to overcome these computing constrain, since it allows to achieve better results, with the same experimental facility. A strategy implemented to solve this problem is the *turbo stream* approach. It is based on performing an on-line analysis similar to the off-line one, as done in HLT2. Having access to good-quality data already at trigger step has big benefit. There is the possibility to record only processed data, discarding raw information, as the tracks not involved in the interesting process, and used only to determine the PV position. This decreases the event size, from 70 kB to 5 kB, allowing the record of a larger number of events per second, with the same overall data flow. The $D^0 \to K^0_S K^0_S$ events, analyzed in this work, are collected using the *turbo stream* strategy.

Chapter 3

Measuring the $D^0 \to K^0_S K^0_S$ asymmetry

In this chapter I will describe on the experimental approach to the time-integrated CP asymmetry in $D^0 \to K^0_S K^0_S$ decays measurement. Even if this discussion shares some points with the one presented in Chapter 1, I decided, for clarity, to explain the analysis approach I adopted without reference to the previous one.

3.1 $\mathcal{A}^{CP}$ $(K^0_S K^0_S)$ measurement in LHCb

The aim of the analysis is to measure the asymmetry between the probability for D^0 and $\overline{D}^0$ to decay into the same $K^0_S K^0_S$ final state, given by *CPV* in the decay. It is defined for this final state as:

$$\mathcal{A}^{CP}(K^0_S K^0_S) = \frac{\Gamma(D^0 \to K^0_S K^0_S) - \Gamma(\overline{D}^0 \to K^0_S K^0_S)}{\Gamma(D^0 \to K^0_S K^0_S) + \Gamma(\overline{D}^0 \to K^0_S K^0_S)} \tag{3.1}$$

Experimentally this quantity can be accessed by measuring the asymmetry between the number of D^0 and $\overline{D}^0$ decaying into $K^0_S K^0_S$, defined as $\mathcal{A}^{raw}$:

$$\mathcal{A}^{raw} = \frac{N(D^0 \to K^0_S K^0_S) - N(\overline{D}^0 \to K^0_S K^0_S)}{N(D^0 \to K^0_S K^0_S) + N(\overline{D}^0 \to K^0_S K^0_S)} \tag{3.2}$$

that can be extracted revealing and counting these events.

3.1.1 D^0 tagging

In measuring the quantity expressed in 3.2, it emerges clearly that an essential requirement is the identification of the presence of a D^0 or an $\overline{D}^0$ in the event, through which $N(D^0 \to K^0_S K^0_S)$ and $N(\overline{D}^0 \to K^0_S K^0_S)$ can be extracted. For charged particles the distinction between matter and anti-matter can be made by observing the net charge of the final state, of opposite sign for the two cases. This strategy can not be adopted here, since the D^0 is neutral and it decays into a final state that is a *CP* eigenstate. It is possible to overcome this obstacle, and hence tag the presence of D^0 or $\overline{D}^0$ in the $D^0 \to K^0_S K^0_S$ decay, by reconstructing the complete D^0 decay chain. We exploit the process where a D^0 comes from the decay of a D^*, in which a π is produced:

$$D^{*\pm} \to D^0(\overline{D}^0)\pi^{\pm} \tag{3.3}$$

where D^0 or $\overline{D}^0$ are alternatively present. In this process, the sign of the pion - coming from the same D^* decay that generated the D^0- can be used to tag the D^0 flavor. For this reason I will refer to it as π_{tag} from this point. In particular the presence of a π^+ and π^- indicates the presence of a D^0 and $\overline{D}^0$, respectively. This is because the considered decay proceeds *via* strong interaction, that conserves CP. With this strategy the sample can be split into two sub-samples, depending on the sign of the pion, where the yields can be separately extracted, allowing the determination of the CP asymmetry.

3.1.2 Event detection

With the adoption of this tagging strategy, the events to be analyzed include the complete decay chain:

$$D^{*\pm} \to D^0(\overline{D}^0)\pi^\pm_{tag} \to (K^0_\mathrm{S}K^0_\mathrm{S})\pi^\pm_{tag} \to (\pi^+\pi^-)(\pi^+\pi^-)\pi^\pm_{tag} \tag{3.4}$$

Its schematic representation is shown in Figure 3.1 (from here on I will omit for brevity the D^*, π sign and the D^0 flavor).

This kind of events are detected and then reconstructed through the five pions present

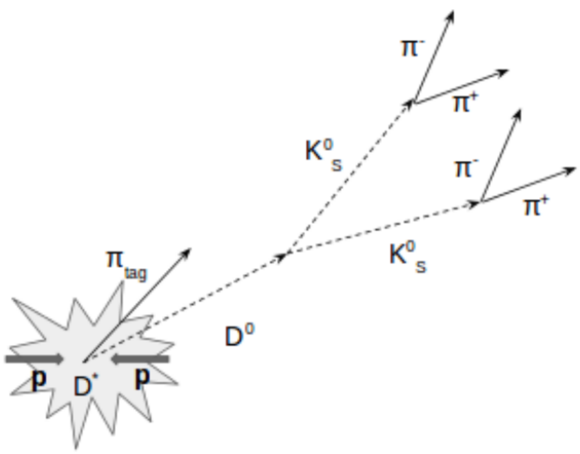

Figure 3.1: Schematic representation of the analyzed decay chain, distances are not to scale.

in the final state. The detection can happen in LHCb in three different configurations, depending on the detectors adopted to reconstruct each pion pair from the K^0_S decays. While the π_{tag} is always reconstructed as a Long track, since it always causes some VELO hits, pion pairs coming from K^0_S can be revealed both with Long or Downstream tracks. This is due to the K^0_S relatively long lifetime and boost at which are subjected, that is significantly different from zero. In these events K^0_Ss have a $\langle\beta\gamma\rangle \sim 70$, determined from the K^0_S momentum mean value, that can be estimated from the distributions present in 4.3. In this kinematic condition K^0_Ss can travel several cm and decay after the VELO acceptance. In this configuration they are reconstructed as Downstream tracks, since they produce hits only in the TT and T-stations.

The sample is then divided into three separate sub-samples (*channels*), depending on the K^0_Ss detection configuration:

- **LL channel** when both K^0_S are reconstructed with Long tracks;

- **LD channel** when one K^0_S is reconstructed with Long and the other with Downstream tracks;

- **DD channel** when both K^0_S are reconstructed with Downstream tracks.

The three channels have different resolutions (for example in vertex position and momentum), because of the different hits position resolution provided by the involved detectors and the larger distance between the detector and the interaction point for the VELO, TT and T-stations. To better handle these differences and obtain a better sensitivity on $\mathcal{A}^{CP}$ the three channels will be separately analyzed, three different $\mathcal{A}^{CP}$ values will be extracted and then recombined to find the definitive result.

3.1.3 Decay chain fit

To extract information describing the detected process it is necessary to perform a fit. A peculiarity of this decay chain is that it includes several neutral particles. These can not be directly revealed, since they do not interact with the detectors material and can not produce any hit and the situation requires a specific approach when is present the decay of a neutral particle into two others, as happens in this case with $D^0 \to K^0_S K^0_S$.
In high energy physics experiments it is often necessary to reconstruct unstable particles, that can be detected only through their decay products. The usual method adopted to determine the observables related to the particles present in the decay chain is the "leaf-by-leaf" method. This is adopted by LHCb too, with the decay chain fitter named LoKi Fitter. Here quantities related to the mother particle are extracted through a vertex fit, that takes as input information given by its decay products. This is done starting from the end of the chain, with a "bottom-up" approach, separately for each present particle. Given that in the leaf-by-leaf method each decay vertex is separately fit, one located at the end of the decay chain does not influence the reconstruction of particles located upstream. This does not properly work in case of a decay process that involves neutral particles only, as the one considered here, since there are not tracks that can be used to reconstruct the decayed particle.
This issue has been encountered previously in the BaBar experiment, in case of the reconstruction of the $K^0_S \to \pi^0\pi^0$ decay, where no tracks can be exploited to reconstruct the K^0_S. To solve this problem they set up a different method to fit the decay chain, named Decay Tree Fitter (DTF) [30]. The main difference with the leaf-by-leaf method is that here the whole decay chain is fitted in a single step and the parameters about each particle are simultaneously extracted, allowing optimized reconstruction of decays as the $K^0_S \to \pi^0\pi^0$ or $D^0 \to K^0_S K^0_S$. This is done through the parametrization of the decay chain in terms of vertex positions, momenta and decay times, with the extraction of these parameters in an single fit. In this procedure two *internal* constrains are applied: the decay vertex of a particle and the production vertex of its daughters have to coincide (vertex constrain) and it is required the momentum conservation, ensuring the four-momentum conservation, too. More *external* constrains can be introduced, additionally to the internal ones. In this analysis two different ones will be used: the mass of each K^0_S candidate is fixed to the known value (K^0_S mass constrain) and the D^* (and hence the D^0) is forced to come from the PV (PV constrain).
These constrains can be extremely powerful, since they improve the mass resolution and may allow a better signal to background ratio, but can not be used in the first part of the

analysis. This is because, even if they give a tighter signal peak, they significantly distort the background shape. Therefore until the background contribution is not significantly reduced it is not useful to use the variables obtained through DTF, since the extraction of signal yields can be difficult.
For these reasons in the analysis we will exploit both the Loki Fitter and DTF variables. The former when the background contribution has not been reduced yet, while the latter are adopted in the last part of the analysis, where a selection aimed to reject background has been already applied.

3.1.4 Asymmetry extraction

The variables extracted by the fits are then used to extract $N(D^0 \to K^0_S K^0_S)$ and $N(\overline{D}^0 \to K^0_S K^0_S)$, and hence the $\mathcal{A}^{CP}$. To count the events we exploit the Δm variable, where $\Delta m = m$ $(D^0$ $\pi_{tag})$ - m $(K^0_S K^0_S)$ is the difference between the mass of the D^* and the D^0 candidate, respectively. This is crucial in this analysis, because in Δm distribution the presence of the signal is a sharp peak and the signal yield can be directly extracted fitting its shape.
Before the asymmetry extraction it is important in this analysis to apply a selection, aimed to the rejection of a significant fraction of the various background sources. This is not ordinary for an LHCb analysis on charm hadrons decay, because here the main issue is usually due to the large amount of data that has to be managed. The $D^0 \to K^0_S K^0_S$ LHCb sample, on the contrary, is typically made of few hundreds of events ([5, 40]) and the greatest part of the effort is the research for a cuts configuration that allows the achievement of the best $\mathcal{A}^{CP}$ resolution, improving the signal to background ratio. The sample smallness, with respect to other charm decays, is due to the difficulty in detection and triggering of neutral and long-lived particles, as K^0_Ss, in the LHCb detector. It, in fact, was tuned to detection of particles with smaller flight distance, typically b- and c-hadrons, that cross the VELO detector. On the contrary, large fraction of produced K^0_Ss decays downstream of the VELO and can be reconstructed only with lower quality information. This makes the collection and the analysis of the $D^0 \to K^0_S K^0_S$ sample particularly challenging and requires specific efforts.

After the selection identification, fits to the Δm distributions are performed, obtaining the signal yields for the samples tagged with opposite π_{tag} sign. From these, through (3.2), it is possible to extract the $\mathcal{A}^{raw}$ value. It is important to remember that $\mathcal{A}^{raw}$ does not directly corresponds to $\mathcal{A}^{CP}$. In fact, in an experimental environment like LHCb, the considered asymmetry receives other contributions and it can be expressed as:

$$\mathcal{A}^{raw} \approx \mathcal{A}^{CP} + \mathcal{A}^{prod} + \mathcal{A}^{det} \tag{3.5}$$

where the approximation is valid at first order. $\mathcal{A}^{prod}$ is the asymmetry between the probability to produce a D^{*+} or a D^{*-} and $\mathcal{A}^{det}$ is the asymmetry between the π^+_{tag} and π^-_{tag} detection efficiency. The detection efficiency of the two K^0_S is irrelevant, since these are a CP-symmetric state.

3.1.5 $\mathcal{A}^{prod}$

LHC collisions are a not-CP symmetric initial state, composed by two protons. In this configuration there is a non-zero $\mathcal{A}^{prod}$ term, given by the different values assumed by the

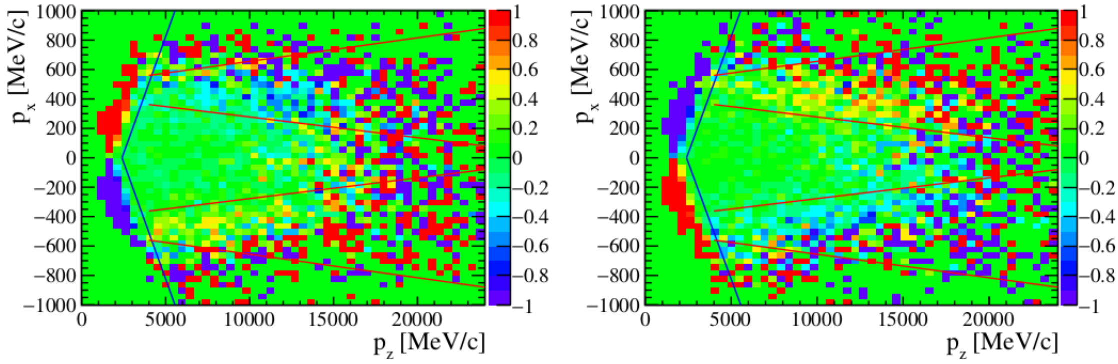

Figure 3.2: π_{tag} charge asymmetry for LL channel collected during 2015 for *MagUp* (left) and *MagDown* (right). Figure taken from [39].

D^{*+} and D^{*-} cross sections [32]:

$$\mathcal{A}^{prod} = \frac{\sigma(D^{*+}) - \sigma(D^{*-})}{\sigma(D^{*+}) + \sigma(D^{*-})} \tag{3.6}$$

3.1.6 $\mathcal{A}^{det}$

The $\mathcal{A}^{det}$ arises as a consequence of a different detection efficiency for π^+_{tag} and π^-_{tag}. This is partially due to an intrinsic difference in probability of interaction with the detector for opposite-sign particles, but the most significant contribution to $\mathcal{A}^{det}$ is given by the not-symmetric magnetic field present in the detector. It, in fact, bends particles of different sign in opposite directions and this leads to a different acceptance in the T-stations and a different probability to cross the beam pipe for the two cases. These asymmetric effects are significantly reduced thanks to periodic inversion of the magnetic field during data taking, that averages the asymmetries to a smaller value, but even with this procedure some detection asymmetries remains. It is important to pay attention to regions where these assume large values. In this case the approximation adopted in (3.5) could not stand, and for this reason, these regions are usually excluded with fiducial cuts. These are cuts that exclude the regions where the asymmetry, for events collected with a single magnet polarity, assumes a large value (near 100%). These regions, and the cuts applied to remove them are shown in Figure 3.2. Fiducial cuts are identified by:

$$|p_x| \leq \alpha(p_z - p_0) \tag{3.7}$$

$$\text{if } |p_y/p_z| < 0.02: \quad |p_x| < p_1 - \beta_1 p_z \vee |p_x| > p_2 + \beta_2 p_z \tag{3.8}$$

where p_x, p_y and p_z are the π_{tag} momentum components, $\alpha = 0.317$, $\beta_1 = 0.01397$, $\beta_2 = 0.01605$, $p_0 = 2400\,\text{MeV}/c$, $p_1 = 418\,\text{MeV}/c$ and $p_2 = 497\,\text{MeV}/c$. The first remove regions where pions are bent inside the T station acceptance depending on their charge (100% asymmetric regions for each magnet polarity) and the second one removes pions flying near the beam pipe.

3.1.7 $\mathcal{A}^{prod}$ and $\mathcal{A}^{det}$ subtraction

To obtain $\mathcal{A}^{CP}$ from the measured $\mathcal{A}^{raw}$, $\mathcal{A}^{prod}$ and $\mathcal{A}^{det}$ have to be subtracted. It is not helpful to use the measured values for these two asymmetries, since the resulting uncertainty on the $\mathcal{A}^{CP}$ value would be significantly worsened by the $\mathcal{A}^{prod}$ and $\mathcal{A}^{det}$ value. Therefore, in LHCb analyses of this type, $\mathcal{A}^{prod}$ and $\mathcal{A}^{det}$ are typically subtracted by exploiting a control channel.
For this purpose, it is necessary to identify another decay process, affected by the same $\mathcal{A}^{prod}$ and $\mathcal{A}^{det}$ of the signal sample, available with high statistics and with a $\mathcal{A}^{CP}$ value known with a precision better than the expected sensitivity of the analysis. If these conditions apply, it is possible to extract the difference between the two $\mathcal{A}^{CP}$ values (defined as $\Delta\mathcal{A}^{CP}$) from the difference between the signal and control channel $\mathcal{A}^{raw}$:

$$\mathcal{A}^{raw}(K^0_S K^0_S) - \mathcal{A}^{raw}(c.c.) = \mathcal{A}^{CP}(K^0_S K^0_S) - \mathcal{A}^{CP}(c.c.) \equiv \Delta\mathcal{A}^{CP} \tag{3.9}$$

since $\mathcal{A}^{prod}$ and $\mathcal{A}^{det}$ cancel each other in the $\mathcal{A}^{raw}$ difference. From $\Delta\mathcal{A}^{CP}$ it is possible to extract $\mathcal{A}^{CP}$ $(K^0_S K^0_S)$ simply adding the $\mathcal{A}^{CP}$ $(c.c.)$ term:

$$\mathcal{A}^{CP}(K^0_S K^0_S) = \Delta\mathcal{A}^{CP} + \mathcal{A}^{CP}(c.c.) \tag{3.10}$$

This procedure does not worsen the sensitivity on $\mathcal{A}^{CP}$ $(K^0_S K^0_S)$ measurement, thanks to the control channel high statistics and the precision on the $\mathcal{A}^{CP}$ $(c.c.)$ measurement. In most recent LHCb analysis, the $D^0 \to K^+K^-$ sample has been adopted as control channel for the $D^0 \to K^0_S K^0_S$ analysis, since the two samples contain events with the same event topology, except for the D^0 decay mode and $\mathcal{A}^{CP}$ (K^+K^-) has already been measured with a precision that is one order of magnitude smaller than the expected resolution of our analysis [7]. In older analyses of the same channel, the $D^0 \to K^-\pi^+$ was used as control channel [5].

3.2 Experimental status

The measurement of $\mathcal{A}^{CP}$ in $D^0 \to K^0_S K^0_S$ decays has been already performed, by several experiments. LHCb provided the most recent measurement of this quantity, exploiting data collected during first two years of Run-2, achieving a statistical sensitivity of 3.4%. Extrapolating this resolution naively to the Run-2 data yields expectations for $\mathcal{A}^{CP}$ resolution around 2%. This is still insufficient for a useful exploration of this channel. The future Run-3 will bring more data, but it is not yet clear what the efficiency for this difficult channel will be in the upgraded experiment, that will have much tighter precessing time requirements. As a consequence, it is very important to perform now a study of possible ways to enhance the LHCb sensitivity to this "golden" channel - both with the already available data, and with the samples that will come. This will be the central subject of the rest of this document.

Chapter 4

$D^0 \rightarrow K^0_S K^0_S$ in LHCb new data

In this chapter I explain the first part of the analysis I performed, based on the estimate of the sample signal yields and on the analysis of new trigger performance. In the last part I explain the different approach to this measurement, that I adopted here for the first time, and why it has been conceived.

The analysis presented in this document follows along the same line as the ones already performed by LHCb ([5] [40]) and it is focused in the same way to the measurement of $\mathcal{A}_{cp}$ in $D^0 \rightarrow K^0_s K^0_s$ decays. It exploits new data, in particular the ones collected by LHCb in 2017. The obtained results can be extended to the complete 2017-18 sample. Here the analysis is restarted from the beginning, in order to maximize the resolution that can be achieved also accounting for the fact that the on-line selection has been modified since the previous measurement.

4.1 2017 sample

The sample on which this analysis is performed was collected by LHCb at a center of mass energy of $\sqrt{s} = 13$ TeV and it corresponds to a total integrated luminosity of 1.7 fb^{-1}, as can be seen in Table 4.1, where also a comparison with past samples is shown. The inclusion of new data, collected in the second part of the Run-2 allows to improve the sensitivity of the analysis, adding a significant amount of statistics to the $D^0 \rightarrow K^0_s K^0_s$ decays sample, that at the current status is what limits the resolution of the measurement.

Data taking period	$\int \mathcal{L}dt$ [fb^{-1}]	$\sqrt{s}$ [TeV]
Run-1	3	7-8
Run-2 2015-2016	1.98	13
Run-2 2017	1.7	13
Run-2 2018	2.2	13

Table 4.1: Luminosity and center of mass energy for sample used in this analysis and for the ones used in Run-1 and Run-2 measurements.

4.1.1 Variables definition

Before starting to describe the trigger selection used to collect data in 2017-2018 it is necessary to give a definition of variables that will be used extensively later.

- *Primary Vertex*(PV): spatial point of the primary pp interaction.
- *Secondary Vertex*: spatial point of the decay of the particle produced in the interaction. Typically a heavy flavor hadron as a charmed or beauty hadron.
- χ^2/ndf: χ^2 obtained from the fit of a track revealed in the detector, normalized to its degrees of freedom.
- χ^2_{VVD}: squared significance of the distance between primary and decay vertex calculated using the positions and covariance matrices of the two fitted vertexes.
- p: momentum of the particle.
- p_{T}: transverse component of the particle momentum with respect to beams flight direction.
- τ: lifetime of the particle.
- τ_{BPV}: defined as $\tau_{BPV} = \mathrm{FD}/\gamma\beta c = \mathrm{FD}m/pc$, where FD is the particle flight distance between the PV and the decay vertex; it represents the time necessary for the particle to travel from the PV to its decay vertex, normalized to the particle boost.
- Pseudorapidity (η): defined as $-\log(\tan(\theta/2))$, where θ is the angle between the beams flight direction and the momentum of the particle.
- θ_{DIRA} (*direction angle*): angle between the momentum of a particle and the direction identified by the PV and the decay vertex of that particle. This angle tends to be larger in case of a partially reconstructed prompt particle, or a particle not produced in the primary pp interaction.
- $\mathcal{P}_{ghost}$: probability for the track to be a misidentified track (*ghost*); this variable is returned by a Neural Network, that exploits various variables which describe track reconstruction and global event properties in order to separate ghost tracks, which are spurious combination of hits, from real tracks.
- *Impact Parameter*(IP): distance of closest approach between the PV and the direction identified by the momentum of the particle. For a particle not produced in the PV due to the pp interaction, as K^0_{S} in the considered decay chain, this variable is more likely to assume larger values.
- χ^2_{IP}: difference between χ^2 obtained from PV fitting including or not including a particle in the fit. For a particle does not come from the PV this variable assumes larger value on average.
- $\chi^2_{\mathrm{vtx}}/\mathrm{ndf}$: χ^2 of the fit to the vertex of origin of two or more tracks, normalized to its degrees of freedom.

4.2 Trigger

As mentioned in the introduction the trigger adopted to collect LHCb events is organized in three sequential steps: L0, HLT1 and HLT2. At every trigger level, we define two different event classes, depending on how the events were collected:

- *Trigger On-Signal (TOS)*: is defined like this an event triggered directly on the presence of the signal decay chain. One or more tracks coming from it satisfied the selection criteria of the relative trigger line and the event will be recorded even if the signal process would be the only one present;

- *Trigger Independent-of-Signal (TIS)*: in this case the event has been recorded because of another process present in the same interaction. Tracks coming from that process satisfied a trigger line different from the one aimed to the signal collection.

4.2.1 L0

The first step in the selection is given by L0 trigger requirements. Several L0 configurations have been used to trigger the considered events, given by the three different lines (and even combination of these). For the purposes of the analysis not all the possible configurations can be accepted. In particular if the π_{tag} is the particle that satisfied the L0 requirements there is the possibility that this introduces a significant detection asymmetry in the sample. What is worse, the L0 processing is based on hardware threshold affected by fluctuations that are not perfectly reproducible in a simulation. The resulting asymmetry could be significantly different between our signal and control sample, and for this reason we decided not to trust the cancellation for this effect. We require, therefore, for events included in the sample that particles other the π_{tag} satisfied the L0 requirements. Doing this, the detection asymmetry due to the L0 trigger is kept under control. The two accepted configurations are when the D^0 is TOS (L0Hadron TOS) or the D^* is TIS on the global L0 decision (L0Global TIS). In the former the event is triggered because of the D^0 presence in the event, while in the latter a D^* is present in an event triggered because of other tracks.

4.2.2 Hlt1

Events present in our sample can be selected by every HLT1 line, being TIS or TOS on these, but the HLT1 lines that select most of the events are: Hlt1TrackMVA and Hlt1TwoTrackMVA. These lines search for one or two (respectively) detached high momentum good-quality track, signature of the decay distant from the primary vertex of an heavy flavor hadron.
The requirements of the first line is a track that satisfies:

- $\chi^2/\text{ndf} < 2.5$

- $\mathcal{P}_{ghost} < 0.4$

- $\{(p_{\rm T} > 25.0) \wedge (\chi^2_{\rm IP} > 7.4)\} \vee \left\{[1.0 < p_{\rm T} < 25.0] \wedge \left[\ln\chi^2_{\rm IP} > \ln(7.4) + \frac{1.0}{(p_{\rm T}-1.0)^2} + \alpha\left(1 - \frac{p_{\rm T}}{25}\right)\right]\right\}$

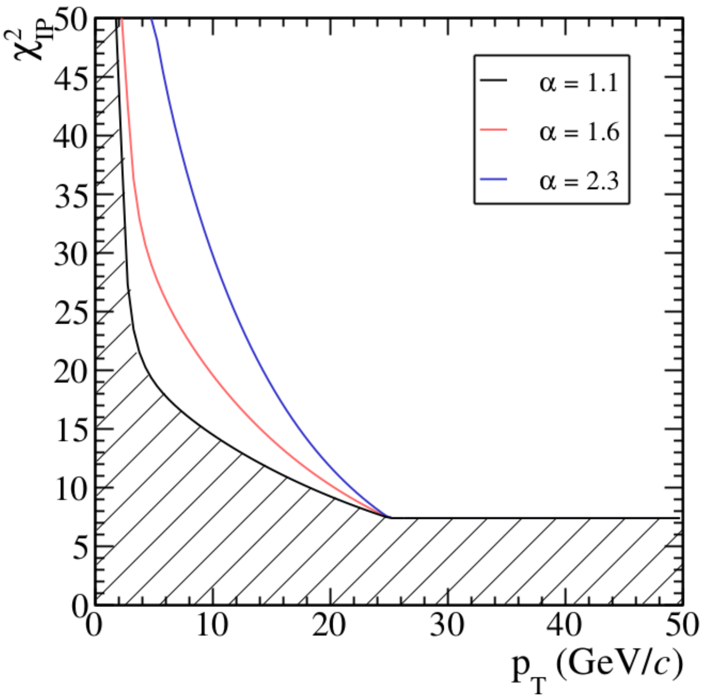

Figure 4.1: Different configurations of Hlt1TrackMVA, in terms of different α values.

here p_{T} is expressed in GeV$/c$, α is a parameter that varies during data acquisition and modifies the configuration of requirements, in a way that can be seen in Figure 4.1. The requirements for the track to considered good are represented by constraints in χ^2/ndf and in $\mathcal{P}_{ghost}$. The constraints on p_{T} and in χ^2_{IP} assure that the track has an high p_{T} and is detached from PV.

The requirements of the Hlt1TwoTrackMVA line on the single track are:

- $p_{\mathrm{T}} > 500$ MeV$/c$
- $p > 5000$ MeV$/c$
- $\chi^2/\mathrm{ndf} < 2.5$
- $\chi^2_{\mathrm{IP}} > 4$

and on the combination of the two are:

- $\chi^2_{vtx} < 10$
- $2 < \eta < 5$
- $1 < m_{corr} < 10^6$ Gev$/c^2$
- $\cos(\theta_{\mathrm{DIRA}}) > 0$
- selection on the output of a classifier calculated from the following variables: (1) χ^2 of the two-track vertex, (2) distance between the primary vertex (PV) and the two-track vertex, (3) sum of the p_{T} of the two tracks, (4) number of tracks with $\chi^2_{\mathrm{IP}} > 16$. The classifier is based on Boosted Decision Trees and should help in

selecting good quality tracks compatible with the decay of a long-lived particle. But it has been trained on b –hadron decays and therefore it is not necessarily optimal for the selection of a charm decays.

here m_{corr} (*corrected mass*) is defined as $\sqrt{m^2 + p^2_{\mathrm{T},mis}}$ and $p_{\mathrm{T},mis}$ is the missing transverse momentum needed to have the total sum of p_{T} of the daughter particle equal to zero with respect to the flight direction of the mother particle.

4.2.3 Hlt2

Events that satisfy both L0 and HLT1 requirements are then processed by many HLT2 lines, each aimed at the recognition of a certain decay pattern and the selection of those events. The lines I have chosen in this analysis are three:

- Hlt2CharmHadDstp2D0Pip_D02KS0KS0_KS0LLTurbo
- Hlt2CharmHadDstp2D0Pip_D02KS0KS0_KS0LL_KS0DDTurbo
- Hlt2CharmHadDstp2D0Pip_D02KS0KS0_KS0DDTurbo

that select respectively LL, LD and DD events.
In HLT2 tracks identified as pions are matched together to form two different K^0_{S} candidates; their four-momentum is determined from the sum of those of daughter particles. The process is repeated matching two K^0_{S}s in order to identify a D^0 candidate and matching a D^0 and a pion to identify a D^*. On those events are then applied a series of cuts, summarized in Table 4.2 and 4.3.

Variable	$K^0_{\mathrm{S}L} \to \pi^+_L\pi^-_L$	$K^0_{\mathrm{S}D} \to \pi^+_D\pi^-_D$
$\chi^2/\mathrm{ndf}(\pi)$	< 3	< 4
$\mathcal{P}_{\mathrm{ghost}}(\pi)$	< 0.4	< 0.4
$\chi^2_{\mathrm{IP}}(\pi)$	> 36	$-$
$p_{\mathrm{T}}(\pi)$	$-$	> 175 MeV$/c$
$p(\pi)$	$-$	> 3000 MeV$/c$
$\lvert m(\pi^+\pi^-) - m(K^0_{\mathrm{S}})\rvert$	< 35 MeV$/c^2$	< 64 MeV$/c^2$
$\chi^2_{\mathrm{vtx}}/\mathrm{ndf}(K^0_{\mathrm{S}})$	< 30	< 30
$\tau(K^0_{\mathrm{S}})$	> 2 ps	> 0.5 ps
$z(K^0_{\mathrm{S}}) - z(PV)$	$-$	> 400 mm
$z(K^0_{\mathrm{S}})$	$\in [-100, 500]$ mm	$\in [300, 2275]$ mm

Table 4.2: Summary of K^0_{S} selection in HLT2: two such candidates are then combined to form D^0 candidates.

The HLT2 algorithm is different from the one adopted during 2015-16 data-taking. HLT1 was requiring the presence of at least one Long track, while HLT2 was requiring the D^0 candidate to be TOS on any HLT1 line. The presence of that unwanted condition caused the absence of any DD event in the 2015-16 sample. It has been removed, allowing the collection of DD events. Downstream K^0_{S} are especially relevant for the $D^0 \to K^0_{\mathrm{S}}K^0_{\mathrm{S}}$ decay channel, seen that they are long-lived particles and approximatively 60% of the K^0_{S}

Variable	$D^0 \to K^0_{SL}K^0_{SL}$	$D^0 \to K^0_{SL}K^0_{SD}$	$D^0 \to K^0_{SD}K^0_{SD}$
$\sum_{K^0_S} p_T$	> 1500 MeV/c		
$p_T(K^0_S)$	> 500 MeV/c		
$\chi^2_{IP}(K^0_S)$	> 4		
$\chi^2_{VVD}(D^0)$	> 5		
$m(K^0_S K^0_S)$	$\in [1775, 1955]$ MeV/c^2		
$\chi^2_{vtx}/\mathrm{ndf}(D^0)$	< 10		
$\theta_{DIRA}(D^0)$	< 34.6 mrad		
$m(D^0\pi_{tag}) - m(K^0_S K^0_S)$	$\in [-75, 170]$ MeV/c^2		
$p_T(\pi_{tag})$	> 200 MeV/c		
$\mathcal{P}_{\mathrm{ghost}}(\pi_{tag})$	< 0.25		
$\chi^2/\mathrm{ndf}(\pi_{tag})$	< 3		
$\chi^2_{vtx}/\mathrm{ndf}(D^*)$	< 25		

Table 4.3: Summary of HLT2 trigger selection on D^0 candidates.

decay downstream of the VELO and can be detected only as Downstream tracks. For this reason the presence of a DD sample is important, since it offers another point of view, additional to the one given by LD sample, to understand the performances that can be achieved with Downstream tracks. One of my tasks will therefore be to analyze this new sample and evaluate its suitability for the measurement.
The other difference present between the 2015-16 and 2017 trigger algorithm are the changes introduced in the limits for HLT2 requirements, that were tuned in order to increase signal acceptance. The work on the trigger selections is an essential step for this analysis, necessary to increase the sensitivity that can be achieved, limited at the moment by the restricted size of the available sample. This has to be done in particular for trigger aimed to the detection of Downstream revealed particles. A trigger with a greater detection efficiency on these could exploit the relative abundance of K^0_S decayed after the VELO, producing larger samples, under the same event conditions.
The changes introduced in the sample in order to improve the $D^0 \to K^0_S K^0_S$ detection efficiency are the loosening of HLT2 cuts and the removal of the requirement for the D^0 to be TOS on some HLT1 line. Understand quantitatively the effect of the former changes on the detection efficiency is difficult without exploiting a Monte Carlo simulation. With the removal of the HLT1 cuts we collects also events where is the π_{tag} that triggered HLT1 and the events was collected as TIS on HLT1. Therefore we include in the sample events where, for the LL channel, pions coming from K^0_S decays did not triggered HLT1 and events where, for the LD channel, pions coming from the Long K^0_S did not triggered HLT1. We can suppose that the improvement should be bigger for the LD channel with respect to the LL one. Therefore verifying the effective improvement in signal event acceptance due to the adoption of the new trigger has been crucial, since the introduced changes and their efficacy can be used as a baseline for future trigger upgrades.

4.3 2017 sample preliminary analysis

Due to the novelties in the sample, it is essential to examine it preliminary before any more complex study to understand how it behaves and if there are some major differences with past samples that should be taken into account during the analysis. The first necessary thing is an estimate of signal yields and comparison with the past.
The main observable I use in evaluating yields is the Δm, as explained in Chapter 3. Therefore I started taking a first look at Δm distribution of each of three channels without the application of any other cut excepting for trigger and fiducial cuts. In this preliminary analysis I will use kinematic variables produced by the Loki Fitter (derived directly from measured four-momenta, with only vertex constrain applied). This excepting for Δm calculation, because in the Loki fitter D^0 and D^* masses are computed by fitting separately the two vertex particles, and procedure can distort Δm distribution, especially for events where the vertex resolution is worse. For this reason, to have a coherent calculation of these masses, I computed in this preliminary analysis D^* mass from the D^0 and π_{tag} four-momenta and then computed Δm from this.
Δm distributions for 2017 sample with application of only the two mentioned set of cuts, are shown in Figure 4.2, 4.3 and 4.4, for the three main subsamples of my interest. The

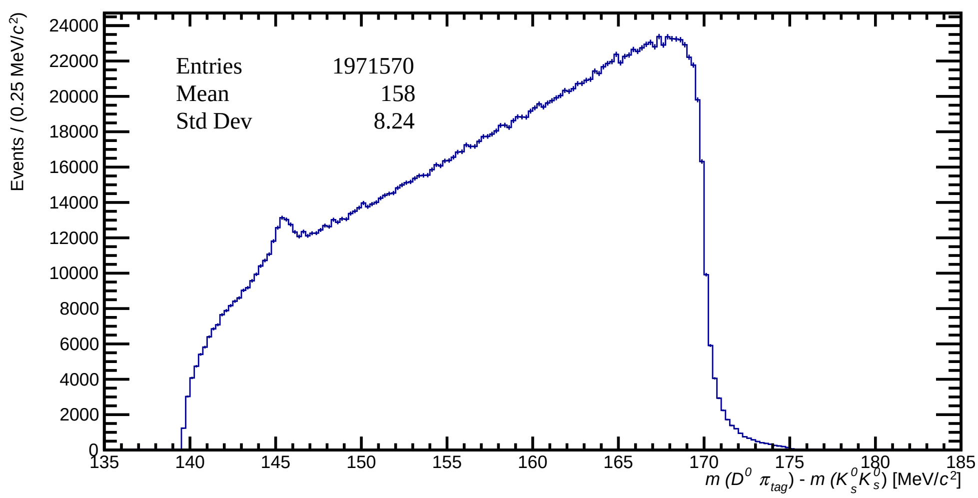

Figure 4.2: Δm distribution for LL channel, with only trigger, L0 and fiducial cuts.

three distributions have different shapes. The signal contribution can be noticed at a $\Delta m \simeq 145.5$ MeV$/c^2$. This value is given by the difference between the mass of a real D^* and a real D^0 when part of the decay chain considered in this analysis. The presence of the signal is discernible only for the LL and LD channel, while it is not for the DD channel. At this level there is however still a large background in the continuum distribution (combinatorial) and also in the peak region - as will be discussed later.
Other important observables are obviously the mass distribution of D^0 and K^0_S candidates, shown in Figure 4.5, 4.6 and 4.7. For K^0_S candidates mass distributions the presence of real K^0_S is proved by the significant peak centered at K^0_S mass. The peak in the D^0 candidates mass distributions is significantly lower and it can be discerned only for LL and LD channels, as happens for the Δm distributions. The resolution on invariant mass worsens from LL to LD and DD channel. This trend is expected, due to lack of precision

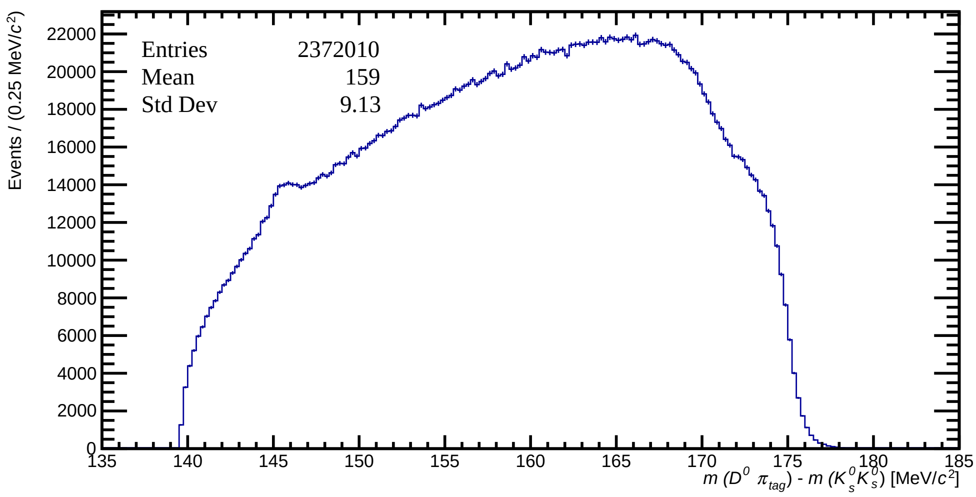

Figure 4.3: Δm distribution for LD channel, with only trigger, L0 and fiducial cuts.

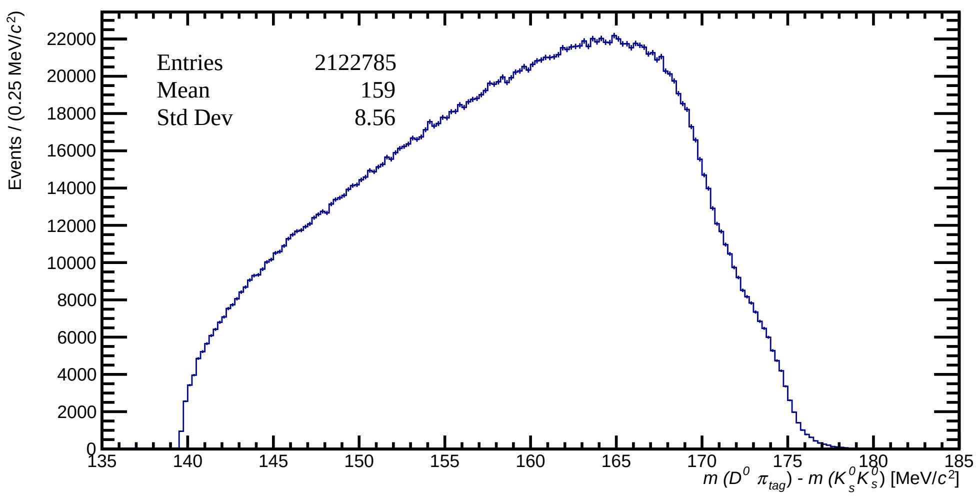

Figure 4.4: Δm distribution for DD channel, with only trigger, L0 and fiducial cuts.

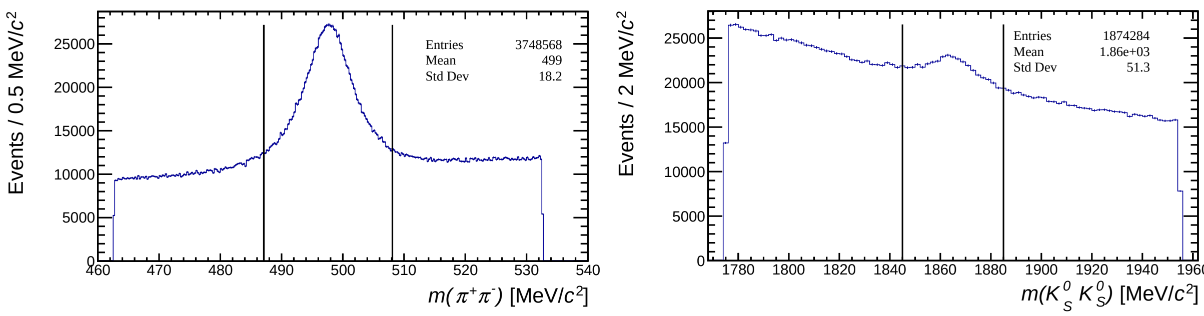

Figure 4.5: K^0_S (left) and D^0 (right) mass distributions for LL channel candidates, with only trigger and fiducial cuts. Vertical lines indicate the chosen values for the mass cuts.

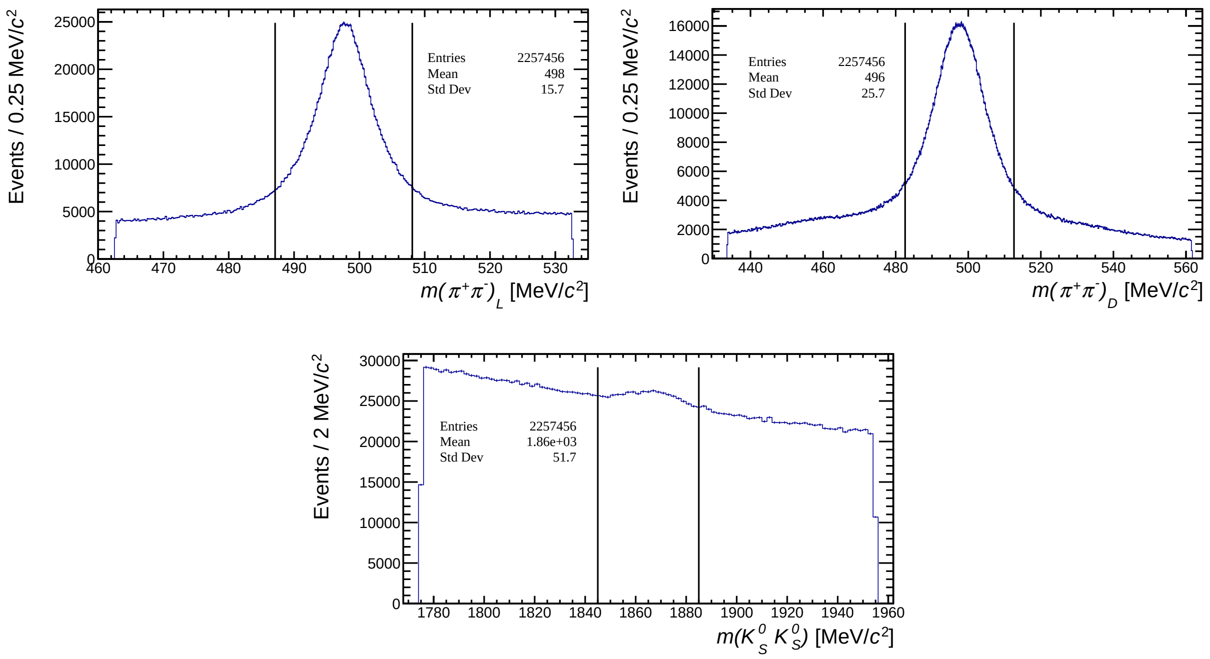

Figure 4.6: K^0_S Long (top left), K^0_S Downstream (top right) and D^0 (bottom) mass distributions for LD channel candidates, with only trigger and fiducial cuts. Vertical lines indicate the chosen values for the mass cuts.

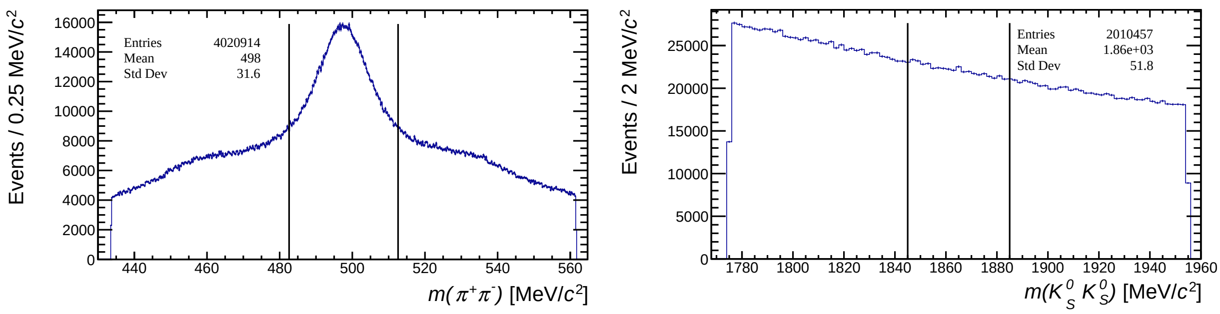

Figure 4.7: K^0_S (left) and D^0 (right) mass distributions for DD channel candidates, with only trigger and fiducial cuts. Vertical lines indicate the chosen values for the mass cuts.

VELO points in the Downstream tracks. In all distributions is clear the presence of a large background contribution; this was expected. The trigger selections are designed to obtain the largest signal acceptance and this causes also a large background acceptance. Other interesting variables are the momentum distributions of particles involved in the process. In Figure 4.8, 4.9 and 4.10 the momentum distributions are shown. The distribution of kinematic variables are similar between different channels, since the adoption of different detectors does not significantly influence the acceptance. In the K^0_S momentum distribution for the LD channel two different trends can be discerned. This is due to the presence of TIS and TOS events. These two have two different momentum distribution because they are collected through separate trigger lines, that differently influence the events kinematics. In particular, TOS events have a larger momentum on average, since for these one of the tracks present in the event directly satisfied one of the trigger

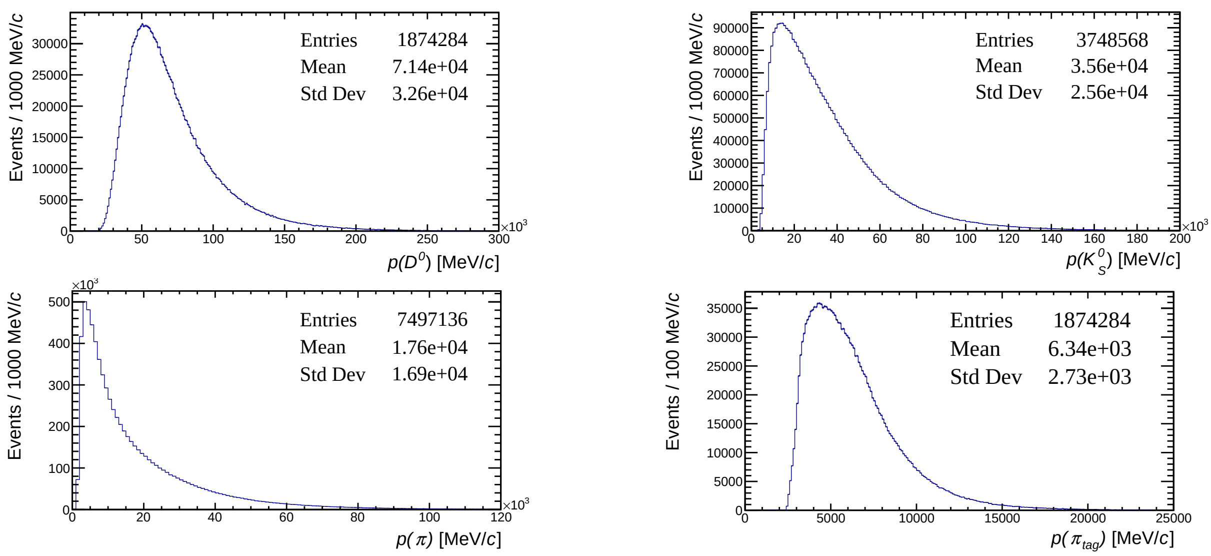

Figure 4.8: D^0 (top left), K^0_S (top right), π coming from K^0_S decay (bottom left) and π_{tag} (bottom right) momentum distributions for LL channel, with only trigger, L0 and fiducial cuts.

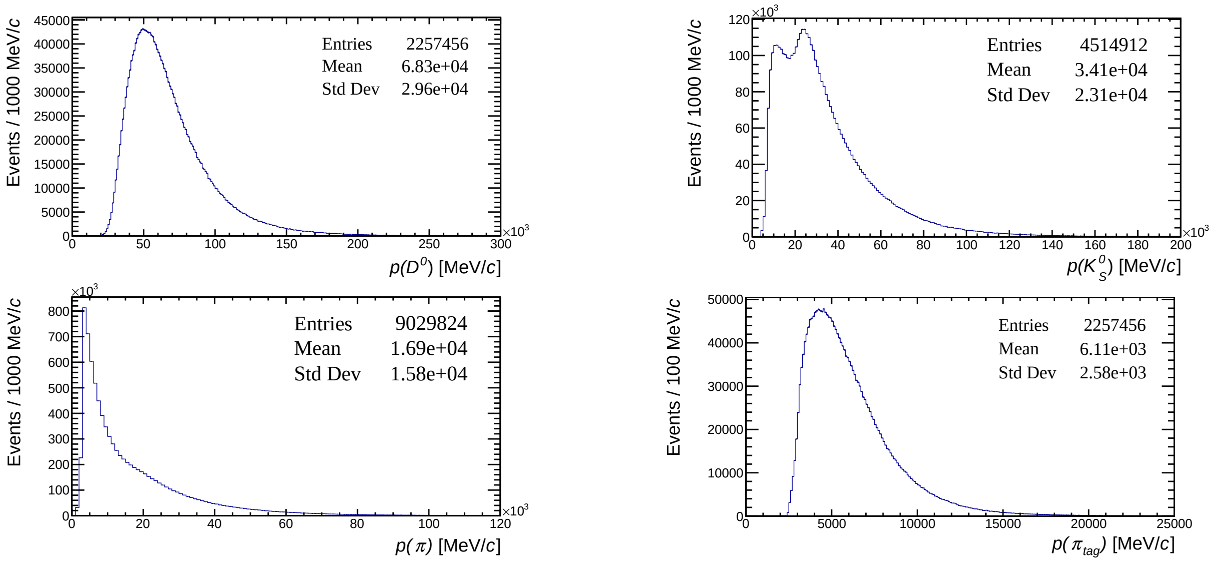

Figure 4.9: D^0 (top left), K^0_S (top right), π coming from K^0_S decay (bottom left) and π_{tag} (bottom right) momentum distributions for LD channel, with only trigger, L0 and fiducial cuts.

requirements, based on momentum, too.

4.3.1 Background classification

The main contributions to background in analyzes performed so far, involving charmed hadrons can be categorized in three classes: combinatorial background, prompt peaking background and secondary decays.
Combinatorial background is produced by fake K^0_S, D^0 and D^* candidates. Those are not real particles, they are wrongly reconstructed matching two random particles or candidates

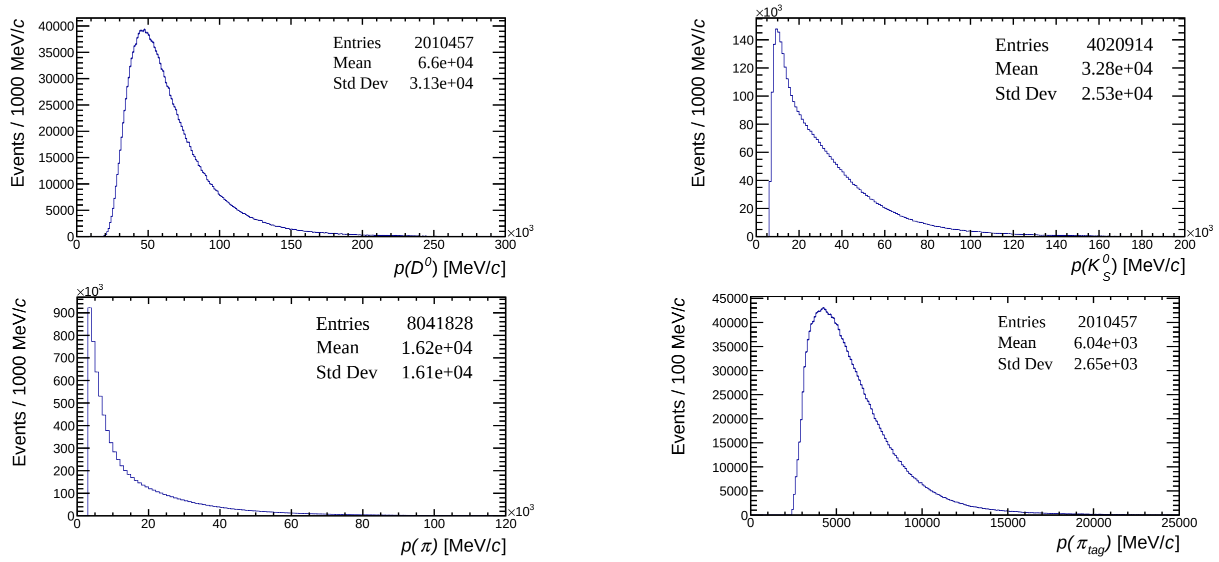

Figure 4.10: D^0 (top left), K^0_S (top right), π coming from K^0_S decay (bottom left) and π_{tag} (bottom right) momentum distributions for DD channel, with only trigger, L0 and fiducial cuts.

present in the event, whose trajectories accidentally cross each other and form a good vertex. This kind of background does not peak in Δm distribution and contributes to the continuous component. This because it is given by fake particles, that do not have the mass of the real candidates and does not respect kinematic constrain.
The peaking background contribution is produced by events where a real D^* decays into a D^0, that reaches the same four-pion final state of $D^0 \to K^0_S K^0_S$ decay through a different decay channel. The largest contribution to this kind of background is given by $D^0 \to K^0_S \pi\pi$ and $D^0 \to \pi\pi\pi\pi$ decay. These decay channels for D^0 are prevailing because they shares the same final state with the signal and because of their branching ratio, two order of magnitudes larger than our signal. These events give a peaking contribution to Δm because both D^* and D^0 are real in these events and the decay configuration of the D^* is equal to that of signal events. For this reason they have to be carefully removed.
Secondary decays are events where the D^* is not produced in the primary pp interaction, but it comes from the decay of a b-hadron. The decay configuration of these, and prompt events, can be better understood looking at Figure 4.11. These events have the same

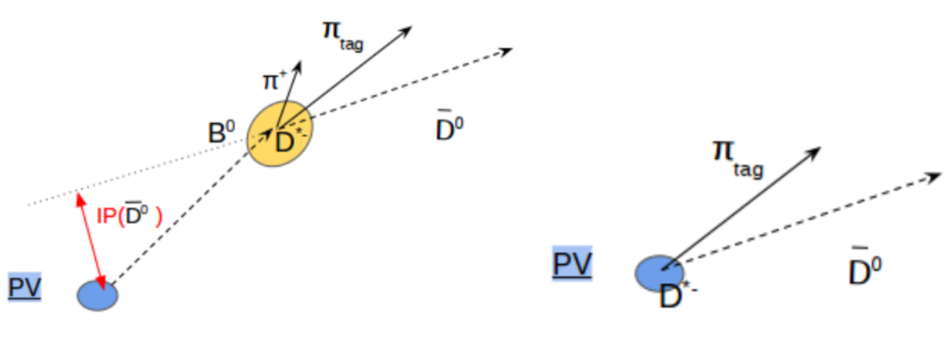

Figure 4.11: Schematic representation of the decay topology of secondary (left) and prompt (right) decays. It emerges that for the former $\chi^2_{\rm IP}$ (D^0) and $\chi^2_{\rm IP}$ (π_{tag}) assumes larger values.

physical properties of those promptly produced, but different production asymmetry, that influences the $\mathcal{A}^{prod}$ value. Therefore $\mathcal{A}^{prod}$ is given by two different contributions, from D^* and any b-hadron production asymmetry:

$$\mathcal{A}^{prod} = \left(1 - \sum_i f_i\right) \mathcal{A}^{prod}{}_{D^*} + \sum_i f_i \mathcal{A}^{prod}{}_i \tag{4.1}$$

where f_i denotes the fraction of secondary candidates coming from the decay of a certain b-hadron, and the index i runs over all b-hadrons. For secondary decays the production asymmetry assumes a different value because of the different asymmetry in the b-hadrons cross section and additionally because of the influence of *CPV* effects occurring in the b-hadron decays. While it is in principle possible to measure the production asymmetry of b-hadrons (and to some extent it has been done [6]), the overall effect given by the mixture of the different b-hadron species on the D^* production asymmetry is extremely hard to evaluate precisely, since each one contributes with a different weight (corresponding to f_i), with both production and *CP* asymmetries (some still not measured). This would not be a problem, if the signal and calibration channel were composed by exactly the same mixture of prompt and secondary decays, that would assure cancellation of the unknown effect between the two. In reality it is really difficult to obtain two samples with this feature, since already at trigger level cuts that can differently bias the fraction of secondary decays are applied. When the two fractions are different, the $\mathcal{A}^{prod}$ assume different values for signal and control channel, introducing a bias in the $\mathcal{A}^{CP}$ extraction. For these reasons the usual LHCb approach to secondary decays is to reject them with appropriate cuts, to force their fraction in the sample to zero, avoiding any bias.

As a first step we would like to evaluate the yields of the samples before performing any significant selection, in order to understand the "starting point" provided to us by the new trigger selection adopted in 2017. In particular, in order to allow a meaningful comparison with older data samples, we want to avoid any selection cuts whose efficiency may be affected by factors, other than the trigger, that may have changed (*e.g.* subtle resolution/alignment effects). However, in order to extract even an appropriate estimate of signal yields from presented distributions it is necessary to reduce the high level of background present in these plots. In particular, peaking background events must be strongly rejected before fitting, in order to avoid getting misleading results. Continuous component does not cause any bias on signal yield, but its presence worsens the sensitivity that can be achieved on yield.
We therefore need to apply at least a minimal set of cuts, that we will refer to as our "fiducial selection" in the following.

4.3.2 Mass cuts

First selection that has been applied is a series of rectangular cuts on mass of reconstructed candidates, hence K^0_S and D^0. A cut on D^* mass is not applied, as it would reflects on a cut on Δm distribution, that will be fitted to extract number of signal events.
These sample cuts are reliably almost-full efficient on signal, while being extremely powerful in rejecting combinatorial background because if the candidate is given by a random intersection of two particle trajectories present in the event, the invariant mass of the

candidate does not have to correspond to the mass of the real particle. This works both for random pions that are matched to fake K^0_S and random K^0_S matched to fake D^0.
The cut on K^0_S mass also reject peaking background, as in case of a $D^0 \to K^0_S\pi\pi$ decay, only one of the pion pairs present in the final state come from a real K^0_S and its invariant mass corresponds to the K^0_S mass. On the other hand, for the other pair in the decay there is a small probability to have an invariant mass near the value of the mass of a real K^0_S.
The cut ranges have to be selected taking into account the resolution on masses, of K^0_S and D^0. If the applied cut is too tight it rejects also real particles, that have an invariant mass distant from the real value because of the finite resolution on momentum measurement, and this needs to be avoided.
Selected mass windows are:

- $|m(K^0_S) - 497.6\,\mathrm{MeV}/c^2| < 10.5\ \mathrm{MeV}/c^2$ and $|m(D^0) - 1865\,\mathrm{MeV}/c^2| < 20\ \mathrm{MeV}/c^2$ for LL channel;
- $|m(K^0_S) - 497.6\,\mathrm{MeV}/c^2| < 10.5\ \mathrm{MeV}/c^2$ for K^0_S detected as Long tracks $|m(K^0_S) - 497.6\,\mathrm{MeV}/c^2| < 15\ \mathrm{MeV}/c^2$ for K^0_S detected as Downstream tracks and $|m(D^0) - 1865\,\mathrm{MeV}/c^2| < 20\ \mathrm{MeV}/c^2$ for LD channel;
- $|m(K^0_S) - 497.6\,\mathrm{MeV}/c^2| < 15\ \mathrm{MeV}/c^2$ and $|m(D^0) - 1865\,\mathrm{MeV}/c^2| < 20\ \mathrm{MeV}/c^2$ for DD channel.

Reported in Figure 4.5, 4.6 and 4.7. From the area of the histogram out of mass window it is possible to gauge the effectiveness of these cuts on excluding a large amount of background otherwise present in the sample.

4.3.3 Flight distance cuts

A fraction of peaking background events is still present after the application of mass cuts, even if they are highly effective on reducing background contribution to the sample. This happens because there is the possibility for a pion pair do not coming from the decay of a K^0_S to randomly have an invariant mass near to K^0_S mass and hence to pass the already applied cuts. For this reason it is necessary to apply other cuts to reject $D^0 \to K^0_S\pi\pi$ events.
There is another relevant difference between $D^0 \to K^0_S\pi\pi$ and $D^0 \to K^0_S K^0_S$ events that allows to distinguish them. It is based on the flight distance of the K^0_S candidate. K^0_S is a long-lived particle and it is possible to be sensitive on its flight distance, *e.g.* the difference between the PV of the event and its decay vertex. For fake K^0_S coming from $D^0 \to K^0_S\pi\pi$ decays the flight distance is smaller with respect to the one of a real K^0_S. The variable I used is not directly K^0_S flight distance, but it is the z-projection (z_{FD}) of the distance between the decay vertex of the K^0_S and the PV. The use of this simple variable allows to distinguish between real and fake K^0_S coming from $D^0 \to K^0_S\pi\pi$ in an efficient way. I preferred to do not adopt more complex variables, as $\chi^2\ _{FD}$, since these are sensitive to vertex position and resolutions.
This can be better understood looking at the plot in Figure 4.12. Here a double check can be made: K^0_S not only fly for a distance that is significantly different from zero, but they also cluster in mass distribution and can be better identified. In Figure 4.12 K^0_S reconstructed with Long and with Downstream tracks are superimposed, therefore the

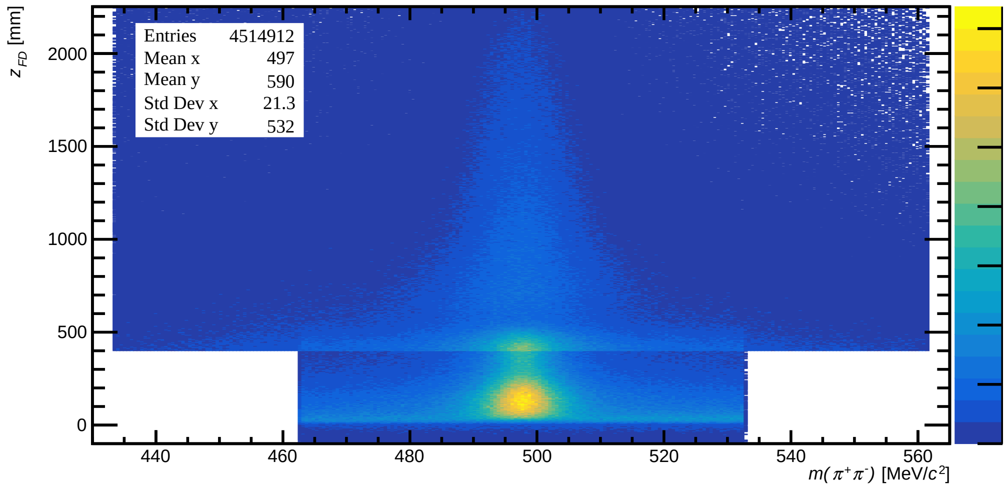

Figure 4.12: Scatter plot of reconstructed mass of K^0_S on x-axis and z-projection of K^0_S flight distance on y-axis, for LD channel, with only trigger and fiducial cuts.

plot sums up all the information necessary to understand the value of the cut that has to be applied. For K^0_S revealed with Downstream tracks it is not necessary to apply any cut on z_{FD}, since by definition a Downstream track it is detected without exploiting VELO hits and hence the particle traveled for at least 400 mm (where the VELO ends) after the PV; this distance is much larger than the cut that will be applied.
Observing plot in the region of events populated by Long tracks it is clearly visible an events cluster around K^0_S mass, detached from zero in z_{FD}. The cut has to select these events.
To better understand which cut value should be applied for Long tracks it is useful to look at Figure 4.13. Here it is reported the same plot as in Figure 4.12, selecting region at small z_{FD}. It is more clear the presence of the events cluster described before and it is visible a group of events with different K^0_S mass but smaller z_{FD}, given by $D^0 \to K^0_S\pi\pi$ events. The chosen value for the cut to exclude the presence of a peaking background is z_{FD} = 60 mm. This cut has an high efficiency on real K^0_Ss, since these fly, in this sample, for an average distance equal to $\gamma\beta c\tau \simeq 68 \cdot 2.7\,\text{cm} = 180\,\text{cm}$. Plots like the one present in Figure 4.12 for LL and DD channels are not reported here, since they do not give significant additional information.

4.4 Signal yield estimate

After the application of these cuts I give a first estimate of the signal yields for the three channels.

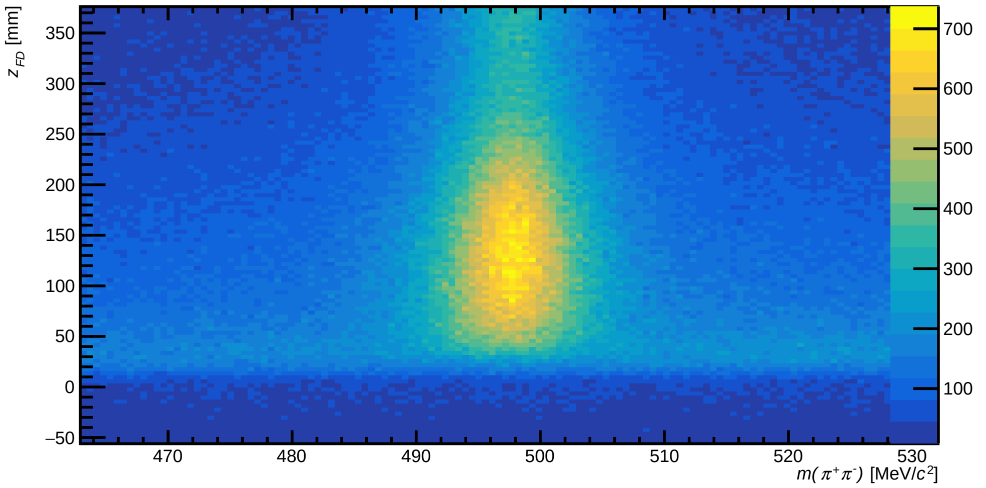

Figure 4.13: In Figure are plotted reconstructed mass of K^0_S on x-axis and z-projection of flight distance for LD channel, highlighting region at small z_{FD}.

4.4.1 Fit model

The function used to fit histograms is the sum of two components, corresponding to signal and background events. To shape the signal peak a Gaussian *p.d.f.* was chosen:

$$f_{sig}(x) \propto \frac{1}{\sqrt{2\pi\sigma^2}} \exp\left\{\frac{(x-\mu)^2}{2\sigma^2}\right\} \tag{4.2}$$

where mean μ and σ are free parameters. And to model the background contribution an empirical *p.d.f.* was adopted:

$$f_{bkg}(x) \propto 1 - \exp[-c(x-m_\pi)] + b(x-m_\pi) \tag{4.3}$$

where b and c are free parameters.
A maximum likelihood fit is performed, where the likelihood assumes the form:

$$\mathcal{L} = \frac{e^{-N_{exp}} N_{exp}^{N_{obs}}}{N_{obs}!} \prod_{i=1}^{N_{obs}} \frac{[n_{sig} \cdot f_{sig}(x) + n_{bkg} f_{bkg}(x)]}{n_{sig} + n_{bkg}} \tag{4.4}$$

where n_{sig} and n_{bkg} are the yields for signal and background, respectively, $N_{exp} = n_{sig}+n_{bkg}$ and N_{obs} is the number of observed events.

4.4.2 Yield values

With the rejection of peaking background contribution it is meaningful to give a first estimate of signal yields fitting Δm histograms for three channels. The Δm histograms are shown in Figure 4.14, 4.15 and 4.16, together with performed fits. As can be seen, there is only a weak signal evidence for DD channel. Here, to extract the yield value, I fixed the shape of the signal peak and fitted only the number of signal events. The mean of the Gaussian was fixed to 145.4 MeV/c^2, the standard deviation to the value extracted from fit to LD channel.

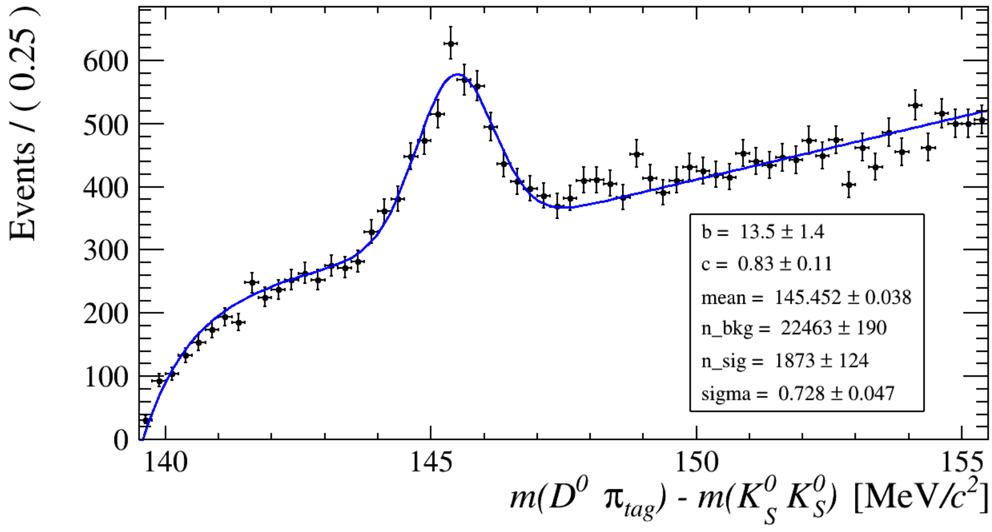

Figure 4.14: Δm distribution and relative fit for LL channel, after the application of cuts on K^0_S and D^0 mass and z_{FD}.

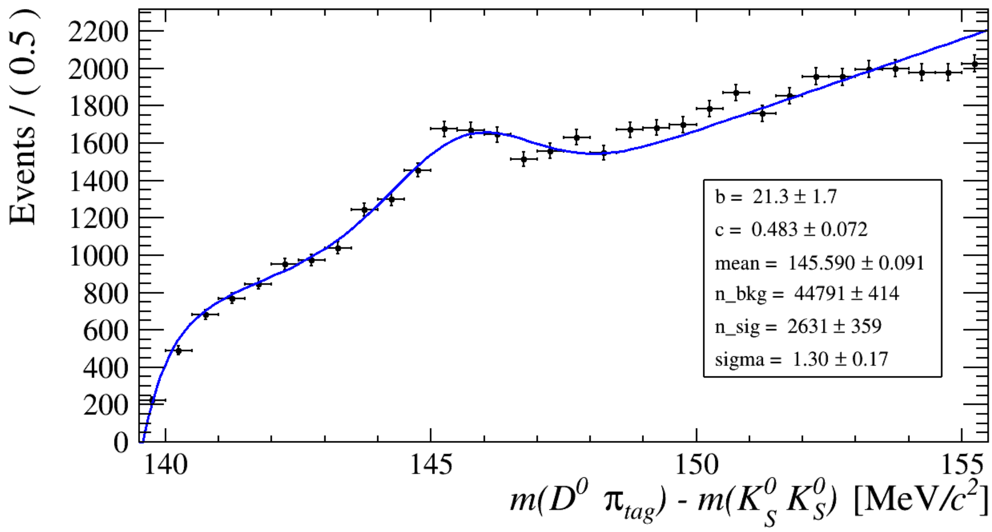

Figure 4.15: Δm distribution and relative fit for LD channel, after the application of cuts on K^0_S and D^0 mass and z_{FD}.

We can now make a comparison between number of signal events collected in 2017 sample and 2015-16 sample; to do this properly, I had to go back to original 2015-16 data and rerun the selection. The comparison is summarized in Table 4.4. This procedure allows

sample	Integrated luminosity	LL	LD	σ_{LL} [fb]	σ_{LD} [fb]
2015-16	1.98 fb^{-1}	1701 ± 116	1437 ± 115	859 ± 59	726 ± 58
2017	1.7 fb^{-1}	1873 ± 124	2631 ± 359	1102 ± 73	1548 ± 211

Table 4.4: Signal yields for LL and LD channels after cuts K^0_S and D^0 masses and z_{FD}. σ here represents the cross section times detection efficiency and geometrical acceptance (extracted as number of signal yields divided by number of fb^{-1}).

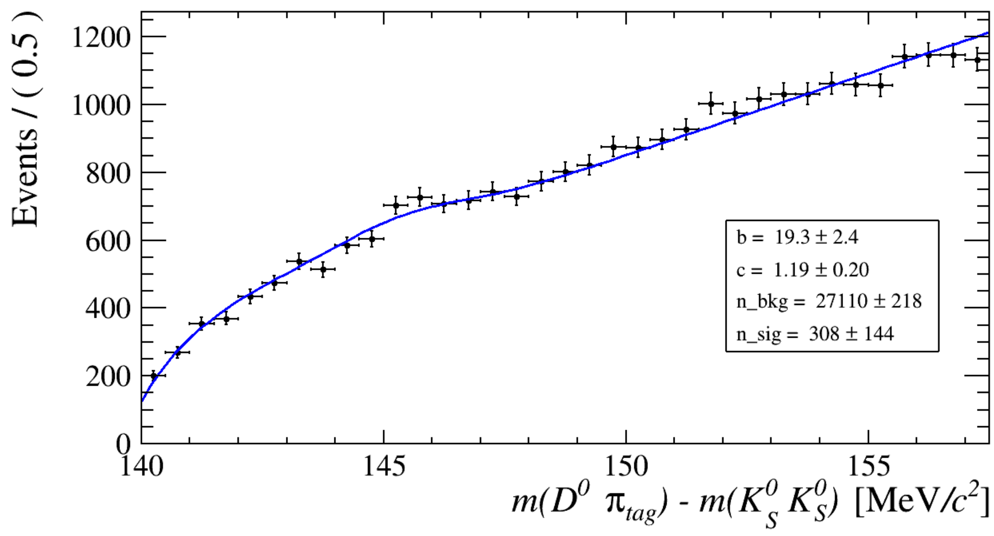

Figure 4.16: Δm distribution and relative fit for DD channel, after the application of cuts on K^0_{S} and D^0 mass and z_{FD}.

to make a comparison between the two trigger selections adopted in the data-taking. My results confirm that the 2017 sample contains more signal events per collected fb^{-1}, showing a better detection efficiency. The enhancement of the trigger efficiency from 2015-16 to 2017 corresponds to a factor of ~ 1.3 for LL channel, and this is even bigger for the LD channel, where it is equal to ~ 2.1.
In the next section I will start considering the possibilities for further improving this performance, beyond what was given by the trigger.

4.5 The issue of secondary decays rejection

The sample identified from the cuts applied so far still contains secondary decays. As mentioned before, they can bias the $\mathcal{A}^{CP}$ extraction, and the standard approach in LHCb is to reject them with appropriate cuts. We will now discuss however, why this is a bigger issue in the channel of our interest, than in other charm asymmetry measurements. The variables that mostly allows to distinguish prompt and secondary decays are the χ^2_{IP} (D^0) and χ^2_{IP} (π_{tag}), and the χ^2_{VVD} (D^*), since, for a particle not coming from the PV, these assume on average a larger value.
Applying a cut on χ^2_{IP} (π_{tag}) and χ^2_{IP} (D^0) it is possible to select prompt events, where the D^* comes from the PV. χ^2_{IP} distributions are shown in Figure 4.17, 4.18 and 4.19.
In these distributions it is possible to see two different trends: a peak at small χ^2_{IP} values and a contribution at higher values. The first is due to prompt events, the second one is given by secondary decays. The cuts applied on π_{tag} and D^0 χ^2_{IP} to reject secondary decays in the sample are:

- $\log(\chi^2_{IP}(D^0)) < 3$ and $\log(\chi^2_{IP}(\pi_{tag})) < 2$ for LL channel;
- $\log(\chi^2_{IP}(D^0)) < 4$ and $\log(\chi^2_{IP}(\pi_{tag})) < 3.5$ for LD channel;
- $\log(\chi^2_{IP}(D^0)) < 4$ and $\log(\chi^2_{IP}(\pi_{tag})) < 3.5$ for DD channel;

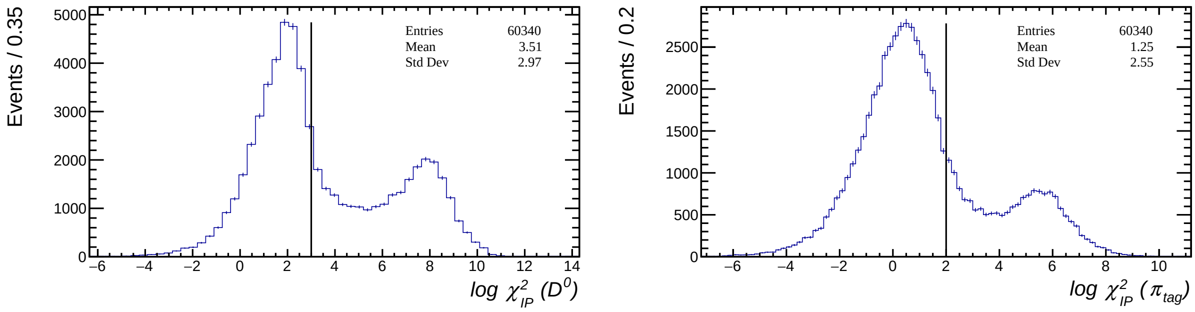

Figure 4.17: χ^2_{IP} (D^0) (left) and χ^2_{IP} (π_{tag}) (right) distributions for LL channel. Cuts on $m(K^0_{\mathrm{S}})$ and $m(D^0)$ and z_{FD} are applied. The vertical line represents the applied cut on the variable.

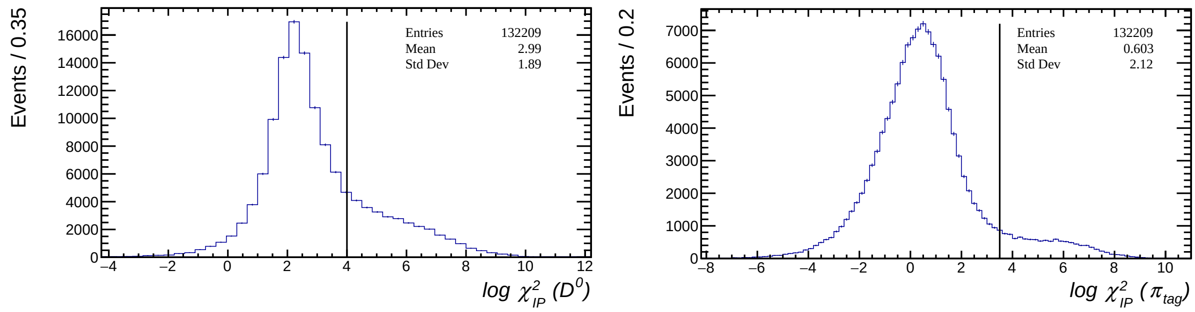

Figure 4.18: χ^2_{IP} (D^0) (left) and χ^2_{IP} (π_{tag}) (right) distributions for LD channel. Cuts on $m(K^0_{\mathrm{S}})$ and $m(D^0)$ and z_{FD} are applied. The vertical line represents the applied cut on the variable.

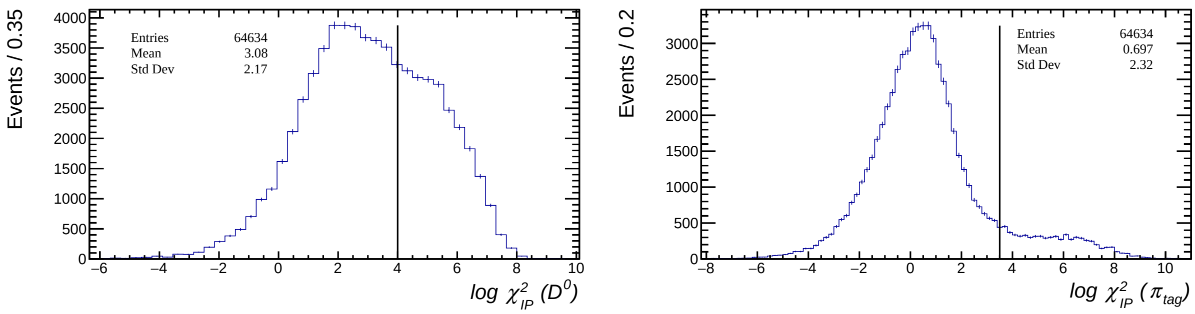

Figure 4.19: χ^2_{IP} (D^0) (left) and χ^2_{IP} (π_{tag}) (right) distributions for DD channel. Cuts on $m(K^0_{\mathrm{S}})$ and $m(D^0)$. The vertical line represents the applied cut on the variable.

These cuts are the ones applied in the most recent analysis, shown in [39]. Here the cuts have been chosen looking at Monte Carlo simulation for the $D^0 \to K^0_{\mathrm{S}} K^0_{\mathrm{S}}$ events, for both prompt and secondary decays. Since no significant difference between the distributions of these variables because of the different trigger is expected, the same cuts are applied.
The other considered variable is the χ^2_{VVD} (D^*). It represents the compatibility between the PV and the D^* decay vertex. Therefore even this variable assumes larger values when the D^* in the event is not promptly produced. The χ^2_{VVD} (D^*) distributions for the three channels are shown in Figure 4.5. The trend is similar to the χ^2_{IP} one, where the events at smaller χ^2_{VVD} are prompt ones, while for the secondary decays that variable assumes

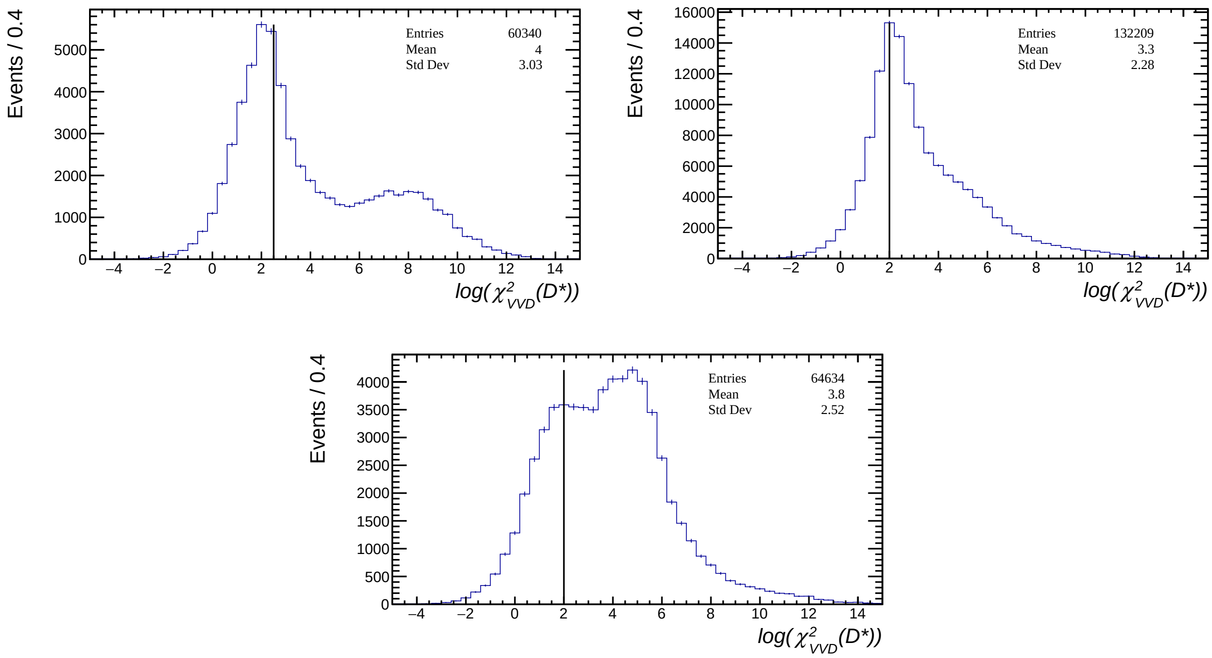

Figure 4.20: LL (up left), LD (up right) and DD (down) channels χ^2_{VVD} distributions. Cuts K^0_{S} and D^0 mass and z_{FD} are applied. The vertical line represents the applied cut on the variable.

larger values.
The cuts applied on the χ^2_{VVD} (D^*) to reject secondary decays are:

- $\log(\chi^2_{\mathrm{VVD}}(D^*)) < 2.5$ for LL channel;
- $\log(\chi^2_{\mathrm{VVD}}(D^*)) < 2$ for LD channel;
- $\log(\chi^2_{\mathrm{VVD}}(D^*)) < 2$ for DD channel;

After the application of these cuts it is useful to extract the signal yields, fitting Δm histograms. This allows to understand the effects of these cuts. Histograms and fits about the sample after the rejection of secondary decays are shown in Figure 4.21, 4.22 and 4.23. To fit DD channel distribution I fixed mean and standard deviation of the Gaussian $p.d.f.$ to the value extracted from the LD channel fit.

4.5.1 Signal event rejection

In Table 4.5 a comparison between signal yields before and after secondary decays is summarized. From these data it is clear that with the application of cuts on χ^2_{IP} and χ^2_{VVD} to remove secondary decays takes place also a significant loss of signal events. This happens in every channel, but not with the same magnitude: the effect on LD events is more than twice the one on LL and DD events. Even if it should be noticed that the uncertainty on the DD yields it is comparable to the value of the fraction of lost events. This is not a feature of the 2017 sample only: by looking at 2015-16 numbers ([39]) we can see that the same effect was present there. This shown that the rejection of secondary decays causes a significant drop in event yields.

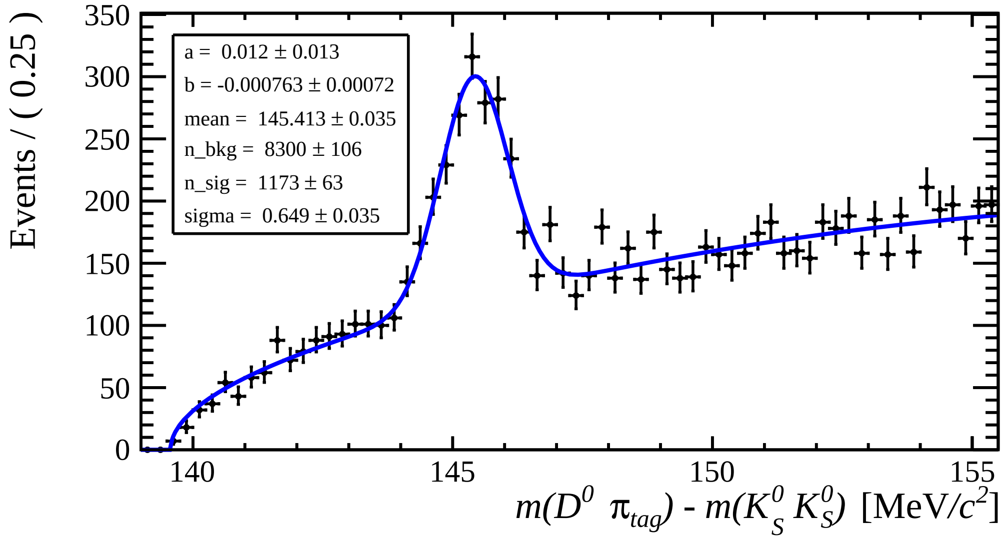

Figure 4.21: Δm distribution and relative fit for LL channel, after the application of cuts on K^0_{S} and D^0 mass, z_{FD}, χ^2_{IP} and χ^2_{VVD}.

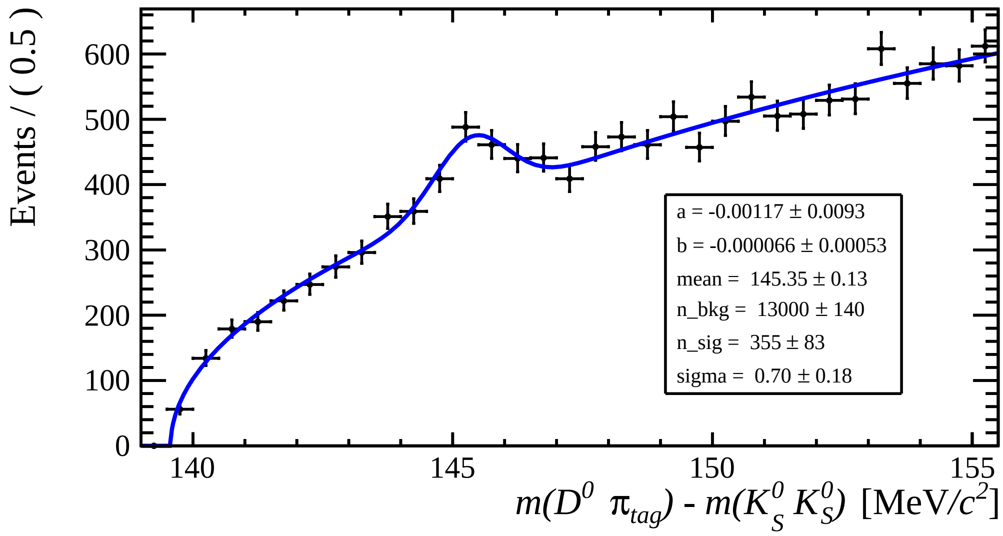

Figure 4.22: Δm distribution and relative fit for LD channel, after the application of cuts on K^0_{S} and D^0 mass, z_{FD}, χ^2_{IP} and χ^2_{VVD}.

Sample	Before χ^2_{IP} and χ^2_{VVD} cuts	After χ^2_{IP} and χ^2_{VVD} cuts	Cut efficiency
LL	1873 ± 124	1173 ± 63	63 %
LD	2631 ± 359	355 ± 83	15 %
DD	308 ± 144	12 ± 33	65 %

Table 4.5: Comparison between signal yields for 2017 sample before and after rejection of secondary decays.

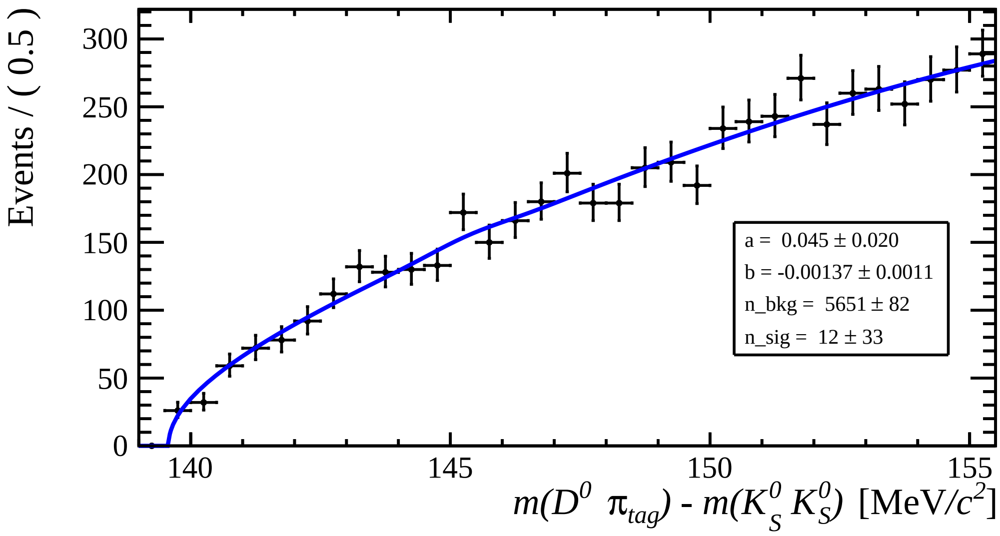

Figure 4.23: Δm distribution and relative fit for DD channel, after the application of cuts on K^0_{S} and D^0 mass, z_{FD}, χ^2_{IP} and χ^2_{VVD}.

Chapter 5

An improved approach to the analysis

In this chapter I analyze several variables exploited to distinguish signal to background component present in the sample. After I identify with an automated procedure the cuts configuration that maximize the resolution that can be achieved.

In this part of the work I want to obtain the best resolution on $\mathcal{A}^{CP}$ with the adoption of the new strategy. To achieve this result it is necessary to identify and optimize a set of cuts that allows to reject backgrounds, in both peaking and combinatorial component and that do not apply any bias on the fraction of secondary decays. This implies that we should not make any cut whose efficiency depends on the location of the decay vertex of the D^* particle relative to the PV. We will refer to this as a "vertex unbiased" selection. To figure out the effect of the new strategy and to make a comparison with the alternative strategy it is necessary, after the cuts application, to extract a value for the resolution for the two selections that will be identified. This is not done in this analysis for the DD channel, because of the small evidence of signal that was found that makes difficult a significant comparison and shows little promise of contributing significantly to the final result.
The analysis will be performed in the LL and LD channel separately, in order to achieve the best possible resolution.

In the previous chapter a significant signal event loss was verified in case of the rejection of secondary decays. Why this happens can be better understood looking at the variables that allows the determination of χ^2_{IP} and χ^2_{VVD}, and therefore on which the distinction between prompt and secondary decays is based.
The signal events loss is due to the difficulty in distinguishing between D^0 coming from prompt and secondary decays. Why this happens, and why this trend between channels appears, can be clearly understood by looking at the shown χ^2_{IP} (D^0), χ^2_{IP} (π_{tag}) and χ^2_{VVD} (D^*) distributions. χ^2_{IP} offers a good separation between prompt and secondary decays only when the uncertainty on the D^0 decay vertex position is smaller than the mean value of the difference between IP of secondary and primary decays. This condition does not happen in the reconstruction of neutral and long-lived particles as K^0_{S}. In this case the vertex resolution is not good enough, in particular the vertex that affects most the determination of the χ^2_{IP} is the D^0 decay vertex[1]. The uncertainty on the D^0 vertex

[1] χ^2_{IP} is in reality determined also from the D^0 momentum direction, but with a parallel $p(D^0)$ translation, the uncertainty on the D^0 decay vertex reflects directly on the uncertainty on the distance between

position for the three channels is shown in Figure 5.1. It is possible to see a strong decrease

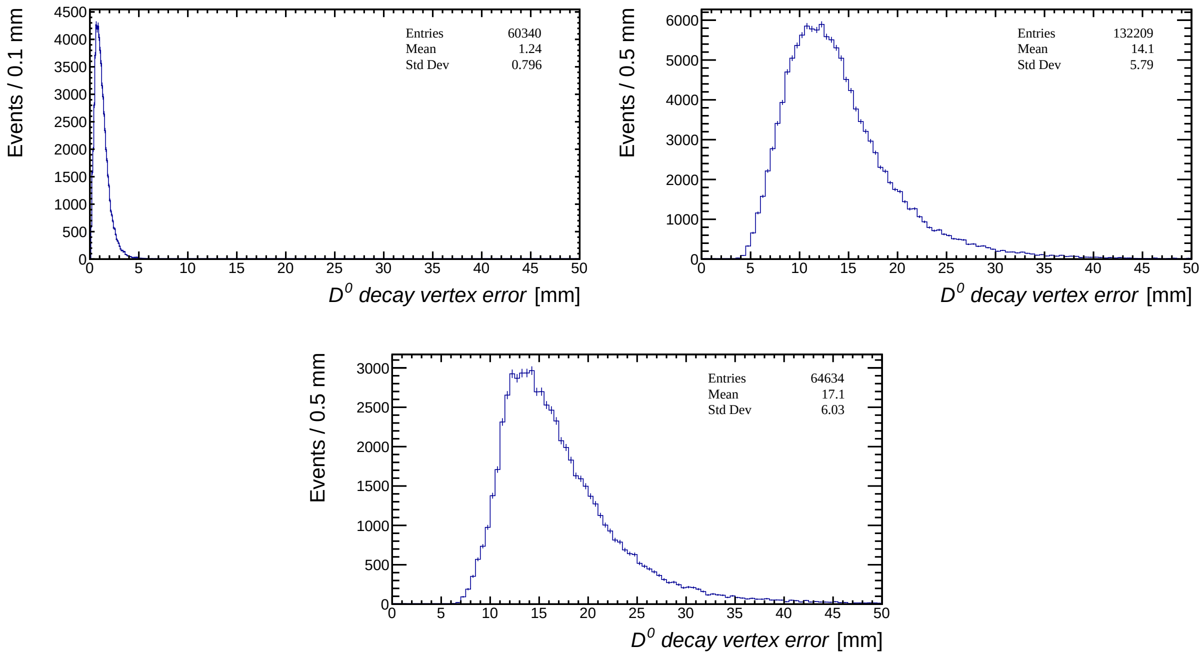

Figure 5.1: LL channel (top left), LD channel (top right), DD channel (bottom) uncertainty on the D^0 decay vertex position distribution, for LL channel.

of the sensitivity from LL to LD and DD channels. The mean values of the resolutions on the D^0 decay vertex are equal to 1.2 mm, 14 mm and 17 mm, for LL, LD and DD channel, respectively. The expected difference between the IP of a secondary and a prompt decay is related, and typically smaller, to the difference between the $c\tau$ of a b-hadron and a c-hadron, that is $\sim 400\,\mu\text{m}$, and therefore assumes on average a smaller value with respect to the resolution on the decay vertex position. It is useful to look at the resolution on the D^* decay vertex position, too. This is the variable that mostly affects the χ^2_{VVD} (D^*), since the PV position is known with an higher resolution. The distributions of the D^* decay vertex position uncertainty, for the three channels, is shown in Figure 5.2. From these plots emerges that the position of the D^* decay vertex is known with a precision even worse than the one of the D^0 decay vertex. The mean values of the uncertainty on the D^* decay vertex position are equal to 19 mm, 25 mm and 60 mm, respectively for the LL, LD and DD channel. These values have to be compared with the average flight distance of a b-hadron in LHCb, that approximately is $\gamma\beta c\tau \sim 13 \times 400\,\mu\text{m} \simeq 5.3$ mm, assuming for these particles an average momentum equal to the D^0 one. These plots show that LHCb ability to distinguish between particles coming from the PV or a displaced vertex is strongly impaired in the presence of Downstream K^0_S.
It is simple to understand that, in these conditions, the application of a cut aimed to the rejection of secondary decays removes from the sample a significant fraction of prompt events, too, causing the observed statistics loss. This is a serious problem for the $D^0 \to K^0_\text{S} K^0_\text{S}$ analysis, since it is mostly limited by the available statistics, and this approach reduces again the available events. While other off-line selection cuts have more moderate

the PV and the D^0 momentum, hence on the IP.

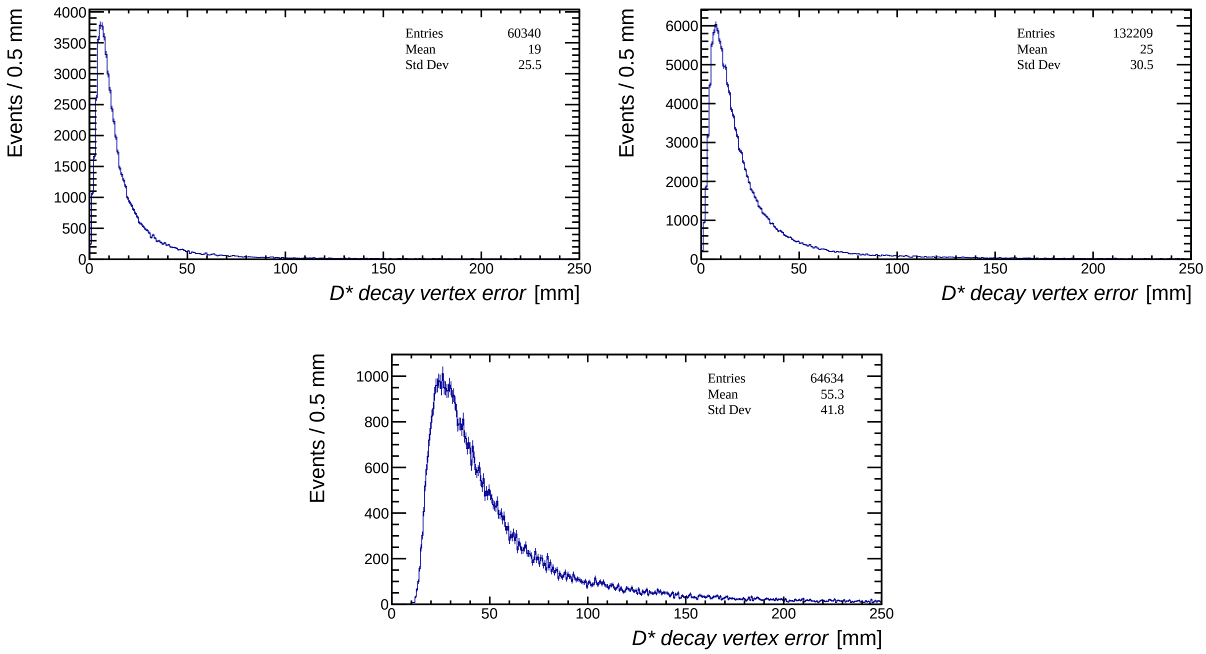

Figure 5.2: LL channel (top left), LD channel (top right), DD channel (bottom) uncertainty on the D^* decay vertex position distribution, for LL channel.

effects and are probably unavoidable, it is worthwhile to ask whether it might be possible to do without the secondary removal cuts. Much of what follows is devoted to the study of this issue.

5.1 A new approach: including secondary decays

These limits are set by the LHCb configuration, not directly designed to reveal K^0_S. Therefore, to achieve a better resolution a new approach has to be thought, that allows to handle secondary decays.
Therefore I set up an innovative way to analyze $D^0 \to K^0_S K^0_S$ decay events, where secondary decays are not considered as background, but signal events. With this approach no cut to reject them is applied. For this reason it is not present signal event loss, even if the resolution does not allow to distinguish between the two event categories.
The difficulty associated with keeping secondary decays in the samples may seem a problem, but it must be considered that even in the standard analysis, some fraction of these survives the cuts anyway, and the uncertainty on its amount introduced a non-negligible systematics in the final result. In fact, since secondary decays can not be completely distinguished from prompt events, the cuts applied do not reject all events coming from b-hadrons. This circumstance requires the introduction of a systematic uncertainty, because of the different $\mathcal{A}^{prod}$ value assumed in the two samples, influenced by a different fraction of secondary decays. The systematic uncertainty is usually computed esteeming the fraction of secondary decays present in the sample, multiplied by the difference between the $\mathcal{A}^{prod}$ for prompt and secondary decays. In the most recent analysis performed at LHCb this worthed 2×10^{-4}. This was not what limited the precision in analyzes performed so far, but with the perspective of a increased statistics, this can become a

serious problem.
By including secondary decays explicitly in the sample, we may instead be able to account more accurately for their presence than in the old approach, avoiding the insurgence of systematic effects. This is possible whether signal and control sample share the same fraction of secondary decays. In this case in the difference between the two $\mathcal{A}^{raw}$ the contributions from production asymmetries cancel completely.
Therefore the analysis I want to design have to include secondary decays in the sample, but maintaining the same fraction of these in signal and control sample.
This however is more difficult than it may appear at first glance, because most of the candidate channels to use as control channel are collected by triggers that include cuts on impact parameters of tracks whose effect on the fraction of secondaries is extremely difficult to reproduce with some precision in the $K^0_S K^0_S$ channel, due to its peculiar tracking configuration. It is certainly not possible with the two samples that have been previously used as control for the $K^0_S K^0_S$.
The simplest way to perform an analysis with this purpose is to do not apply any cut on variables that can bias the fraction of secondary decays present in the sample. This is possible through the application to signal and control channel of the same selection, aimed to reject background.

5.1.1 Control channel

If the analysis I want to perform does not have to apply any bias on the fraction of secondary events, it is necessary to have access to a control channel collected with a trigger algorithm that does not apply any cut on variables that can influence the fraction of secondary decays that can not be exactly mirrored on the $K^0_S K^0_S$ mode. This means essentially that only cuts on global D^0 and D^* variables, that are not related with precision parameters like IP are allowed. A sample that can satisfy these requirements was indeed collected during Run-2, it is the so-called $D^0 \to K^+K^-$ lifetime-unbiased sample. It will be better explained later.

5.2 Variables analysis

In the following sections I will consider a number of vertex-independent observables, to understand which allows to distinguish between signal and background event and to improve signal to background ratio. We must also be careful in avoiding making cuts on observables, whose effect can not be reproduced on our control sample. This may happen for instance when resolution is very different for that variable in the two samples. The risk we want to avoid is to affect some kinematic distribution, that in turn may be correlated with D^* vertex, leading to unwanted indirect biases on such vertex. At the end of the whole selection process, we will perform a check of consistency of the kinematical distributions of the signal with the control sample, to look for possible surviving differences, and corrections if necessary. Each variable is particularly helpful in reducing one type of background and I will present each variable considering the source of background that allows to reject. At the end cuts will be applied on some of them. The value of the cut will be chosen with an automated procedure that scans all the possible cuts combinations and fits the Δm distribution to extrapolate the achieved resolution on the number of signal events. This allows to determine the combination of rectangular cuts providing the best resolution on our parameter of interest, that is $\mathcal{A}^{CP}$.

5.2.1 Peaking background reduction

The first considered variable is the χ^2_{FD} of the K^0_{S} candidates. It is the significance on the flight distance of the K^0_{S} candidates present in the event. Only for a real K^0_{S} it assumes a value significantly different from zero, if the resolution on the origin and decay vertex of the K^0_{S} is small enough. In this situation it allows to distinguish between $D^0 \to K^0_{\text{S}} K^0_{\text{S}}$ events and $D^0 \to K^0_{\text{S}} \pi\pi$ or $D^0 \to \pi\pi\pi\pi$, where the pion pairs identified as K^0_{S} have a null FD. This cut on this variable has the same purpose of the one on z_{FD}. Now that I am not anymore concerned with comparing with previous data sample, for the definitive selection it is preferred to use χ^2_{FD} (in particular its logarithm) because it exploits the full information on K^0_{S} candidates FD and not only its projection on one direction. It must notices that , while this cut does in principle involve the position of the PV, the size of the K^0_{S} lifetime is so much larger than the lifetime of b-hadron, that the potential bias on the D^* vertex position is absolutely negligible. Regarding comparing with the control sample, this cut simply has no parallel in that sample, being purely "internal" to the decay tree. The plot that allows to understand the cut that has to be applied is the two χ^2_{FD} (K^0_{S}) scatter plot, it is shown in Figure 5.3 and 5.4 for the two channels. For the LL channel it is possible to distinguish four different regions where events cluster. In the bottom left both K^0_{S} candidates have FD compatible with zero. These events are given by $D^0 \to \pi\pi\pi\pi$ decay and combinatorial background. In the bottom right and up left regions are present events where only one of the two K^0_{S} candidates has FD compatible with zero. These events are $D^0 \to K^0_{\text{S}} \pi\pi$ events. In the up right region are present events where both K^0_{S} candidates flight for a distance significantly different from zero. This is the signal region, hence where both K^0_{S} are real. This is the region selected by applied cuts.
For LD channel it is possible to distinguish a cluster of events for which the χ^2_{FD} assumes a value different from zero. The event distribution along the two axis is different, in particular for a Downstream reconstructed K^0_{S} χ^2_{FD} naturally takes larger values. This happens because in these cases K^0_{S} traveled for at least 400 mm, having decayed after the VELO. Because of this condition the contribution of peaking background is automatically suppressed when the K^0_{S} is reconstructed Downstream, while it is necessary to apply a cut on the χ^2_{FD} of the one reconstructed Long.
The applied cuts to reject prompt peaking background are:

- $(\log\chi^2_{\text{FD}}\ (K^0_{S,1}) - 10)^2 + (\log\chi^2_{\text{FD}}\ (K^0_{S,2}) - 10)^2 < 16$ for LL channel;
- $\log\chi^2_{\text{FD}}\ (K^0_{S,L}) > 2.5$ for LD channel.

5.2.2 Rejection of combinatorial K^0_{S}

The main background of this analysis is the combinatorial component. As already said it is given by randomly matched particles that form a fake mother particle candidate. It is important to notice that this component is composed by fake K^0_{S}, D^0 and D^* candidates, that have to be separately analyzed and rejected.
I started working on the combinatorial component from the end of the decay chain, rejecting fake K^0_{S}, due to the random matching of pion pairs present in the event.

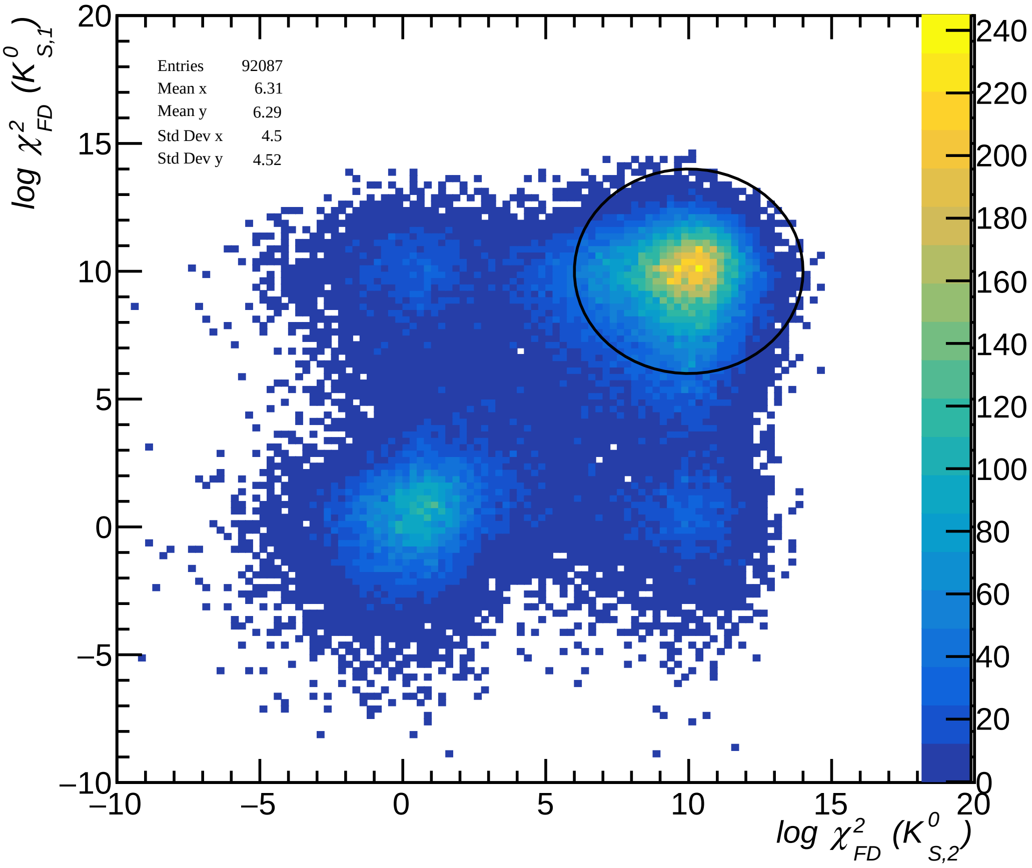

Figure 5.3: Scatter plot of logarithm χ^2_{FD} of K^0_{S} candidates in the event. K^0_{S} are labeled as 1 and 2 only to distinguish first and second candidate. Applied here are fiducial, L0, K^0_{S} and D^0 mass cuts. The applied cut on log χ^2_{FD} is represented by the black line.

To distinguish between real and fake K^0_{S} a set of variables can be used, which distribution is different for signal and background component. To produce this distribution the K^0_{S} candidates mass distribution is exploited. Here it is partially possible to identify real candidates selecting the ones with a mass near the one of a real K^0_{S}. This does not work completely. From Figures 4.5 and 4.6 it is clear that a significant fraction of events in the selected mass window comes from combinatorial events, that randomly have a mass near the real value. Considering this, to obtain the distribution of only real K^0_{S} candidates it is necessary to perform a sideband subtraction.
The procedure I followed to perform sideband subtraction consists in:

- production of distribution adopted to distinguish between signal and background component;
- identification of signal and sideband regions;
- fitting of background component in the sideband region, to extrapolate the contribution in the signal one;
- production of distributions for analyzed events, separately for the two regions;

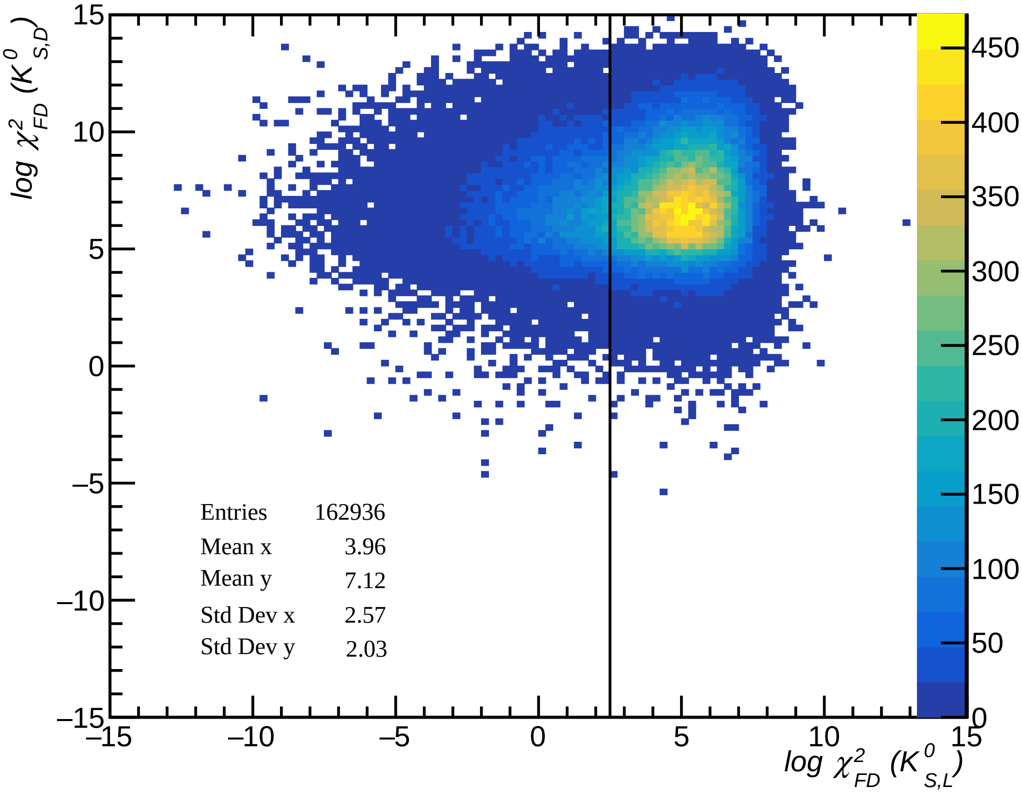

Figure 5.4: Scatter plot of logarithm χ^2_{FD} of K^0_{S} candidates in the event. Logarithm of χ^2_{FD} of Long reconstructed K^0_{S} on x-axis and Downstream reconstructed on y-axis. Applied here are fiducial, L0, K^0_{S} and D^0 mass cuts. The applied cut on log χ^2_{FD} is represented by the black line.

- production of a background distribution with rescaled in order to have the number of events equal to the one extrapolated in the signal region with the fit;
- the rescaled background distribution is subtracted to the one of the signal region, producing the distribution for signal events only;
- both signal and background distributions are normalized to their integral to compare them coherently.

This procedure is applied here to reject fake K^0_{S} and it will be applied in the following part of the analysis in the same way to reject other combinatorial background, adopting different distributions where to identify signal and background regions.

To reject fake K^0_{S} I started producing the K^0_{S} candidates mass distributions, separately for Long and Downstream reconstructed K^0_{S}, in LL and LD channel. Here I identified signal and background regions as the ones adopted in the preliminary analysis shown in the previous chapter. I fitted the background component in the K^0_{S} candidates mass distribution outside the signal region with a polynomial function of grade one and two, respectively for LL and LD channel distributions.

The K_S^0 candidates mass distributions for LL and LD channels are shown in Figure 5.5 and 5.6, where the performed fits are plotted.

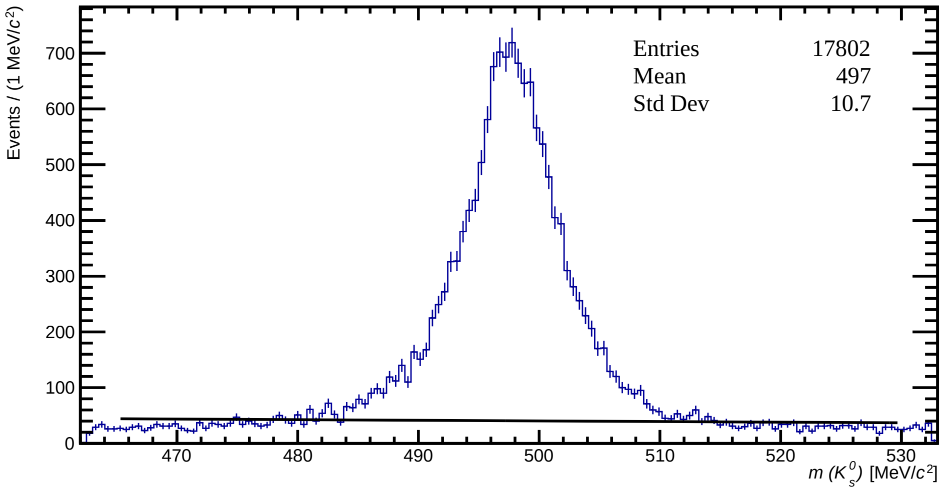

Figure 5.5: K_S^0 candidates mass distribution for LL channel. The fit to extract the background component in the signal region is shown. To produce this distribution the applied set of cuts is: fiducial cuts, L0 cuts, χ^2_{FD} (K_S^0) cuts, $|\Delta m - 145.4\,\mathrm{MeV}/c^2| < 1.5$, $\mathrm{MeV}/c^2 |m(D^0) - 1864.4\,\mathrm{MeV}/c^2| < 20\,\mathrm{MeV}/c^2$.

As can be seen the functions do not describe exactly the background contribution. This was expected, since the choice of those function shapes has not physical motivation. The obtained description of the background is however fully adequate for the purposes of this step of the analysis, where I want to obtain only an estimate of the background component in the signal region.

The first variable I analyzed to distinguish between real and fake K_S^0 is χ^2_{vtx}. For a fake K_S^0 χ^2_{vtx} is expected to assume a larger values on average. This because for the background contribution two pion tracks do not come in reality from a common vertex, as, on the contrary, happens for the decay of real K_S^0. This variable has been analyzed for both LL and LD channel. For LD channel it was useful to distinguish between TIS and TOS tagged events.
χ^2_{vtx} (K_S^0) distributions for LL and LD channels are shown in Figure 5.7 and 5.8. It is possible to distinguish a different behavior for Long and Downstream reconstructed K_S^0 and for TOS and TIS tagged events. The distributions for signal and background behaves as expected, seeing that background contribution has a longer tail with respect to the one of the signal. This can be exploited to increase the signal to background ratio and a cut on χ^2_{vtx} will be applied.
Another considered variable is the transverse momentum of the K_S^0. p_{T} (K_S^0) distributions for LL and LD channels are shown in Figure 5.9 and 5.10. Here the distinction between Long and Downstream reconstructed K_S^0 and between TOS and TIS tagged events is more evident than before, due mostly to the different trigger cuts that influences the distributions. The difference between p_{T} distributions for signal and background events is clear. Signal contribution has larger p_{T} on average, since those K_S^0s come from the decay of a

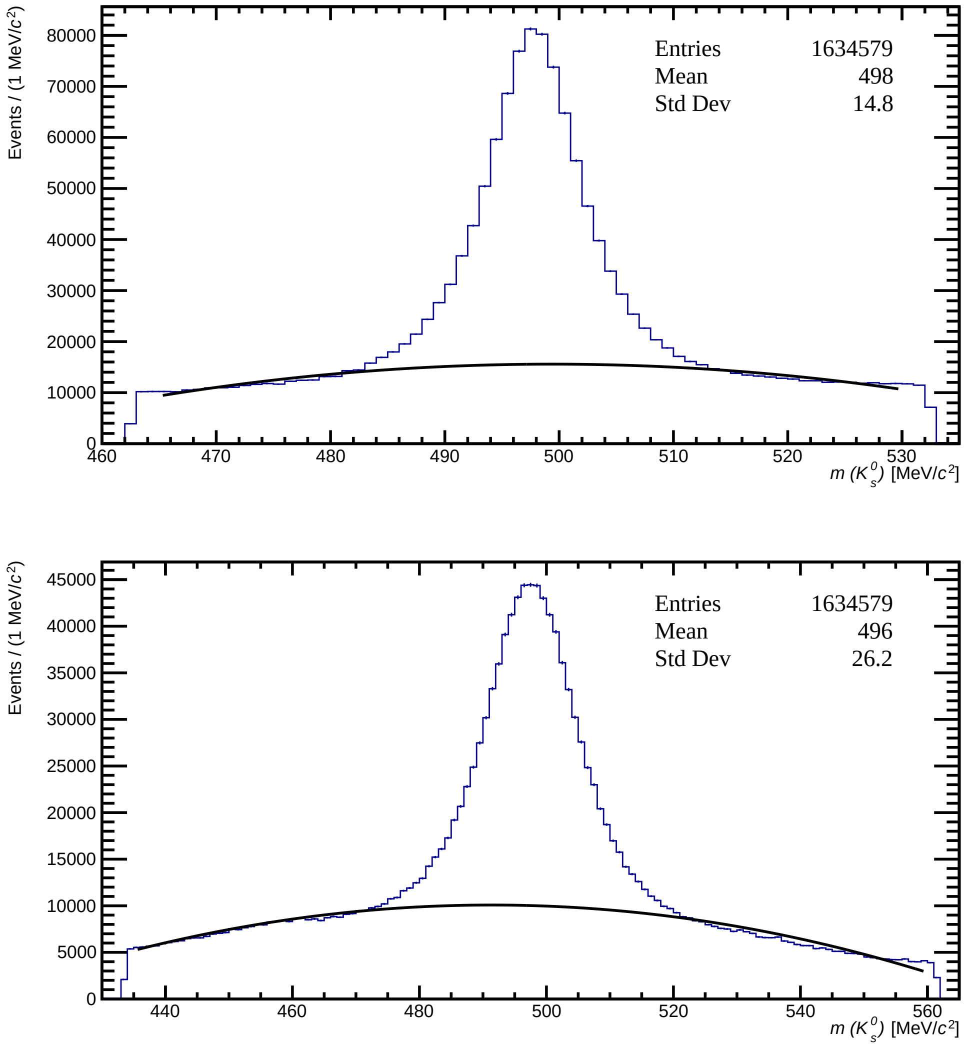

Figure 5.6: K^0_{S} candidates mass distributions for LD channel. Long reconstructed K^0_{S} on the left and Downstream reconstructed on the right. The fit to extract the background component in the signal region is shown. To produce these distributions the applied set of cuts is: fiducial cuts, L0 cuts, χ^2_{FD} (K^0_{S}) cuts, $|\Delta m - 145.4\,\mathrm{MeV}/c^2| < 1.5,\ \mathrm{MeV}/c^2|m(D^0) - 1864.4\,\mathrm{MeV}/c^2| < 20\,\mathrm{MeV}/c^2$.

D^0. Only on the p_{T} of the Downstream reconstructed K^0_{S} a cut will be applied. In the other cases the application of any cut could be counterproductive. This because, for Long TOS events, the difference is less evident and a cut can not be so efficient, while for Long TIS events even a loose cut on p_{T} can exclude a significant fraction of signal events. This is done considering that also other cuts have to be applied and reducing too much signal contribution with a single cut, to maximize there the signal to background ratio, is not efficient.

To reject fake K^0_{S} candidates are obviously applied mass cuts, too. As previously shown a mass cut is extremely powerful rejecting a large fraction of combinatorial background. The applied mass cuts are the same as before.

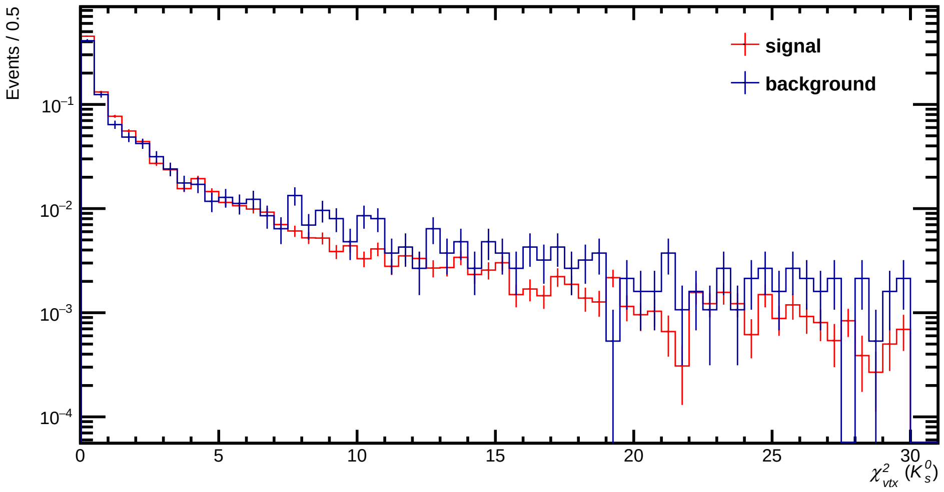

Figure 5.7: χ^2_{vtx} (K^0_{S}) distributions for signal and background contributions, for LL channel. To produce this distribution the applied set of cuts is: fiducial cuts, L0 cuts, χ^2_{FD} (K^0_{S}) cuts, $|\Delta m - 145.4\,\text{MeV}/c^2| < 1.5\,\text{MeV}/c^2$, $|m(D^0) - 1864.4\,\text{MeV}/c^2| < 20\,\text{MeV}/c^2$.

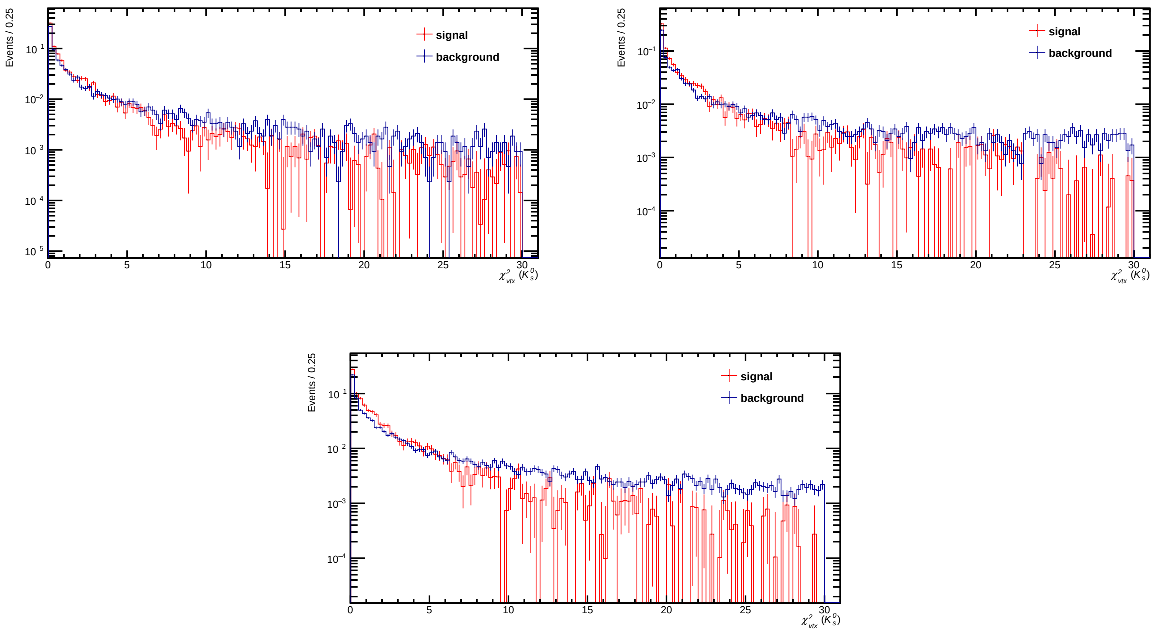

Figure 5.8: χ^2_{vtx} (K^0_{S}) distributions for signal and background contributions, for LD channel. On the top left are shown Long reconstructed and TOS tagged K^0_{S}, on the top right are shown Long reconstructed and TIS tagged K^0_{S}, on the bottom are shown Downstream reconstructed K^0_{S}. To produce this distribution the applied set of cuts is: fiducial cuts, L0 cuts, χ^2_{FD} (K^0_{S}) cuts, $|\Delta m - 145.4\,\text{MeV}/c^2| < 1.5\,\text{MeV}/c^2$, $|m(D^0) - 1864.4\,\text{MeV}/c^2| < 20\,\text{MeV}/c^2$.

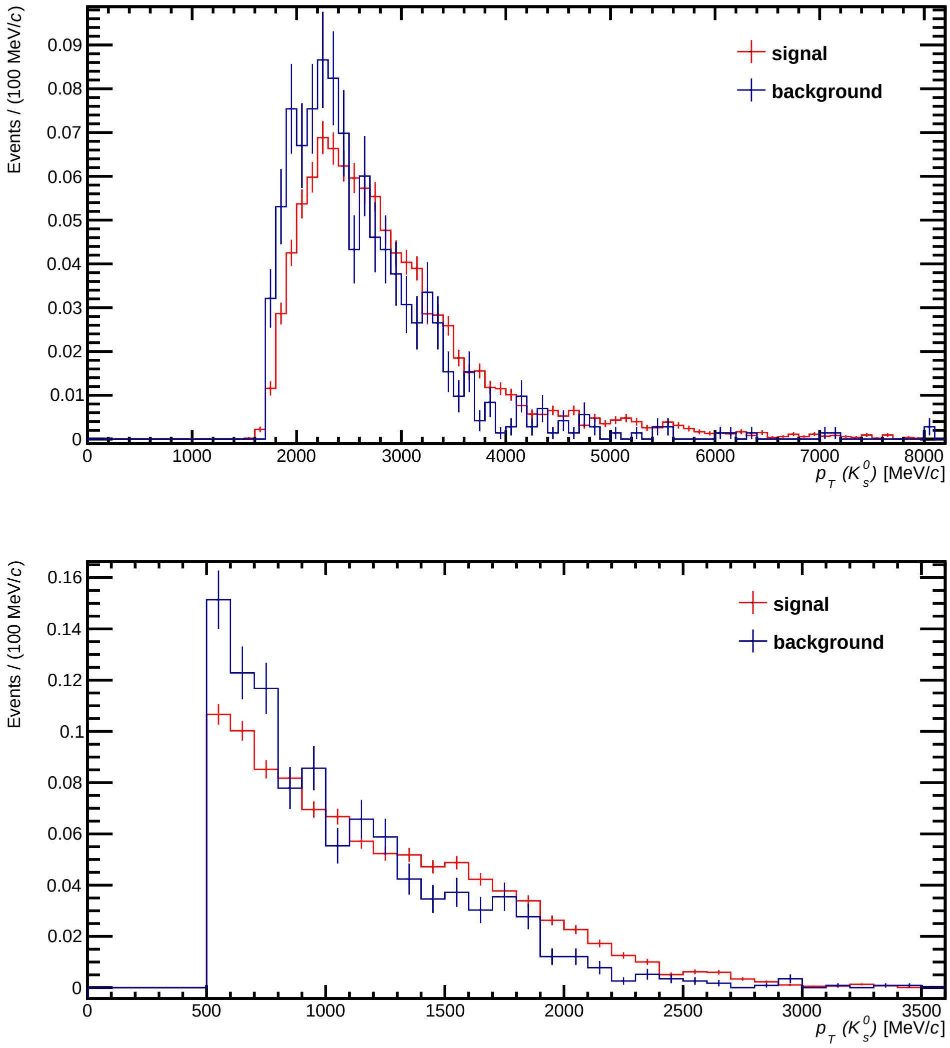

Figure 5.9: p_{T} (K^0_{S}) distributions for signal and background contributions, for LL channel. TOS events are shown on the left, TIS on the right. To produce this distribution the applied set of cuts is: fiducial cuts, L0 cuts, χ^2_{FD} (K^0_{S}) cuts, $|\Delta m - 145.4\,\mathrm{MeV}/c^2| < 1.5\,\mathrm{MeV}/c^2$, $|m(D^0) - 1864.4\,\mathrm{MeV}/c^2| < 20\,\mathrm{MeV}/c^2$.

5.2.3 Rejection of combinatorial D^0

The variables analyzed here aim to reject fake D^0, given by the random combination of K^0_{S} present in the event. The signal region it is identified as the one around the peak in the D^0 candidates mass distribution: $|m(D^0) - 1864.4\,\mathrm{MeV}/c^2| < 20\,\mathrm{MeV}/c^2$. The background region is the one outside the peak. Also here to extrapolate background contribution under signal peak I fitted mass distribution in the background region. In particular I adopted a first degree polynomial function.
The D^0 mass distributions for the two channels are shown in Figure 5.11 and 5.12. It is possible to see a clear difference between the signal evidence in the two samples. The signal to background ratio in the LL channel is clearly higher than in the LD channel. In the first case I decided to apply only a mass cut to reject combinatorial fake D^0. In the case of LD channel it is not enough and I analyzed other variables.

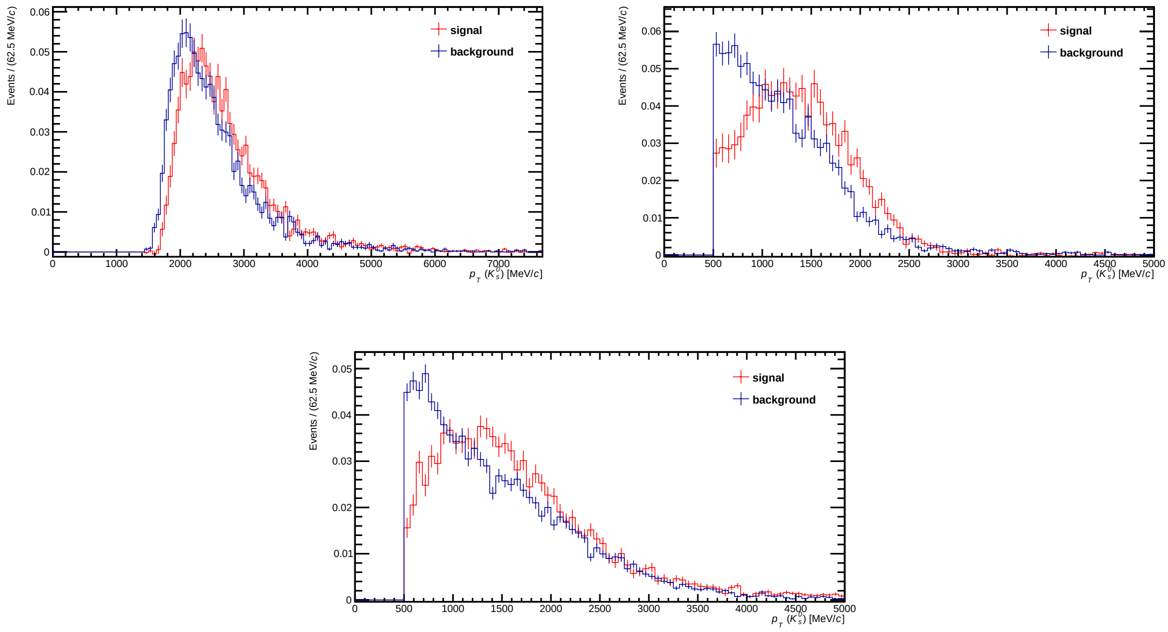

Figure 5.10: p_{T} (K_{S}^0) distributions for signal and background contributions, for LD channel. On the top left are shown Long reconstructed and TOS tagged K_{S}^0, on the top right are shown Long reconstructed and TIS tagged K_{S}^0, on the bottom are shown Downstream reconstructed K_{S}^0. To produce this distribution the applied set of cuts is: fiducial cuts, L0 cuts, χ^2_{FD} (K_{S}^0) cuts, $|\Delta m - 145.4\,\mathrm{MeV}/c^2| < 1.5\,\mathrm{MeV}/c^2$, $|m(D^0) - 1864.4\,\mathrm{MeV}/c^2| < 20\,\mathrm{MeV}/c^2$.

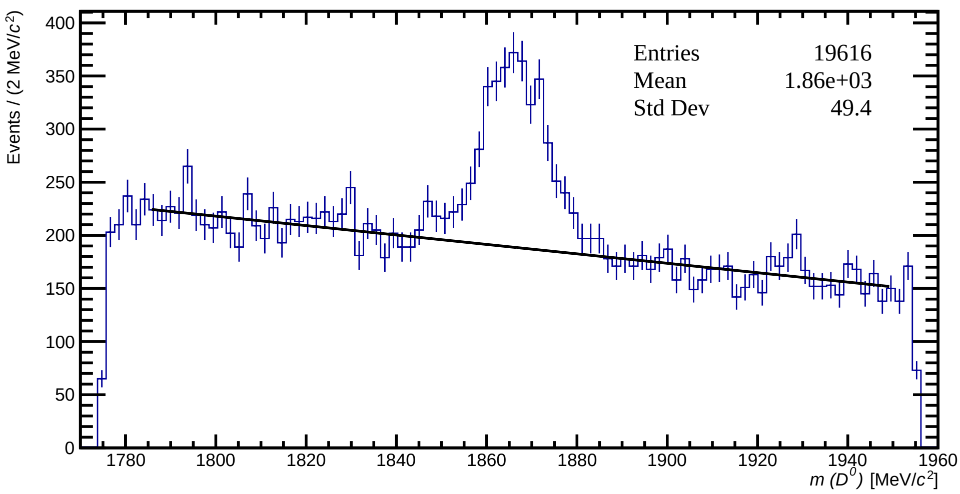

Figure 5.11: D^0 candidates mass distribution for LL channel. The fit to extract the background component in the signal region is shown. To produce this distribution the applied set of cuts is: fiducial cuts, L0 cuts, χ^2_{FD} (K_{S}^0) cuts, $|\Delta m - 145.4\,\mathrm{MeV}/c^2| < 1.5\,\mathrm{MeV}/c^2$, $|m(K_{\mathrm{S}}^0) - 497.6\,\mathrm{MeV}/c^2| < 10.5\,\mathrm{MeV}/c^2$.

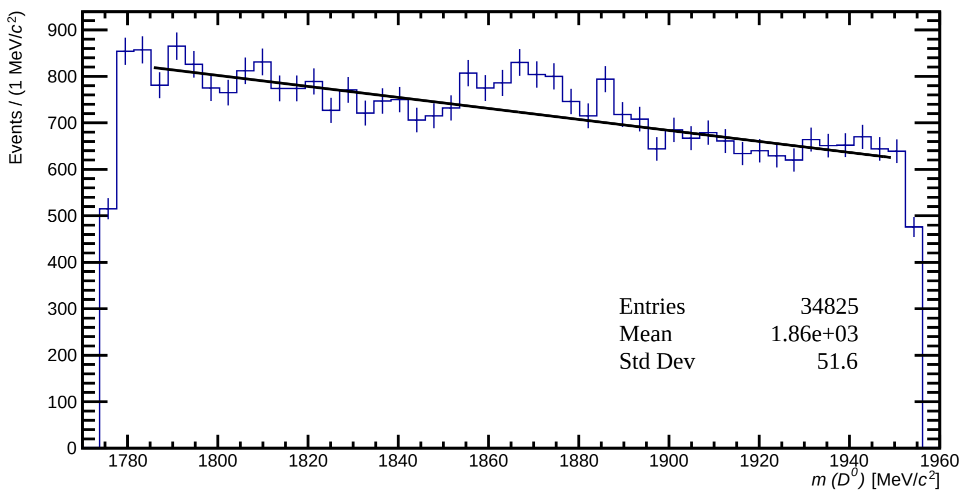

Figure 5.12: D^0 candidates mass distributions for LD channel. The fit to extract the background component in the signal region is shown. To produce this distribution the applied set of cuts is: fiducial cuts, L0 cuts, χ^2_{FD} (K^0_{S}) cuts, $|\Delta m - 145.4\,\mathrm{MeV}/c^2| < 1.5\,\mathrm{MeV}/c^2 |m(K^0_{\mathrm{S}}) - 497.6\,\mathrm{MeV}/c^2| < 10.5\,\mathrm{MeV}/c^2$ for Long reconstructed K^0_{S}, $|m(K^0_{\mathrm{S}}) - 497.6\,\mathrm{MeV}/c^2| < 15\,\mathrm{MeV}/c^2$ for Downstream reconstructed K^0_{S}.

The first variable I decided to analyze is the D^0 transverse momentum.
D^0 transverse momentum distribution for LD channel is shown in Figure 5.13. As was

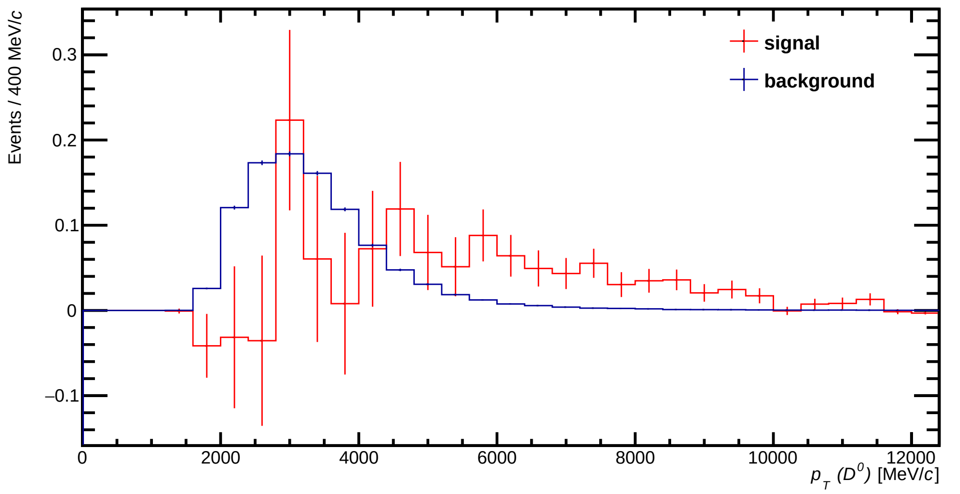

Figure 5.13: p_{T} (D^0) distribution for signal and background contributions, for LD channel. To produce this distribution the applied set of cuts is: fiducial cuts, L0 cuts, χ^2_{FD} (K^0_{S}) cuts, $|\Delta m - 145.4\,\mathrm{MeV}/c^2| < 1.5\,\mathrm{MeV}/c^2$, $|m(K^0_{\mathrm{S}}) - 497.6\,\mathrm{MeV}/c^2| < 10.5\,\mathrm{MeV}/c^2$ for Long reconstructed K^0_{S}, $|m(K^0_{\mathrm{S}}) - 497.6\,\mathrm{MeV}/c^2| < 15\,\mathrm{MeV}/c^2$ for Downstream reconstructed K^0_{S}.

expected from plot shown in Figure 5.12 the signal contribution is poor, and this leads to a low statistics histogram for the signal contribution, as shown in the previous Figure. In this situation is still possible to distinguish two different trends for the two contributions. This motivates the inclusion in the optimization procedure of the p_{T} (D^0).

5.2.4 Rejection combinatorial D^*

Another analyzed variable is the π_{tag} transverse momentum, that helps in rejecting fake D^*. The D^* transverse momentum it is not considered because it is highly correlated to D^0 and π_{tag} transverse momentum. To identify a signal and background region here the Δm distribution is considered. The signal region it is identified as $|\Delta m - 145.4\,\mathrm{MeV}/c^2| < 1.5\,\mathrm{MeV}/c^2$ and the background region is the complementary one. The fit is performed only on the background region, to fit background component. During this procedure I found useful to adopt a different background parametrization, since it converges for a larger range of initial parameters with respect to the one adopted in the preliminary analysis; for the same reason I decided to adopt this for the rest of the analysis from this point. The adopted *p.d.f.* is:

$$f_{bkg}(x) \propto \sqrt{x - m_\pi}(1 + a \cdot (x - m_\pi) + b \cdot (x - m_\pi)^2) \tag{5.1}$$

Δm distributions and the performed fit on these are shown in Figure 5.14 and 5.15.

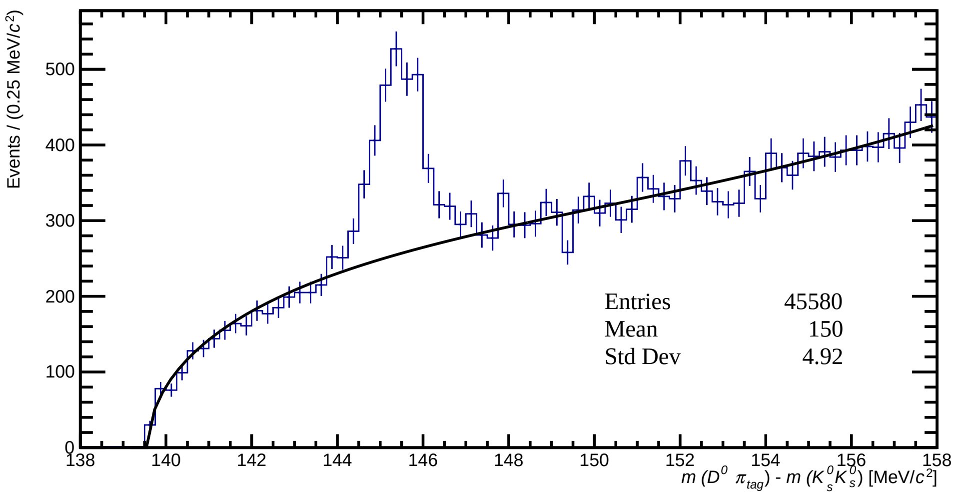

Figure 5.14: Δm distribution for LL channel. The fit to extract the background component in the signal region is shown. To produce this distribution the applied set of cuts is: fiducial cuts, L0 cuts, χ^2_{FD} (K^0_{S}) cuts, $|m(K^0_{\mathrm{S}}) - 497.6\,\mathrm{MeV}/c^2| < 10.5\,\mathrm{MeV}/c^2$, $|m(D^0) - 1864.4\,\mathrm{MeV}/c^2| < 20\,\mathrm{MeV}/c^2$.

p_{T} (π_{tag}) distributions for LL and LD channel extracted using previous fits are shown in Figure 5.16 and 5.17. This variable can be adopted to reject combinatorial background events for LL channel, as can be seen from the different trends present in Figure 5.16. For the LD channel the low statistics does not allow to distinguish as in the previous case two different trends. For this reason this variable it is not adopted in the following part of the analysis.

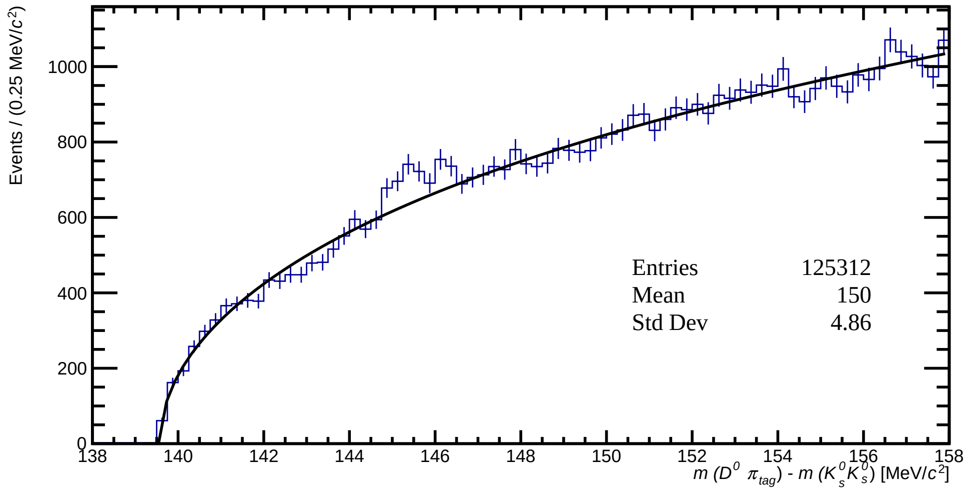

Figure 5.15: Δm distribution for LD channel. The fit to extract the background component in the signal region is shown. To produce this distribution the applied set of cuts is: fiducial cuts, L0 cuts, $\chi^2_{\rm FD}$ $(K^0_{\rm S})$ cuts, $|m(K^0_{\rm S}) - 497.6\,{\rm MeV}/c^2| < 10.5\,{\rm MeV}/c^2$ for Long reconstructed $K^0_{\rm S}$ and $|m(K^0_{\rm S}) - 497.6\,{\rm MeV}/c^2| < 15\,{\rm MeV}/c^2$ for Downstream reconstructed $K^0_{\rm S}$, $|m(D^0) - 1864.4\,{\rm MeV}/c^2| < 20\,{\rm MeV}/c^2$.

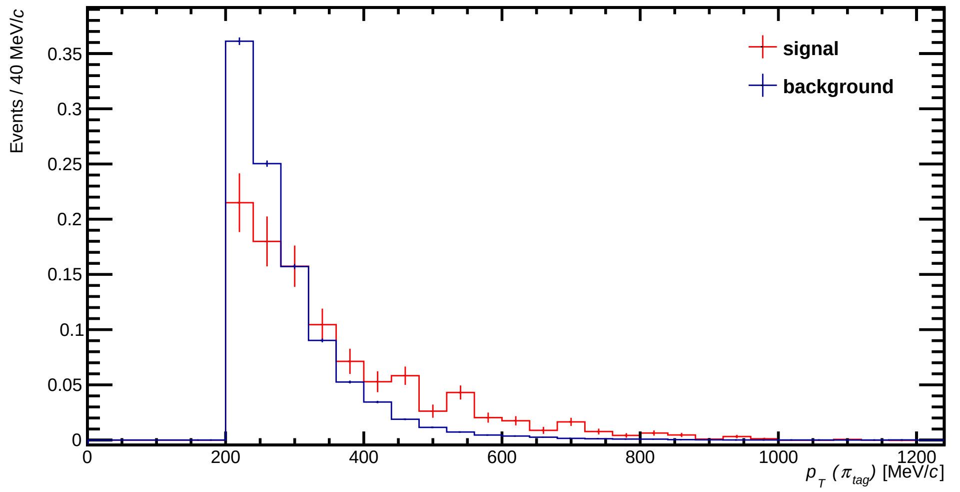

Figure 5.16: $p_{\rm T}$ (π_{tag}) distribution for LL channel. To produce this distribution the applied set of cuts is: fiducial cuts, L0 cuts, $\chi^2_{\rm FD}$ $(K^0_{\rm S})$ cuts, $|m(K^0_{\rm S}) - 497.6\,{\rm MeV}/c^2| < 10.5\,{\rm MeV}/c^2$, $|m(D^0) - 1864.4\,{\rm MeV}/c^2| < 20\,{\rm MeV}/c^2$.

5.3 Cuts optimization

As previously said, the identified variables are now scanned together to find the best cuts configuration that maximizes the statistical sensitivity that can be achieved. The sensitivity on $\mathcal{A}^{CP}$ is directly connected to the one that can be achieved on the number

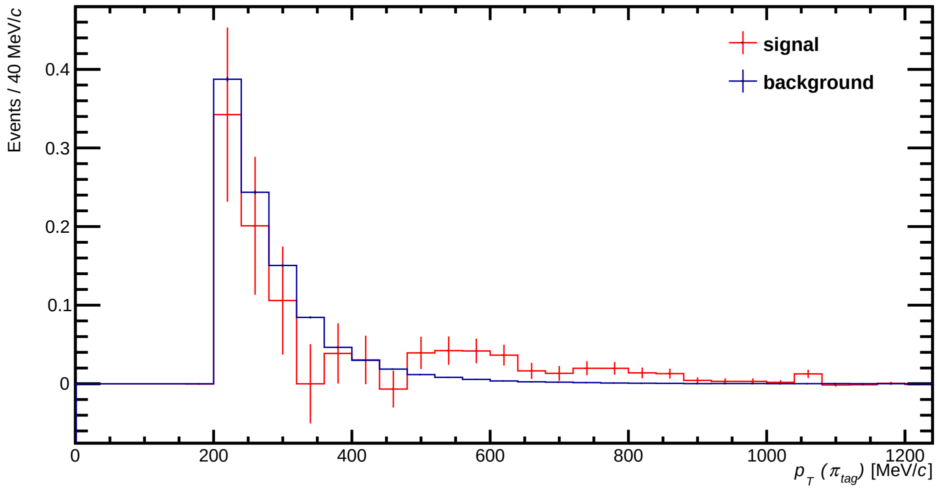

Figure 5.17: p_{T} (π_{tag}) distribution for LD channel. To produce this distribution the applied set of cuts is: fiducial cuts, L0 cuts, χ^2_{FD} (K^0_{S}) cuts, $|m(K^0_{\mathrm{S}}) - 497.6\,\mathrm{MeV}/c^2| < 10.5\,\mathrm{MeV}/c^2$ for Long reconstructed K^0_{S} and $|m(K^0_{\mathrm{S}}) - 497.6\,\mathrm{MeV}/c^2| < 15\,\mathrm{MeV}/c^2$ for Downstream reconstructed K^0_{S}, $|m(D^0) - 1864.4\,\mathrm{MeV}/c^2| < 20\,\mathrm{MeV}/c^2$.

of signal events N_S, as can be simply seen in the case of null $\mathcal{A}^{CP}$:

$$\begin{aligned}
\sigma(\mathcal{A}^{CP})_{\mathcal{A}^{CP}=0} &= \sqrt{\left(\frac{\partial\mathcal{A}^{CP}}{\partial N_+}\right)^2 \sigma^2(N_+) + \left(\frac{\partial\mathcal{A}^{CP}}{\partial N_-}\right)^2 \sigma^2(N_-)} = \\
&= \sqrt{\frac{4N_+^2}{N_S^4}\sigma^2(N_+) + \frac{4N_-^2}{N_S^4}\sigma^2(N_-)} = \\
&= \sqrt{\frac{\sigma^2(N_S)}{N_S^2}} = \frac{\sigma(N_S)}{N_S}
\end{aligned}$$

So the optimization procedure it is performed as follows:

- For each variable a values range where the cut will be located it is identified, suggested from signal and background distributions previously shown;
- In each the selected region some steps are identified, that can be in different number for different variables;
- Every possible combination of the identified steps is applied to the sample and the relative Δm distribution is extracted;
- Each Δm distribution is fitted and the value of $\sigma(N_S)/N_S$ is extracted.

During the optimization process one or more fits could not converge to a good minimum and did not provide any significant result. This happens because the initial parameters from where every fit starts its minimization are the same and this choice can lead to bad convergence in some case. When the fit does not converge to a good minimum it is repeated changing initial parameters, until it is possible to know the value of $\sigma(N_S)/N_S$ for every cut combination. I chose this strategy as a good compromise between the control on the procedure and the time necessary for its execution. In fact, the number of fits that have to be run more than one time is small and the procedure is sufficiently fast. This happens because of the poor sample statistics, that makes the fit convergence simple enough.

In conclusion the selection that will be applied to LL channel events is:

- Fiducial cuts
- L0 trigger requirements: D0_L0HadronDecision_TOS $\vee$ DS_L0Global_TIS;
- $[\log(\chi^2_{\rm FD}\ (K^0_{\rm S\ 1})) - 10]^2 + [\log(\chi^2_{\rm FD}\ (K^0_{\rm S\ 2})) - 10]^2 < 16$;
- $|m(K^0_{\rm S1,2}) - 497.6\,{\rm MeV}/c^2| < 10.5\,{\rm MeV}/c^2$;
- $|m(D^0) - 1864.4\,{\rm MeV}/c^2| < 20\,{\rm MeV}/c^2$;
- $\chi^2_{\rm vtx}\ (K^0_{\rm S\ 1,2}) < 27.5$;
- $p_{\rm T}\ (\pi_{tag}) > 225\ \ {\rm MeV}/c$.

The selection that will be applied to LD channel events is:

- Fiducial cuts
- L0 trigger requirements: D0_L0HadronDecision_TOS $\vee$ DS_L0Global_TIS;
- $\log(\chi^2_{\rm FD}\ (K^0_{\rm S\ \mathit{Long}})) > 2.5$;
- $|m(K^0_{\rm S\mathit{Long}}) - 497.6\,{\rm MeV}/c^2| < 10.5\,{\rm MeV}/c^2$ and
  $|m(K^0_{\rm S\mathit{Downstream}}) - 497.6\,{\rm MeV}/c^2| < 15\,{\rm MeV}/c^2$;
- $|m(D^0) - 1864.4\,{\rm MeV}/c^2| < 20\,{\rm MeV}/c^2$;
- $\chi^2_{\rm vtx}\ (K^0_{\rm S\ \mathit{Long,TOS}}) < 22.5$,
  $\chi^2_{\rm vtx}\ (K^0_{\rm S\ \mathit{Long,TIS}}) < 25$,
  $\chi^2_{\rm vtx}\ (K^0_{\rm S\ \mathit{Downstream}}) < 15$;
- $p_{\rm T}\ (D^0) > 4000\ \ {\rm MeV}/c$.

These selections identify the two samples on which the analysis will be performed. I need to underline that this is only a preliminary analysis and is clear that this optimization procedure does not achieve the best conceivable resolution. It is still possible to introduce multivariate cuts as it was done in the last LHCb analysis [40], leading to a further improvement in resolution with respect to the purely rectangular selection, but it is not done here since it is not the purpose of this analysis, that aim to understand the results that can be achieved including secondary decay events in the sample.
It is interesting to analyze the Δm distributions obtained for the two channels with the application of the mentioned selections and to fit them in order to understand the statistical sensitivity that can be achieved.
The Δm distributions for LL and LD channel after the application of the identified selections are shown in Figure 5.18. To produce these plots the $K^0_{\rm S}$ mass constrain was

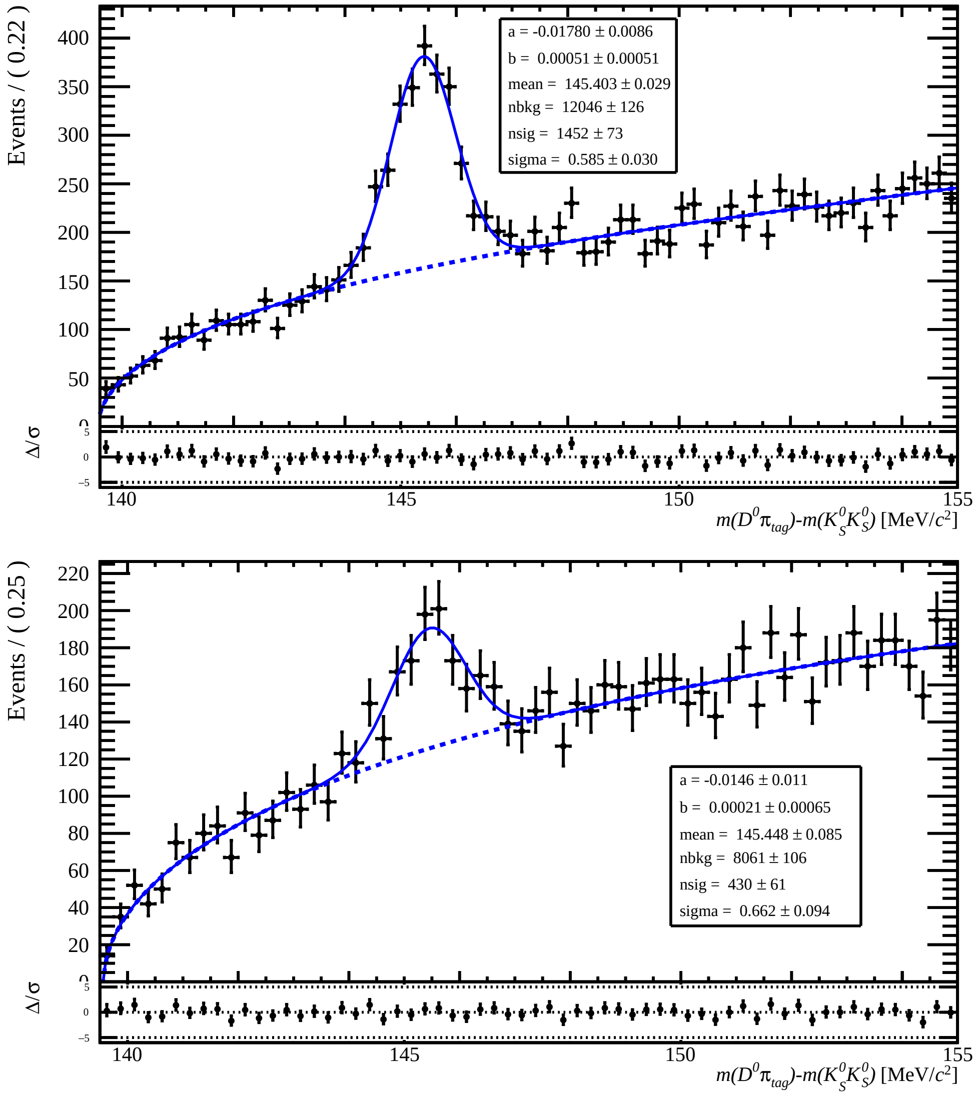

Figure 5.18: Δm distribution for LL (up) and LD (down) channels after the application of identified selections.

imposed on the decay chain. This is done after the selection it is already applied and the background component is reduced, so the application of this constrain allows to improve mass resolution and signal to background ratio without pulling fake K_S^0 events artificially in line with the expected mass. The achieved statistical sensitivities for the two channels are at this point 5% and 14.2%, respectively for LL and LD channel.
It is interesting to analyze the two channels rejecting secondary decays, with the application of the $\chi^2_{\rm IP}$ (D^0), $\chi^2_{\rm IP}$ (π_{tag}) and $\chi^2_{\rm VVD}$ (D^*) cuts, extracting the signal yields and the achieved resolution. The obtained Δm distributions and the relative fits are shown in Figure 5.19, for LL and LD channels; also here the K_S^0 mass constrain is applied. It is useful to make a comparison between the results that can be obtained rejecting or not secondary secondary decays, shown in Table 5.1. The most important thing that emerges from the comparison is the gain in statistics obtained with the new strategy. The selection here identified reaches the purpose for which it was thought, avoiding the significant decrease of signal yields due to the application of $\chi^2_{\rm IP}$ and $\chi^2_{\rm VVD}$ cuts, verified in the previous

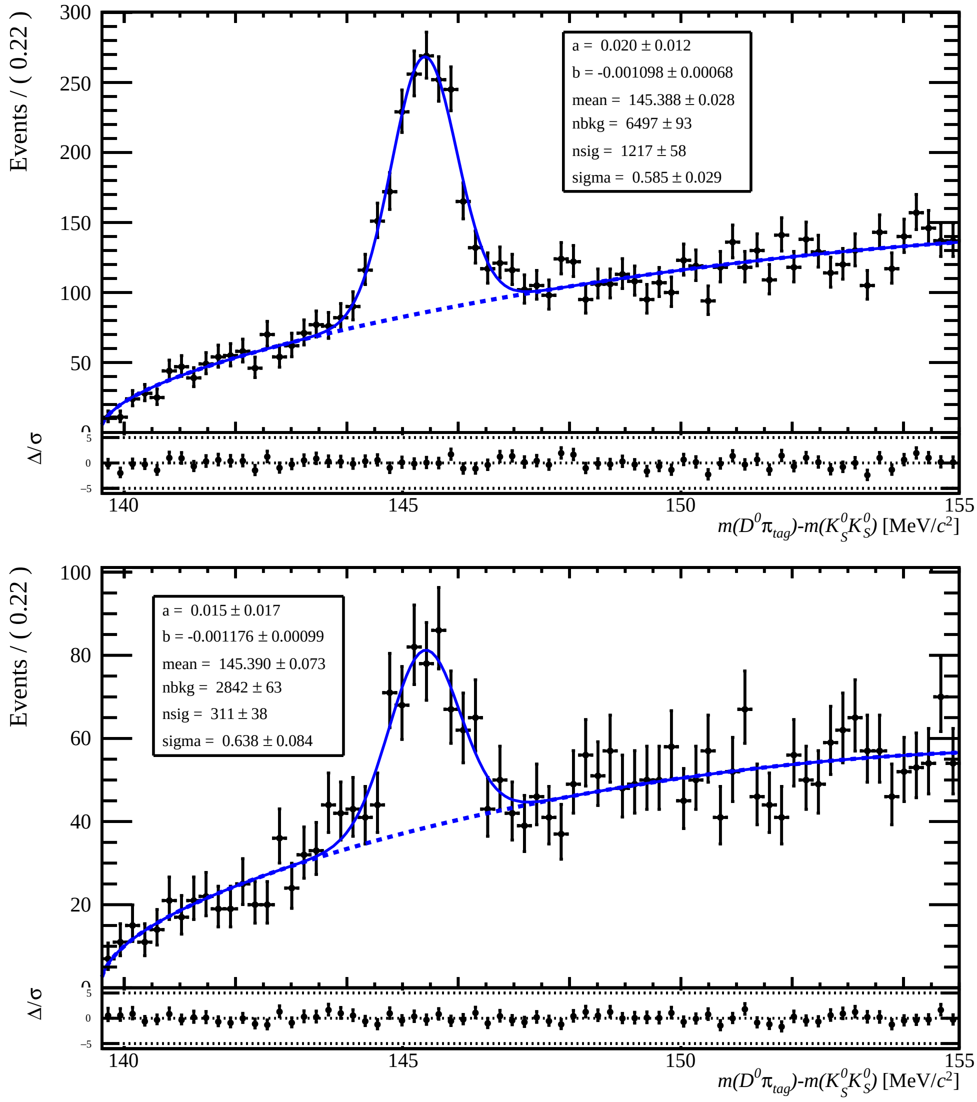

Figure 5.19: Δm distribution for LL (up) and LD (down) channels after the application of identified selections and the rejection of secondary decay events.

Sample	n_{sig}	$\sigma(n_{sig})/n_{sig}$ [%]
LL	1452 $\pm$ 73	5
LD	430 $\pm$ 61	14.2
LL *(no sec.)*	1217 $\pm$ 58	4.8
LD *(no sec.)*	311 $\pm$ 38	12.2

Table 5.1: Comparison between signal yields and statistical sensitivities achieved for LL and LD channels before and after the rejection of secondary decays. I used *no sec.* to label the samples where secondary decays are rejected

chapter and present here, too, equal to 16 % and 28 %, respectively for the LL and LD channel. It can be noticed that the decreases due to the considered cuts are smaller than the ones verified in the previous chapter. This does not changes the purposes for which the analysis has been thought and it is probably due to cuts included in the optimized selection, that rejects a fraction of signal events that will be rejected by the χ^2_{IP} and χ^2_{VVD}

cuts, too.
The other important quantity that has to be compared is the achieved statistical sensitivity. The rejection of secondary decays improves the result, rejecting also a significant fraction of background events, but leading to resolution values similar to the ones achieved with the new analysis.
These two results shows that the identified analysis approach reaches its purpose, demonstrating the possibility to perform an analysis without applying any cut on variables related to vertex position, avoiding the related signal event loss and reaching a sensitivity similar to the one achieved with the usual approach.
While this may be less exciting of what the Table 4.5 in Chapter 5, on a perspective of future, larger samples, the important advantage remains of a reduced systematics on secondary subtraction.

5.4 Application of PV constrain

Another element has to be added to considered. In the usual analysis, after the rejection of secondary decays, it is possible to exploit the DTF PV constrain. Forcing the coincidence between the D^* vertex and the PV a further resolution improvement take place. To understand the improvement size I apply PV constrain, fitting Δm distributions.
The Δm distributions obtained exploiting the PV constrain and the relative fits on LL and LD channel events, are shown in Figure 5.20. It clearly emerges that the PV constrain is a powerful tool to improve the resolution; in fact it allows to reach a statistical sensitivity equal to 3.6% and 9% for the LL and LD channel, respectively, causing an improvement of several percent. The PV constrain can not be directly applied in case of the new approach, because of the presence of secondary decays in the sample. But other strategies can be found to anyway exploit it.

5.4.1 $\Delta\chi^2$ splitting

In the sample where secondary decays are not rejected, are present events for which the D^* vertex is compatible with the PV and other where happens the opposite. The second ones are usually rejected with the application of the χ^2_{IP} and χ^2_{VVD} cuts. The two kinds of event can be distinguished considering the difference between the DTF χ^2 values (defined as $\Delta\chi^2$), without and with the application of the PV constrain. The two fits have different degrees of freedom (dof), in particular the one where the PV constrain is applied has 3 more dof than the other, therefore $\Delta\chi^2$ is distributed as a χ^2, with 3 dof. $\Delta\chi^2$ will assume larger values for events where the D^* is not compatible with the PV, because the χ^2 returned by the DTF, when the PV constrain is applied, will assume larger values, because of the D^* vertex incompatibility with the PV.
The sample can be therefore split between events where $\Delta\chi^2$ in smaller than a certain threshold, for which the PV constrain can be applied, and those where $\Delta\chi^2$ is larger than the threshold, where the constrain can not be applied. The threshold value here assumed is 8, equal to a distance of two standard deviations from the distribution mean.
This splitting allow to apply anyway the PV constrain, to improve the resolution, and to maintain the full sample statistics, avoiding the cuts necessary to reject secondary decays. In this approach it is possible to manage the fraction of secondary decays, that can be in principle different between the two subsamples. This is based on the work described in

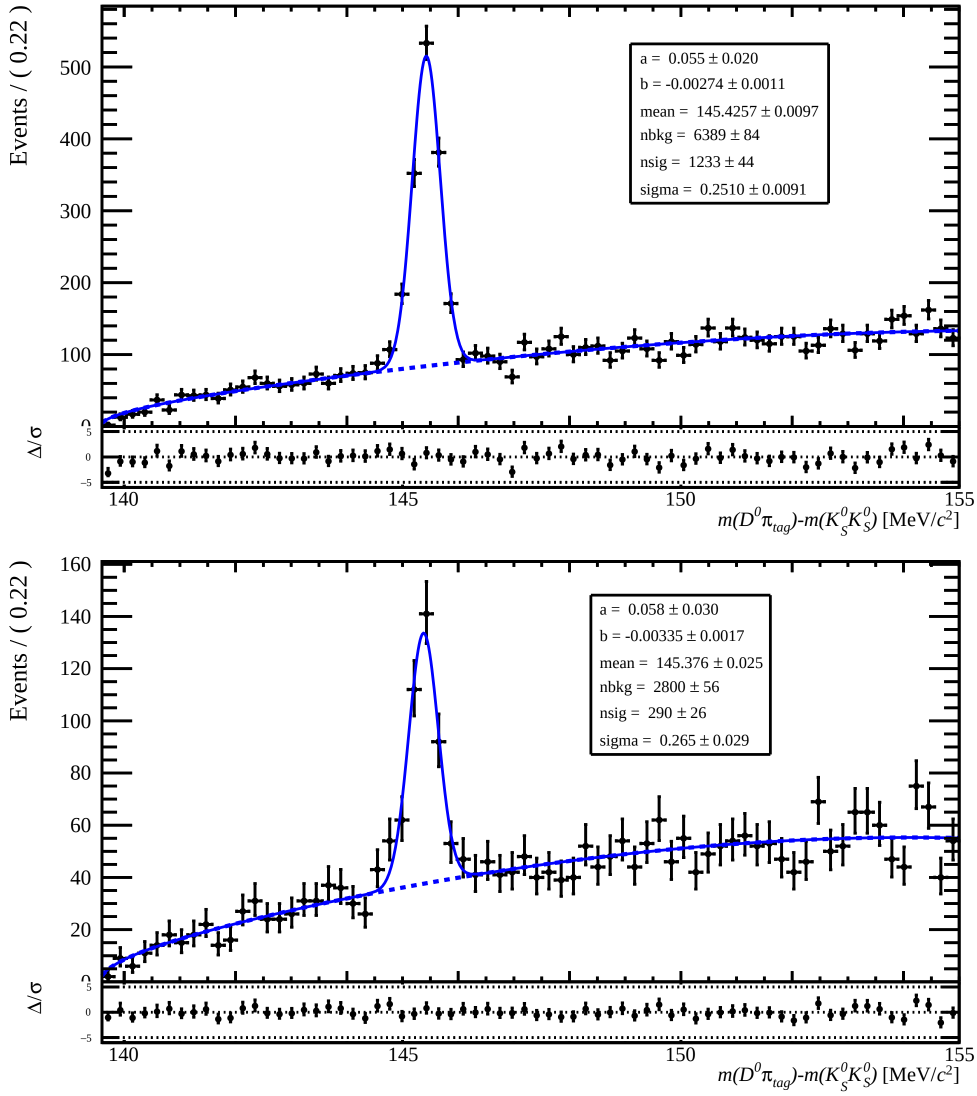

Figure 5.20: Δm distribution for LL (up) and LD (down) channels after the application of identified selections and the rejection of secondary decay events, extracted using DTF with PV constrain.

the following sections, and will be explained in 6.2.4.
This approach will not be completely pursued, since it is over the thesis aims, but it is interesting to understand the resolution that can be achieved applying it to the 2017 sample, and if it is comparable with the one achieved simply rejecting secondary decays and applying the PV constrain.

5.4.2 LL channel

Δm distributions obtained splitting the LL channel sample depending on the $\Delta\chi^2$ value and the relative fits are shown in Figure 5.21. As can be seen for the sample where the D^* is compatible with the PV, the resolution is improved by the applied PV constrain, and it is equal to 3.5%. On the sample with $\Delta\chi^2$ over threshold, the statistics is lower and the resolution is 22.2%.

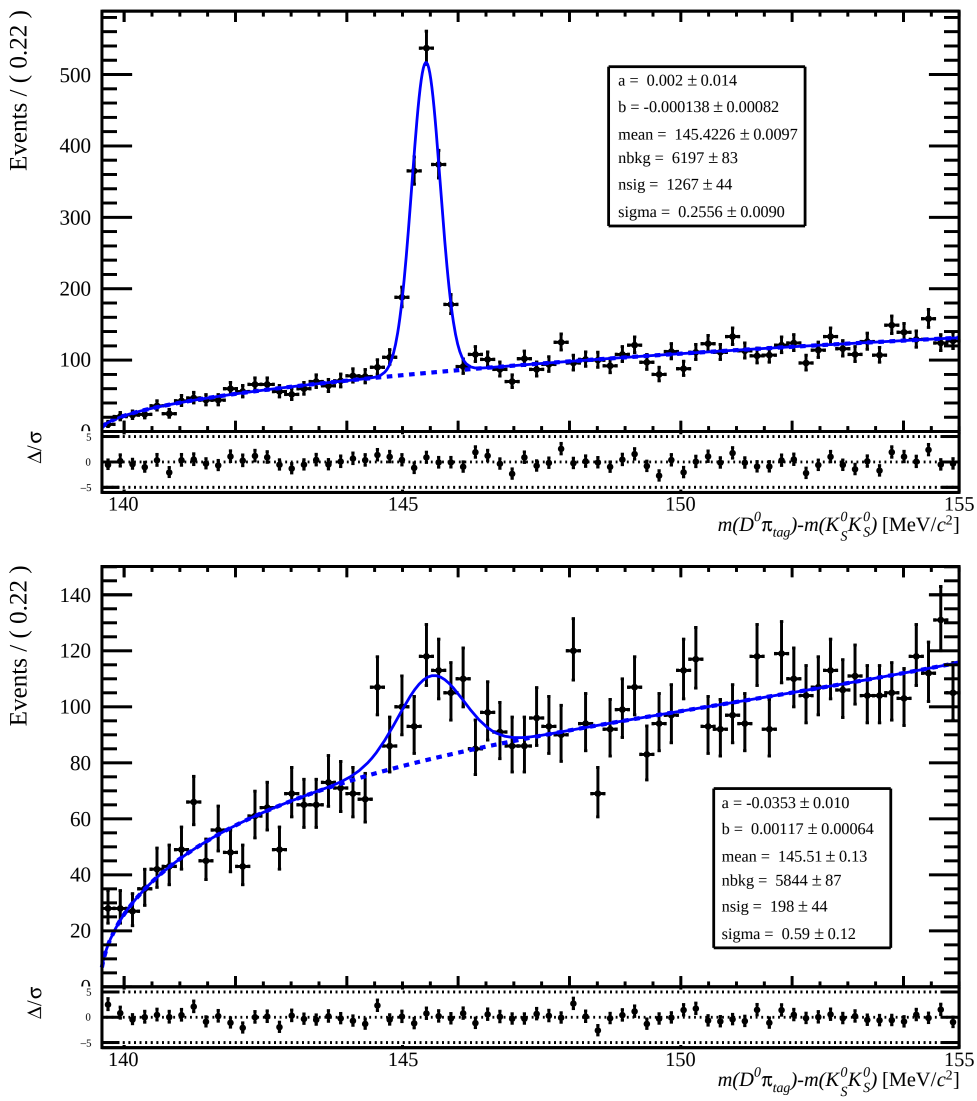

Figure 5.21: Δm distributions, relative fits and results for events for which $\Delta\chi^2$ is less than 8 (up) and more than 8 (down), for LL channel.

Combining these two results, the overall resolution is equal to 3.5% for the LL channel.

5.4.3 LD channel

Following the same procedure for LD channel events, I obtain the results shown in Figure 5.22. Also here the resolution has improved for events with a $\Delta\chi^2$ under threshold, where it is 8.9%; for the other considered subsample, the yield is really low and the resolution is equal to 41.6%.
The combination of these gives a statistical sensitivity that is equal to 8.7% for the LD channel.

Applying the analysis here set up, and after splitting the sample depending on the $\Delta\chi^2$ value, allows to reach a resolution equal to 3.5% and 8.7%, respectively for the LL and LD sample. From this comparison emerges that including secondary decays in the

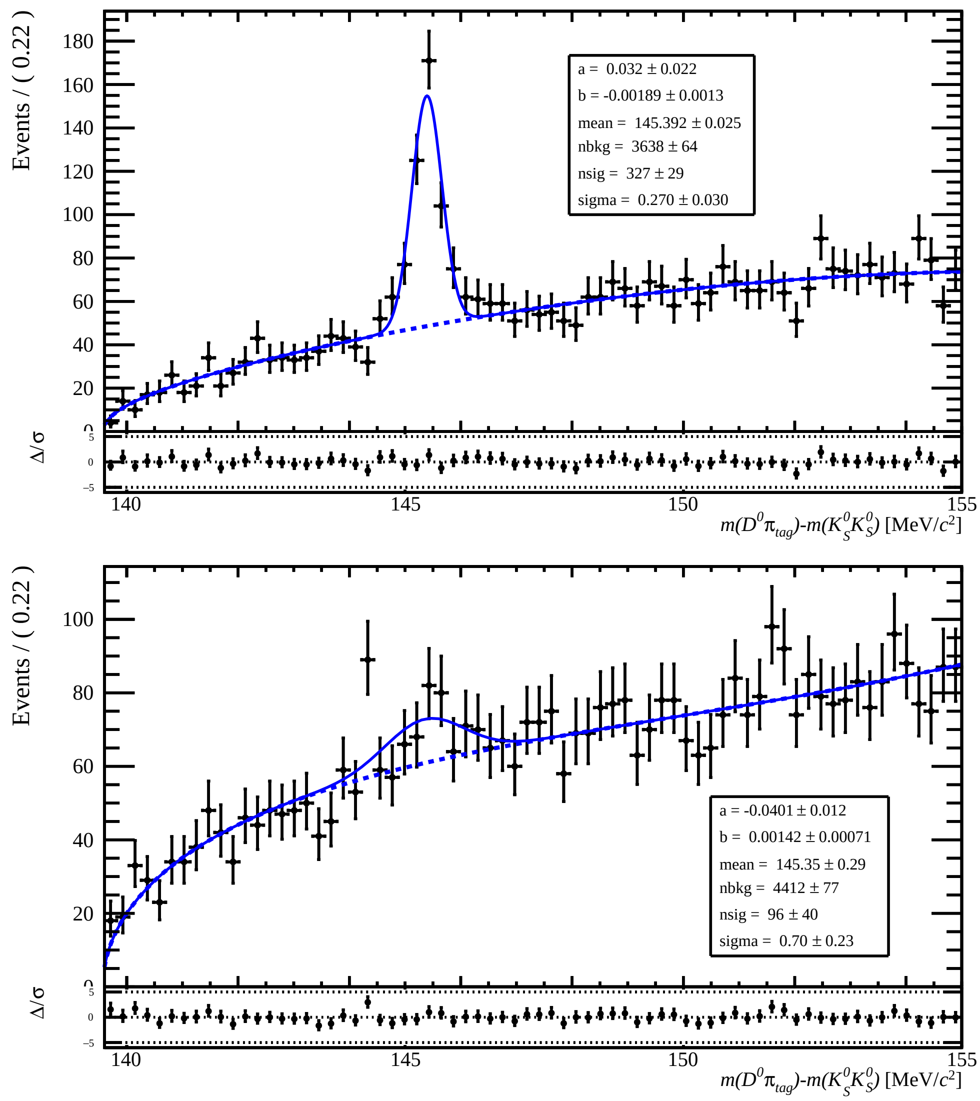

Figure 5.22: Δm distributions, relative fits and results for events for which $\Delta\chi^2$ is less than 8 (up) and more than 8 (down), for LD channel.

sample, and then splitting it as shown, does not limit the statistical sensitivity that can be achieved, and on the contrary, it is possible to achieve a better resolution with respect to the one given by the traditional analysis.

Chapter 6

Precision asymmetry calibration

In this chapter I will analyze the lifetime-unbiased $D^0 \to K^+K^-$ sample, adopted here as control channel. I will analyze it, extracting its $\mathcal{A}^{raw}$ and correction parameters due to present trigger cuts.

6.1 Control sample analysis

The control channel adopted in this analysis is the so-called "lifetime-unbiased" $D^0 \to K^+K^-$ sample. This is a special-purpose sample very different from the one used in the $\Delta\mathcal{A}^{CP}$ measurement (Chapter 1). It has been collected with trigger selection that applies the minimum possible bias to the impact parameters of the $K^\pm$. Its original motivation had nothing to do with the present analysis (it was mainly about precision D^0 lifetime) - but, as it will be seen in the following, we found the way to use it very effectively for our purposes.
This sample has two features that are crucial for the calibration of our analysis. The first is the equality between $\mathcal{A}^{prod}$ and $\mathcal{A}^{det}$ values for the signal and calibration samples, necessary for the $\mathcal{A}^{CP}$ ($D^0 \to K^0_S K^0_S$) extraction; this is expected since in both cases the D^0 comes from a D^* decay and the two decay chains differ only for the D^0 decay channel, that is a CP-eigenstate, not influencing $\mathcal{A}^{det}$. The other essential condition is the absence (nearly complete) of cuts that can bias the fraction of secondary decays through cuts that can not be reproduced in the signal sample. In the next sections I will discuss in details the features of this sample, and what needs to be done to make it possible to use it as a calibration sample for my measurement.

6.1.1 Lifetime-unbiased $D^0 \to K^+K^-$ trigger selection

The HLT1 and HLT2 selections adopted by the "lifetime-unbiased" sample are summarized in Table 6.1 and 6.2. It is important to carefully compare these requirements to our signal sample. This is done in Table 6.1 and 6.2, and in the ones shown in 4.2.
Some cuts present in the selection are applied on quantities that stands only for one of the two samples, for example, the requirement on the track reconstruction quality for the $K^\pm$ in the control sample.
The presence of different cuts on kinematic variables in $K^0_S K^0_S$ and K^+K^- selections can introduce sizable differences in events kinematics. However the application of identical

Variable	Cut
$p_{\mathrm{T}}\ (K^{\pm})$	> 800 MeV/c
$p_{\mathrm{T}\ max}(K^{\pm})$	> 900 MeV/c
$p\ (K^{\pm})$	> 4000 MeV/c
$\chi^2\ _{track}(K^{\pm})$	< 2
$\sum_{p_{\mathrm{T}}}(K^{\pm})$	> 1500 MeV/c
$\lvert m(K^+K^-) - m(D^0)\rvert$	< 100 MeV/c^2
$DOCA_{min}(K^+K^-)$	< 0.2 mm
$\tau(D^0)$	> 0.2 ps
$\chi^2_{\mathrm{vtx}}/\mathrm{ndf}(D^0)$	< 10

Table 6.1: Summary of lifetime-unbiased $D^0 \to K^+K^-$ sample HLT1 selection.

Variable	Cut
$p_{\mathrm{T}}\ (K^{\pm})$	> 800 MeV/c
$p_{\mathrm{T}\ max}(K^{\pm})$	> 1200 MeV/c
$\chi^2_{\mathrm{vtx}}/\mathrm{ndf}(D^0)$	< 10
$\tau_{BPV}\ (D^0)$	> 0.25 ps
$DOCA_{min}(K^+K^-)$	< 0.2 mm
$\theta_{DIRA}(D^0)$	< 141.5 mrad
$p_{\mathrm{T}}\ (D^0)$	> 2000 MeV/c
$m(D^0\pi_{tag}) - m(K^+K^-)$	$\in [130,\ 160]$ MeV/c^2
$p_{\mathrm{T}}\ (\pi_{tag})$	> 200 MeV/c
$\mathcal{P}_{ghost}(\pi_{tag})$	< 0.25
$\chi^2/\mathrm{ndf}(\pi_{tag})$	< 3
$\chi^2_{\mathrm{vtx}}/\mathrm{ndf}(D^*)$	< 25
$cos(\theta_{DIRA}(D^0))$	> 0.9
TisTosSpec	TOS on Hlt1CalibTrackingKKDecision

Table 6.2: Summary of lifetime-unbiased $D^0 \to K^+K^-$ sample HLT2 selection.

cuts would not cause different effects in the two samples for kinematic variables, since their resolution in both samples is good enough to guarantee they will have the same effects on the relative distributions. The only cuts, of this kind, that differs in the two selections, are those applied to the transverse momentum of the D^0 decay products: in the K^+K^- sample it is required p_{T} $(K^{\pm})$>800 MeV/c and $p_{\mathrm{T}\ max}(K^{\pm})$>1200 MeV/$c$, while in the $K^0_{\mathrm{S}}K^0_{\mathrm{S}}$ trigger selection it is required p_{T} (K^0_{S})>500 MeV/c and no constraint is placed on the K^0_{S} with maximum momentum. The equalization of these cuts will be discussed in 6.2.5.
Had the cut on the K^+K^- sample been looser than in the $K^0_{\mathrm{S}}K^0_{\mathrm{S}}$, the issue could have been easily fixed applying the tighter cut to both samples - given the large size of the K^+K^- sample, this would have no effect on the final precision of the result. In the other situation, we need to be more careful, not to waste precious signal.
Other cuts that have to be analyzed are the ones that can directly or indirectly bias the fraction of secondary decays in the control channel. The only explicit bias is due to the τ_{BPV} (D^0) cut, that rejects events where τ_{BPV} (D^0) assumes a value smaller than 0.25 ps; it is important to notice that even if this cut reject an events fraction, it does not distort the τ_{BPV} (D^0) distribution. A potentially dangerous cut, with an indirect effect on secondary decays is the one on the $\theta_{DIRA}(D^0)$, since it selects particles with a momentum pointing to the PV, with an effect similar to χ^2_{IP}. On $\theta_{DIRA}(D^0)$ two cuts are applied, but the significant one is the $\theta_{DIRA}(D^0) < 141.5$ mrad one, equal to $\cos(\theta_{DIRA}(D^0)) > 0.99$. The cut on $\theta_{DIRA}(D^0)$ is present in our signal sample too, and is much tighter ($\theta_{DIRA}(D^0) < 34.6$ mrad) than the one applied on the control sample; this difference can be significant for the analysis. For $\theta_{DIRA}(D^0)$ the resolution is very different in the two samples, therefore cuts can not simply be equalized, since the same cut does not affect in the same way the fraction of secondary decays in the two samples. The effect of this cuts will be analyzed in detail later and it will be seen not to be a problem.
Finally, the most problematic requirement is the τ_{BPV} (D^0) cut. This is definitely going to have an effect on the fraction of secondaries, that we need to deal with somehow. This is a trigger cut, so we cannot remove it; we cannot apply to the signal sample either, because the resolution there is much different - so it is a real problem. Two facts however come to out help:

- the cut is much lower than in the standard $D^0 \to K^+K^-$ sample; this means that its effect is much reduced;

- the cut is much "sharper", being a direct cut and not an indirect consequence of cuts on the individual tracks; efficiency goes to nearly 100% immediately above the cut. This causes it to affect mainly the primary decays, leaving secondaries nearly unaffected.

The bottom line of all this is, even if this cut cannot be neither eliminated nor equalized, its effect is sufficiently small and predictable that we can instead plan for calculating its effect and explicitly correct our $\mathcal{A}^{CP}$ results for it - so we will make this our plan.
Other cuts present in the selections are the ones on the track- or vertex-reconstruction quality; these are equal in both samples, but even if different, they does not represent a problem, since they does not affect the of secondary decays fraction.

6.1.2 Analysis of the control sample

It is interesting to take a first look at the control sample before any selections, to understand the present signal to background ratio. This can be seen from Figure 6.1, where Δm and D^0 candidates mass distribution for the control sample are shown. From these plots it

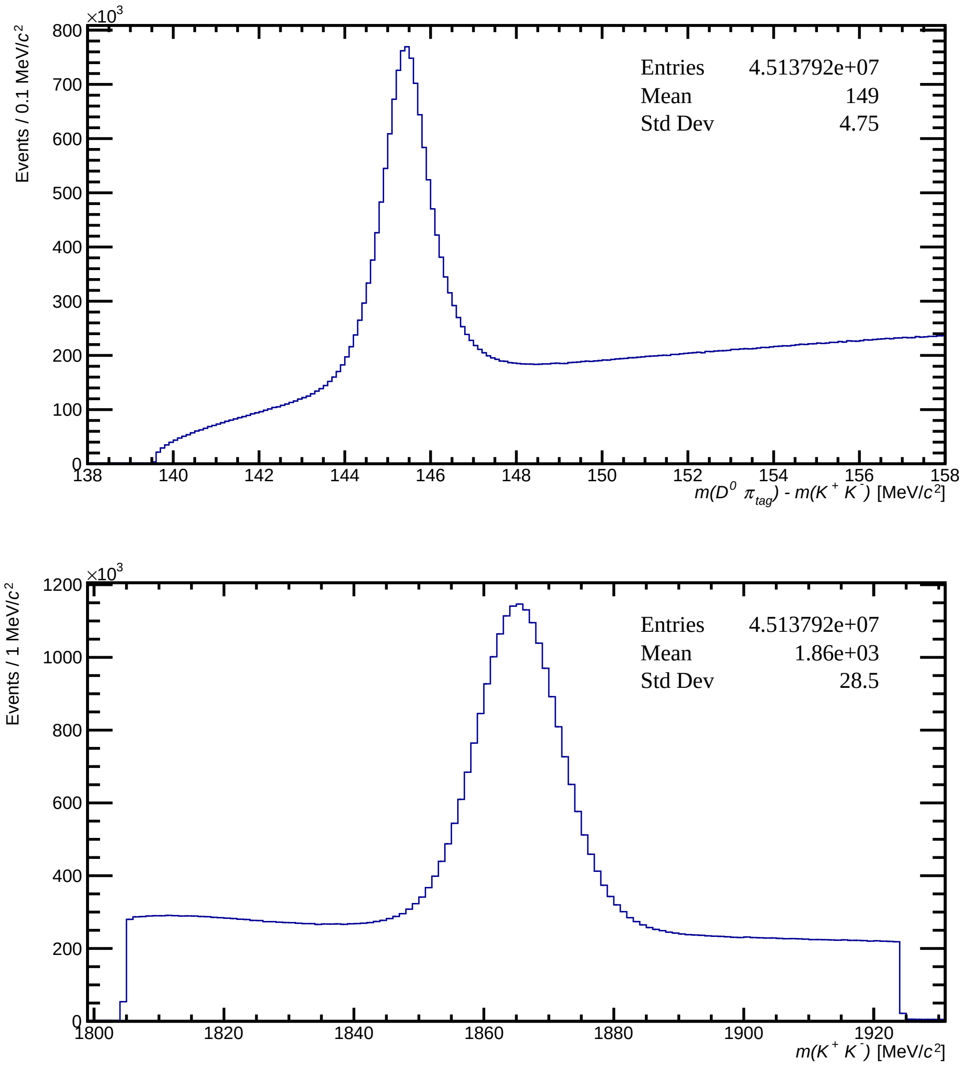

Figure 6.1: Δm (up) and D^0 mass candidates (down) distributions for $D^0 \to K^+K^-$ decay events. Fiducial and L0 cuts are applied.

is apparent the considerable difference between the signal and control sample purity; even without any cut, the $D^0 \to K^+K^-$ signal to background ratio is significantly larger to the signal one, in both Δm and $m(D^0)$ distributions. This is significant: since this sample has been collected with loose cuts, the signal to background ratio is not obvious. The plots assures the small background contribution that allows to achieve the required resolution on $\mathcal{A}^{CP}$ (K^+K^-). Another interesting variable is the uncertainty on the D^0 decay vertex position in this channel, shown in Figure 6.2. As can be seen from the distribution mean value, for the K^+K^- sample the resolution on the D^0 decay vertex determination is much better than in the $K^0_S K^0_S$ sample as it would be expected. This implies that, if we want

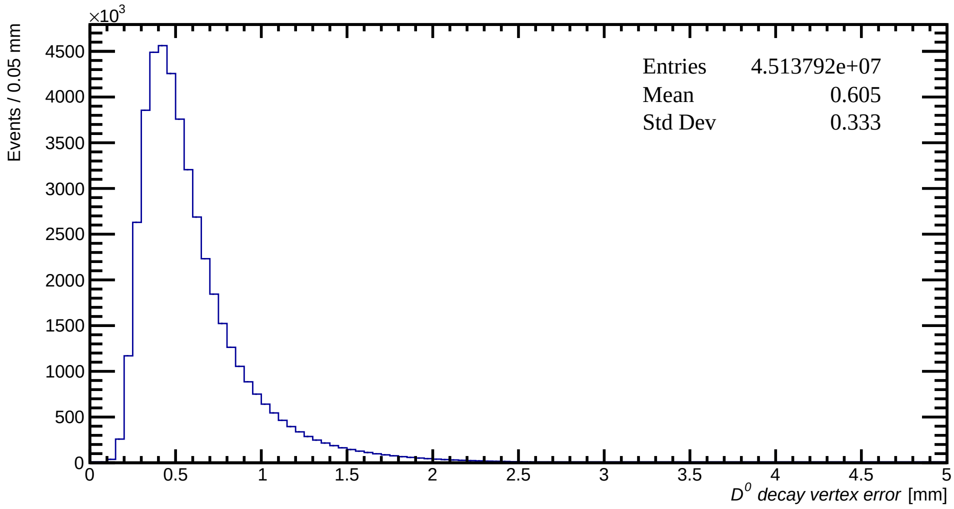

Figure 6.2: Distribution of the uncertainty on the D^0 decay vertex position for $D^0 \to K^+K^-$ decay events. Fiducial and L0 cuts are applied.

to keep equal fraction of secondary decays in the two samples we must never cut on this type of variables, as the effect of the same nominal cut would be completely different in the two samples.

6.1.3 Selection application

These first analysis steps confirmed that the control sample has the expected properties. To extract the $\mathcal{A}^{raw}$ value of the complete sample, it is necessary to apply to the control sample the selections already identified on the $K^0_S K^0_S$ sample, to equalize detection asymmetry. For the K^+K^- sample all particles are detected with Long tracks, therefore are not defined different channels. For this reason the same sample, shown in previous plots, will be adopted as control channel for both LL and LD channels, applying the two different selections, identified for the $K^0_S K^0_S$ channels.
The selections that will be applied to the $D^0 \to K^+K^-$ sample can not be equal to the ones of the $D^0 \to K^0_S K^0_S$ events, since, as happened for the trigger cuts, only a part of the involved variables are defined in both kinds of event.
The selection applied to $D^0 \to K^+K^-$ events to identify the LL channel control sample are:

- Fiducial cuts;
- L0 trigger requirements: D0_L0HadronDecision_TOS $\vee$ DS_L0Global_TIS;
- $|m(D^0) - 1864.4\,\mathrm{MeV}/c^2| < 20\,\mathrm{MeV}/c^2$;
- $p_\mathrm{T}\ (\pi_{tag}) > 225\ \ \mathrm{MeV}/c$.

The ones applied to identify the LD channel control sample are:

- Fiducial cuts

- L0 trigger requirements: D0_L0HadronDecision_TOS $\vee$ DS_L0Global_TIS;
- $|m(D^0) - 1864.4\,\text{MeV}/c^2| < 20\,\text{MeV}/c^2$;
- $p_{\text{T}}\ (D^0) > 4000\ \ \text{MeV}/c$.

After the application of these cuts it is interesting to analyze the Δm distributions, to understand how the selections affected the K^+K^- sample. The Δm distributions of LL and LD channel control samples are shown in Figure 6.3. From the plots emerges that

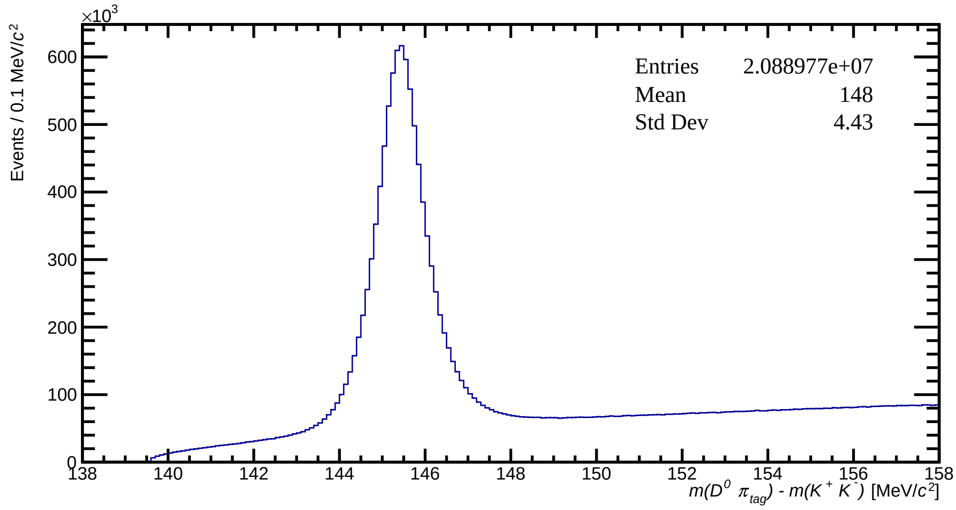

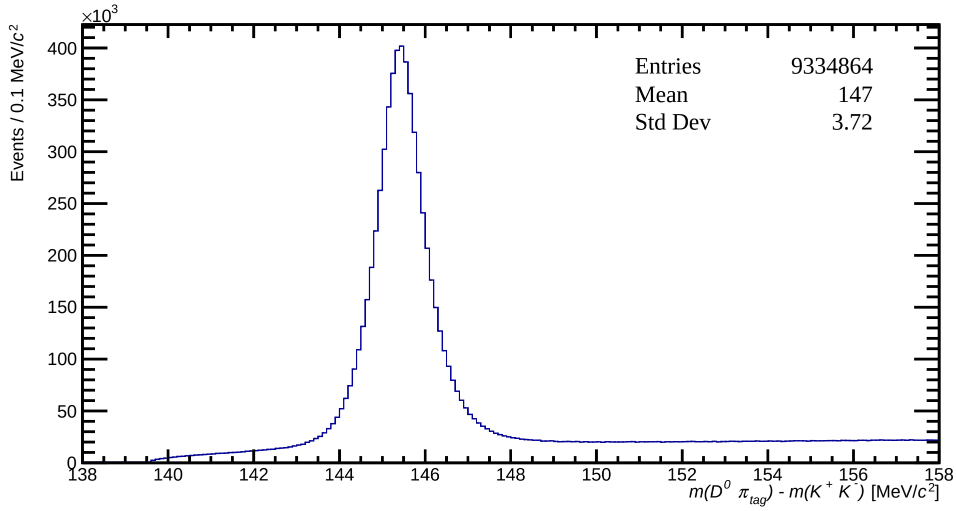

Figure 6.3: Δm distributions for control samples adopted for LL (up) and LD (down) signal samples.

the selections improve the signal purity, rejecting a significant background component. This was expected, since the selections, even if identified on the $K^0_{\text{S}}K^0_{\text{S}}$ sample, aim to signal events. It can be noticed the different effect of the two selections: the LD channel selection rejects a larger background component with respect to the LL one. This is most probably due to the cut applied on $p_{\text{T}}\ (D^0)$; it is an hard cut and is present only in the LD selection. The difference between the two samples does not represent a problem, since the two samples will be analyzed separately.

6.1.4 $\mathcal{A}^{raw}$ variation

Before proceeding I analyzed the $\mathcal{A}^{raw}$ variation as a function of χ^2_{IP} (D^*) for the control sample. This provides significant information because, for different χ^2_{IP} (D^*) values, the sample is composed by a different fraction of secondary decays, in particular the sample at low χ^2_{IP} (D^*) is nearly pure primary, while at high χ^2_{IP} (D^*) it becomes pure secondary decays. The $\mathcal{A}^{raw}$ dependence on the different sample composition is partially due to the $\mathcal{A}^{det}$ variation for prompt and secondary decays, that can have different kinematic distribution, but for the most part it is caused by the different $\mathcal{A}^{prod}$ of the two kind of events, as already discussed in 4.3.1. The difference in $\mathcal{A}^{raw}$ between low and high χ^2_{IP} (D^*) values is a crucial observable with a rich phyisics content, to measure the difference between $\mathcal{A}^{prod}$ for primary and secondary decays. This quantity, multiplied for the fraction of secondary decays, has already been used in past analysis ([40]) to estimate the systematic uncertainty on $\mathcal{A}^{CP}$, due to the presence of residual contamination of secondary decays in the sample, after their rejection.
For this purpose I divided the sample in χ^2_{IP} (D^*) bins, and then extracted the value of $\mathcal{A}^{raw}$ for each bin, counting events present in Δm distributions tagged with opposite π_{tag} sign. To extract the number of events present in the peak I fitted the background contribution in the Δm region outside $\Delta m \in [141, 150]$ MeV/c^2, defined as signal region. The adopted *p.d.f.* is:

$$f_{bkg}(x) \propto \sqrt{x - m_\pi}[1 + a \cdot (x - m_\pi) + b \cdot (x - m_\pi)^2]$$

I perform in this case a minimum χ^2 fit, instead of a maximum likelihood one. This choice, in fact, helps the fit convergence, difficult in case of an high statistic sample, as the $D^0 \to K^+K^-$ one. Through the extraction of the background shape I extrapolated the number of background events in the signal region. With this I computed the number of signal events, from the difference between the overall events in the signal region and the background contribution extracted from the fit.
The $\mathcal{A}^{raw}$ values extracted for each χ^2_{IP} (D^*) bin, and the relative mean value are reported in Table 6.3. These values are plotted in Figure 6.4 in function of the χ^2_{IP} (D^*) mean values.
The trend expected for this plot is monotonic increasing, since:

χ^2_{IP} (D^*) bin	$<\chi^2_{\text{IP}}$ $(D^*)>$	$\mathcal{A}^{raw}$ [%]
<0.85	0.39	-0.97 ± 0.09
0.85 - 2.25	1.49	-0.99 ± 0.09
2.25 - 4.85	3.39	-0.85 ± 0.11
4.85 - 11.45	7.59	-1.1 ± 0.2
11.45 - 19.49	15.06	-0.36 ± 0.8
19.49 - 31.35	24.86	0.4 ± 1.2
31.35 - 61.76	44.42	1.8 ± 1.1
61.76 - 113.85	84.46	-1.6 ± 1.1
>113.85	1498	0.72 ± 0.48

Table 6.3: Identified χ^2_{IP} (D^*) bins, corresponding χ^2_{IP} (D^*) mean values and extracted $\mathcal{A}^{raw}$.

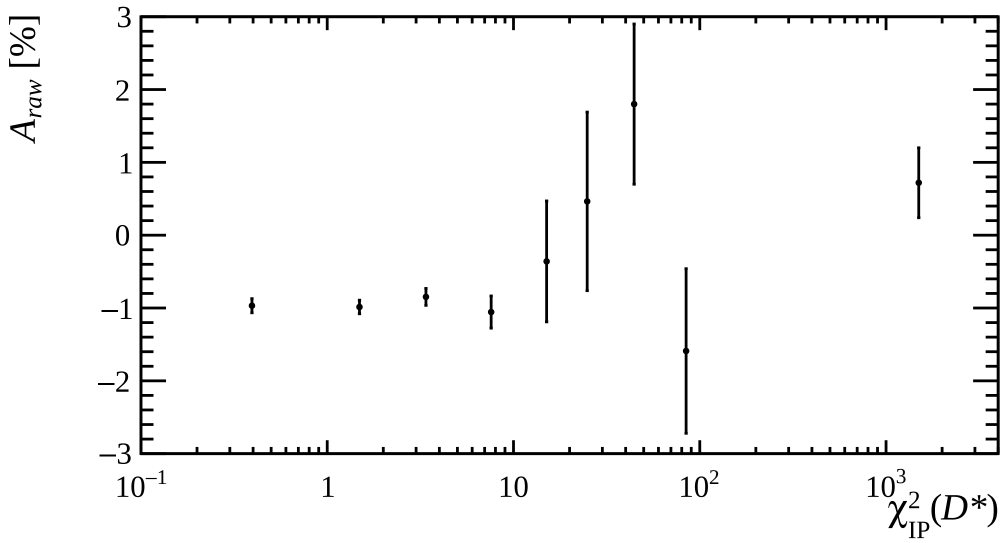

Figure 6.4: $\mathcal{A}^{raw}$ values in function of χ^2_{IP} (D^*) for control channel events.

- one expect that the χ^2_{IP} (D^*) cut does not significantly affect the prompt and secondary decays kinematics;
- the fraction of secondary decays is a monotonic increasing function of the χ^2_{IP} (D^*);
- the measured $\mathcal{A}^{raw}$ value in each bin can is a linear function of the fraction of secondary decays, and a linear function is monotonic increasing.

Indeed, the plot in Figure 6.4 seems to follow the behavior predicted by the above considerations. The size of the variation between the two ends of the plot is an important quantity, and one that is not very easy to predict without a direct measurement, as it is the product of a complex set of physics effects. Had it been negligible, the effort to carefully balance the fraction of secondary decays between the two samples would be pointless, since $\mathcal{A}^{prod}$, and hence $\mathcal{A}^{CP}$, are not biased by the presence of D^* coming from b-hadrons. On the other hand, if it had had a larger value (*e.g.* some ten percent) it would have been really difficult to precisely correct for deviations of secondary contaminations. From the plot it can be seen that the situation is in the middle ground between those extreme possibilities, justifying the strategy we have adopted.

6.2 Comparison after selection

After the application of the identified selections to both signal and control sample the subsamples on which the measurement will be done are identified. At this point it is possible to check the effect of the cuts.

6.2.1 $\theta_{DIRA}(D^0)$ cut

The first necessary check is aimed to understand if, and how, the mentioned trigger cuts ($\theta_{DIRA}(D^0)$ e $\tau_{BPV}(D^0)$) influence the distributions of events significant for the measurement.

The first analyzed cut is the one on $\theta_{DIRA}(D^0)$. This cut is present both in signal and control sample, much tighter on the $D^0 \to K^0_S K^0_S$ one, can bias the secondary events fraction, selecting events with a momentum pointing toward the PV.
To understand if the cut influences the signal events it is important to plot the θ_{DIRA} (or $cos(\theta_{DIRA})$ as done here for simplicity) distribution of those events only. This is done differently for signal and control sample. In the former, the background component requires a sideband-subtraction procedure, performed identifying a signal region (the peak region in Δm distribution) and its sidebands as done before (the Δm plot will not be shown since it corresponds to the one represented in Figure 5.18). For the control sample the background component represents a small fraction of the events in the Δm peak region. So to plot the signal distribution I simply selected the peak region. To avoid as much as possible the presence of background events I adopted a narrower Δm window with respect to the analysis shown in the previous section. Are considered signal events the ones for which $\Delta m \in [144., 147.]$ MeV/c^2.
$\cos(\theta_{DIRA})(D^0)$ distributions for the $K^0_S K^0_S$ sample are shown in Figure 6.5. From the shown plots emerges a significant difference between the signal and background component distributions. The signal distributions suggest that the cut does not significantly affect signal events. I checked this hypothesis fitting the signal distributions with a constant term, in the region at smaller $\cos(\theta_{DIRA}(D^0))$: the fit results show that the signal distribution in that region is compatible with zero. This assures that the $\theta_{DIRA}(D^0)$ cut does not affect signal events. The fits are shown in Figure 6.6.
$\cos(\theta_{DIRA})(D^0)$ distributions for the control samples are shown in Figure 6.7. Here the cut is looser than the one on the signal sample and emerges clearly that it removes only a small fraction of the distribution tail (it is important to notice the logarithmic scale on the vertical axis) and does not significantly influence signal events.
From the above considerations we can safely conclude that the $\theta_{DIRA}(D^0)$ cuts do not affect the distributions of signal events in either sample in any appreciable way and can be therefore neglected.

6.2.2 $\tau(D^0)$ cut

The influence on signal events given by the $\tau_{BPV}(D^0)$ cut has to be analyzed, too. In the $K^0_S K^0_S$ sample this cut is not present, while, for the K^+K^- one, it is required a minimum τ_{BPV} (D^0) value of 0.25 ps. This corresponds to a requirement on the distance between the D^0 decay vertex and the PV. This introduces a bias on the fraction of secondary decays, since it more likely selects particles coming from the decay of a b-hadron, that travel a longer distance on average. I first checked if the τ_{BPV} (D^0) distribution in the K^+K^- sample has been influenced by the cut. To select signal events I applied a cut on Δm, as done in the previous section.
The τ_{BPV} (D^0) distributions for the control samples are shown in Figure 6.8. These distributions show a trend that is approximately exponential, due to the presence of prompt D^0. A deviation from that trend is expected, due to the presence of secondary decays, that appears as a longer tail at higher τ_{BPV} (D^0). From this plot clearly emerges how the cut influences the distributions, rejecting a large fraction of events, at τ_{BPV} (D^0) smaller than the set limit, that are mostly prompt events. Because of this, the cut biases the fraction of secondary decays, making it assume a different value from that of the signal sample, where this cut is not applied and, mos importantly, can not be reproduced,

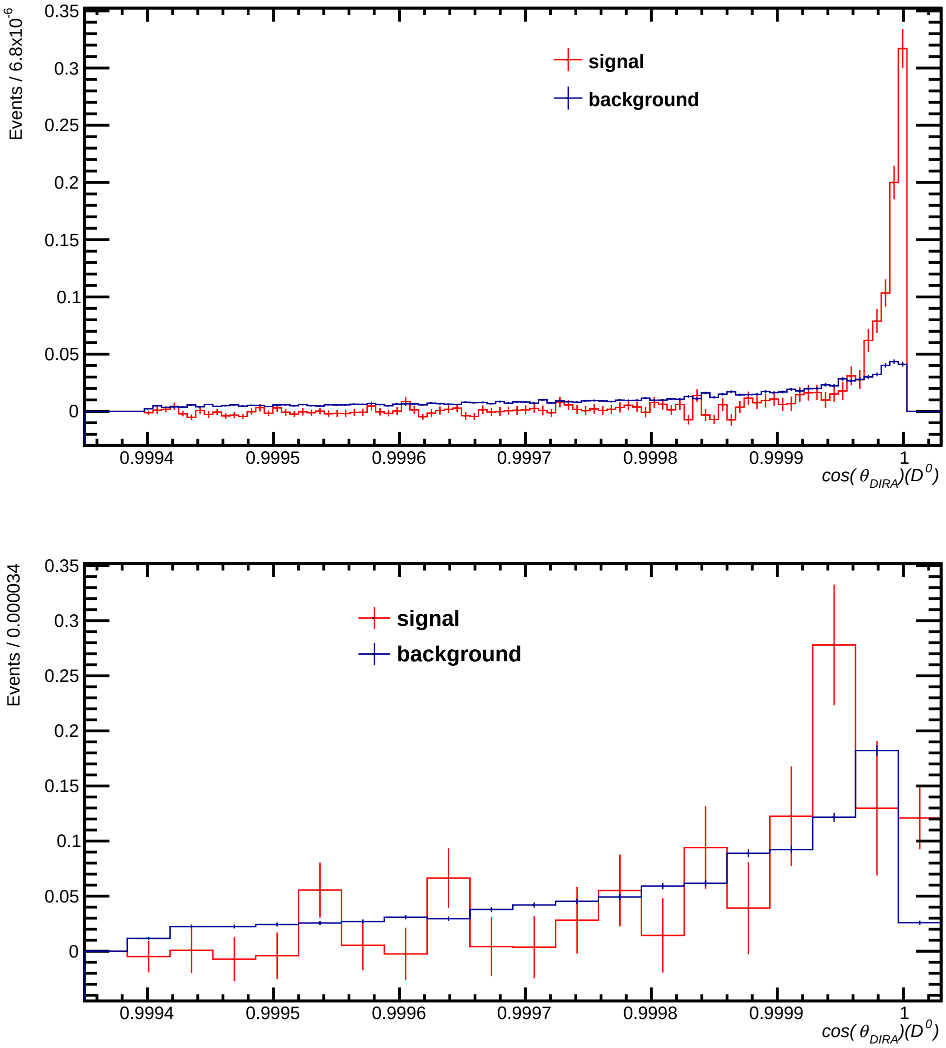

Figure 6.5: $\cos(\theta_{DIRA}(D^0))$ distributions for LL (up) and LD (down) channel, for both signal and background component.

because of the different vertex resolution. This represents a serious issue for this analysis, since it introduces already at trigger level, an effect, strictly avoided in the off-line analysis, that biases the $\mathcal{A}^{CP}$ $(K^0_S K^0_S)$ value extracted from $\Delta\mathcal{A}^{CP}$.

6.2.3 $\mathcal{A}^{raw}$ (K^+K^-) correction

Our analysis strategy, that can be applied even with the presence of the τ_{BPV} (D^0) cut, is based on the calculation of a correction, to be applied to $\mathcal{A}^{raw}$ (K^+K^-). This correction is the difference between the values assumed by $\mathcal{A}^{raw}$ (K^+K^-) with, and without, that cut. Adding this quantity to the $\mathcal{A}^{raw}$ (K^+K^-) value extracted from the sample, where the bias due to the cut is present, one can have access to the unbiased $\mathcal{A}^{raw}$ value, the one needed in the $\mathcal{A}^{CP}$ $(K^0_S K^0_S)$ extraction.
This procedure is based on the following assumptions:

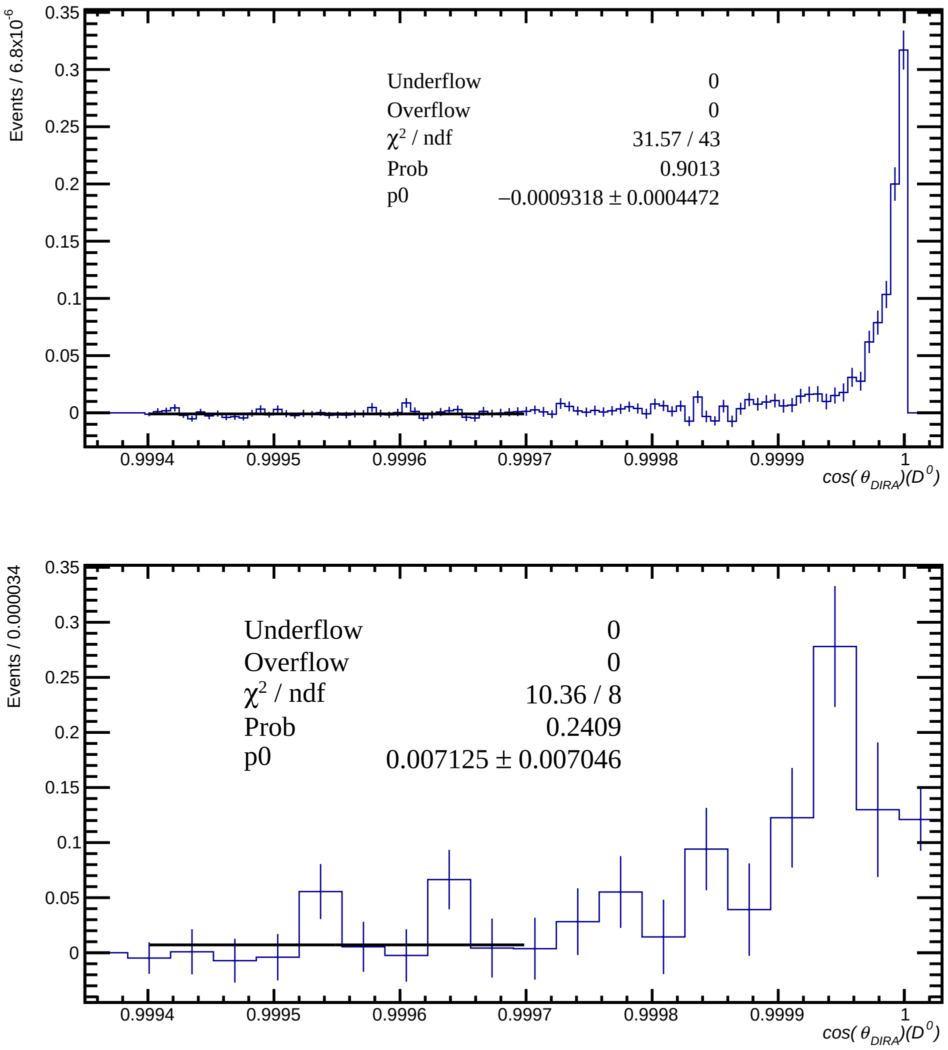

Figure 6.6: $cos(\theta_{DIRA}(D^0))$ distributions for LL (up) and LD (down) channel signal component. Polynomial of grade zero fit is superimposed, together with its results.

- τ_{BPV} (D^0) is independent from the event kinematics; indeed, the trigger was designed in order to apply the least possible bias on that variable;
- the kinematics is not influenced by the τ_{BPV} (D^0) cut, since this is a physical variable, computed taking into account the particle momentum.

If these conditions apply, it is possible, after the LL and LD selections application, to extract the unbiased $\mathcal{A}^{raw}$ (K^+K^-) value.
We start writing $\mathcal{A}^{raw}$ (K^+K^-) as:

$$\mathcal{A}^{raw}(K^+K^-) = (1 - f_s)\mathcal{A}_p + f_s\mathcal{A}_s \tag{6.1}$$

where $\mathcal{A}_p$ and $\mathcal{A}_s$ are the asymmetries of primary and secondary decays, respectively, and f_s is the fraction of secondary decays in the sample, in the absence of the τ_{BPV} (D^0) cut. In (6.1) is made explicit the different contribution given by the presence of both primary and secondary decays in the sample, that have different asymmetry, as previously shown

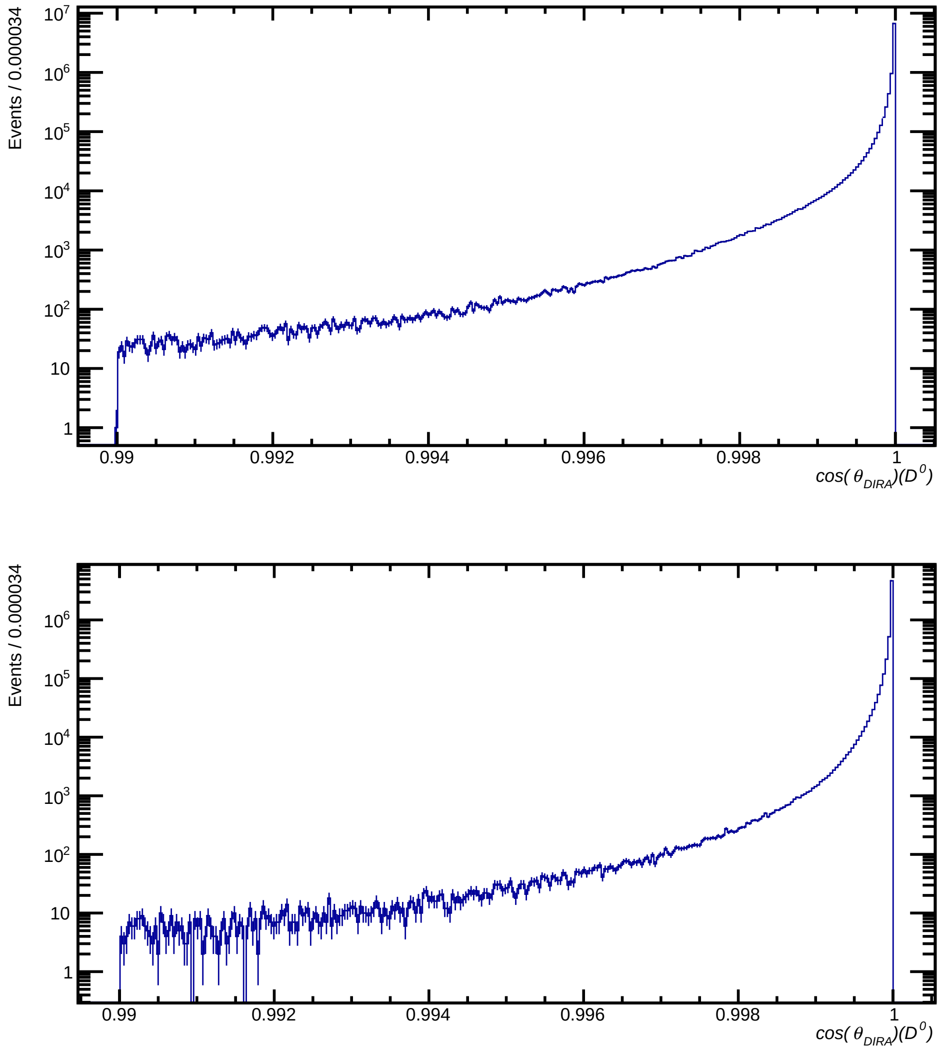

Figure 6.7: $cos(\theta_{DIRA}(D^0))$ distributions for control samples adopted for LL (up) and LD (down) channels, for signal component.

in 6.1.4. Each component contribute with a weight, corresponding to the fraction of those events, here expressed as a function of only f_s. In this notation it is simple to see the effect of the τ_{BPV} (D^0) cut in biasing the $\mathcal{A}^{raw}$ (K^-K^+) value, since it modifies the mixture, between primary and secondary decays, of which the sample is composed. Therefore $\mathcal{A}^{raw}$ (K^+K^-), considering the cut effect, can be expressed as:

$$\mathcal{A}^{raw}(K^+K^-)' = (1 - f_s')\mathcal{A}_p + f_s'\mathcal{A}_s \tag{6.2}$$

where the primed variables are referred to the sample after the τ_{BPV} (D^0) cut. This is the asymmetry that can be actually measured on our sample.
From (6.1) and (6.2), it is simple to compute the difference between the two asymmetries:

$$\Delta\mathcal{A}^{raw}(K^+K^-) = \mathcal{A}^{raw}(K^+K^-)' - \mathcal{A}^{raw}(K^+K^-) = \Delta(f_s' - f_s) \tag{6.3}$$

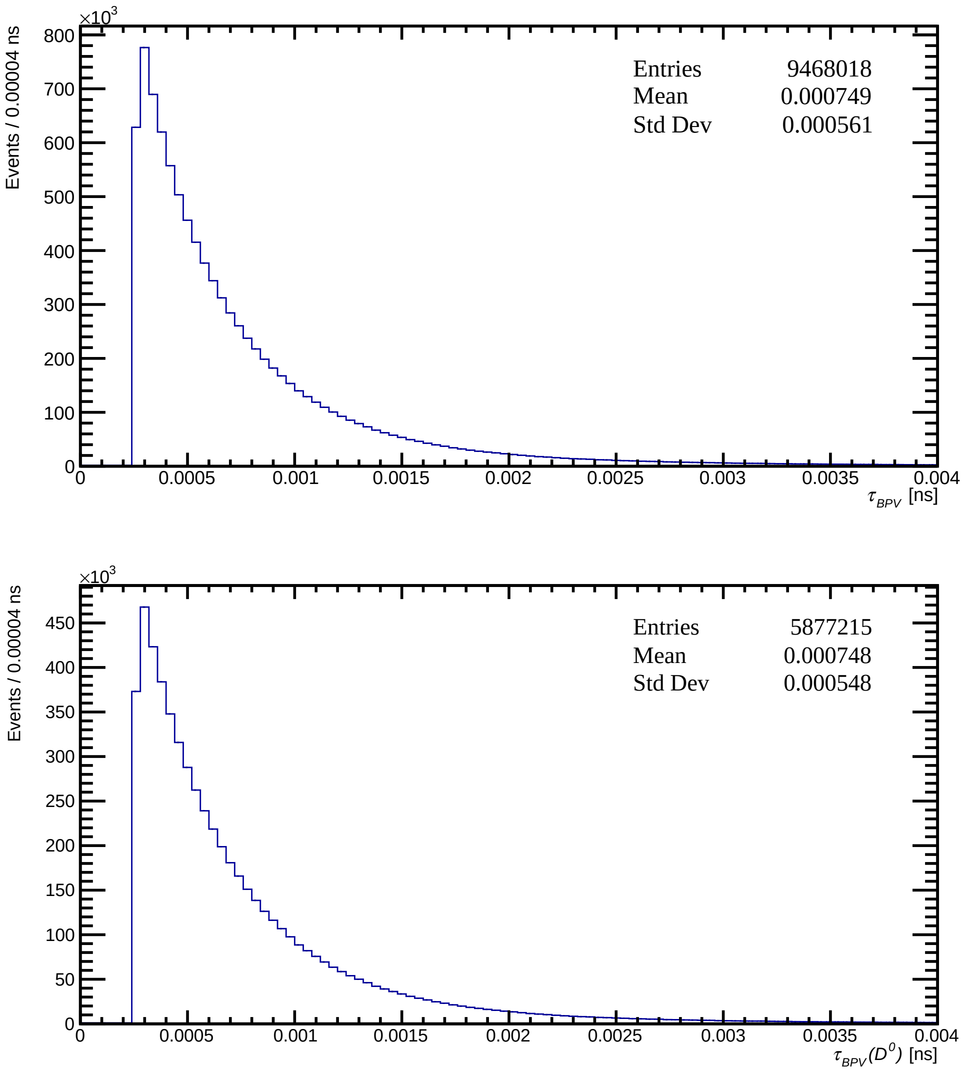

Figure 6.8: $\tau_{BPV}(D^0)$ distributions for control samples adopted for LL (up) and LD (down) channels, for signal component.

where $\Delta = \mathcal{A}_s - \mathcal{A}_p$. The quantity expressed in (6.3) is the correction that allows to extract the unbiased $\mathcal{A}^{raw}$ (K^-K^+) value, simply through:

$$\mathcal{A}^{raw}(K^+K^-) = \mathcal{A}^{raw}(K^+K^-)' - \Delta(f_s' - f_s) \tag{6.4}$$

It is necessary to measure the Δ and $(f_s'-f_s)$ values, separately for the sample identified by the LL and LD selections, for which the correction will assume different values.

Measurement of Δ

The difference between $\mathcal{A}_s$ and $\mathcal{A}_p$ can be gleaned from the values assumed by $\mathcal{A}^{raw}$ for high, and low $\chi^2_{\rm IP}$ (D^*) values, respectively, repeating the procedure applied in 6.1.4. I divided the two samples in $\chi^2_{\rm IP}$ (D^*) bins, measuring the $\mathcal{A}^{raw}$ in each bin.
The results for LL control sample are shown in Table 6.4 and in Figure 6.9.
The results for LD control sample are shown in Table 6.5 and in Figure 6.10. Rather

$\chi^2_{\rm IP}$ (D^*) bin	$<\chi^2_{\rm IP}$ $(D^*)>$	$\mathcal{A}^{raw}$ [%]	$\mathcal{A}^{raw}{}_{fit}$ [%]
<0.85	0.39	-0.81 ± 0.08	-0.94 ± 0.08
0.85 - 2.25	1.48	-0.97 ± 0.08	-0.91 ± 0.082
2.25 - 4.85	3.35	-0.85 ± 0.09	-0.85 ± -0.11
4.85 - 11.45	7.37	-0.70 ± 0.1	-0.82 ± 0.14
11.45 - 19.49	15.0	-0.73 ± 0.6	-0.7 ± 0.3
19.49 - 31.35	24.86	0.20 ± 0.8	-0.5 ± 0.4
31.35 - 61.76	44.48	0.3 ± 0.7	-0.4 ± 0.4
61.76 - 113.85	84.54	-1.46 ± 0.7	-0.2 ± 0.4
>113.85	1374	-0.46 ± 0.31	-0.1 ± 0.3

Table 6.4: Identified $\chi^2_{\rm IP}$ (D^*) bins, corresponding $\chi^2_{\rm IP}$ (D^*) mean values, measured $\mathcal{A}^{raw}$ values and $\mathcal{A}^{raw}$ extracted form the monotonic fit, for the LL channel control sample.

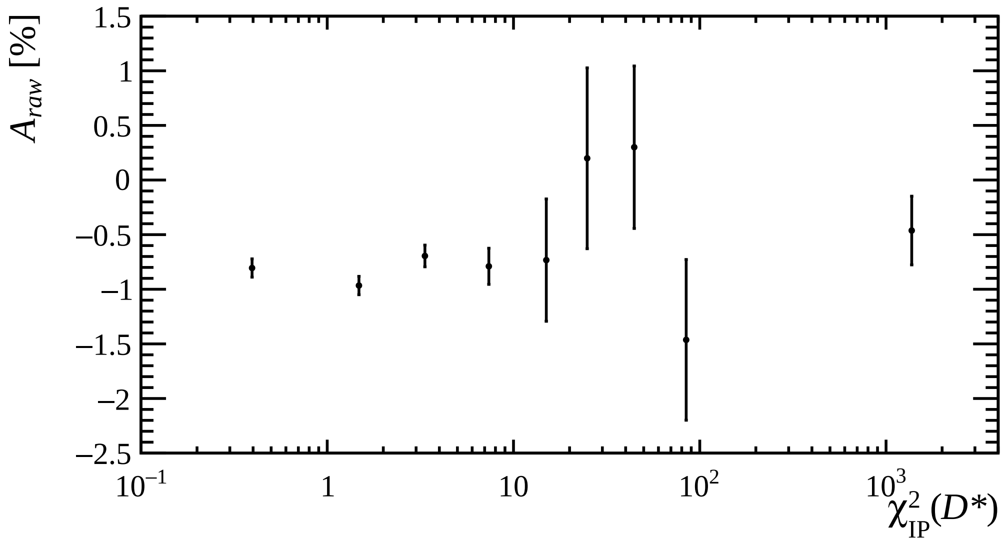

Figure 6.9: $\mathcal{A}^{raw}$ values in function of $\chi^2_{\rm IP}$ (D^*) for LL channel control channel.

$\chi^2_{\rm IP}$ (D^*) bin	$<\chi^2_{\rm IP}$ $(D^*)>$	$\mathcal{A}^{raw}$ [%]	$\mathcal{A}^{raw}{}_{fit}$ [%]
<0.85	0.39	-0.83 ± 0.09	-0.91 ± 0.09
0.85 - 2.25	1.48	-1.00 ± 0.09	-0.91 ± 0.09
2.25 - 4.85	3.32	-0.6 ± 0.1	-0.76 ± 0.12
4.85 - 11.45	7.16	-0.73 ± 0.17	-0.76 ± 0.14
11.45 - 19.49	14.9	-0.8 ± 0.5	-0.76 ± 0.20
19.49 - 31.35	24.91	-0.6 ± 0.7	-0.76 ± 0.26
31.35 - 61.76	44.65	-0.7 ± 0.6	-0.76 ± 0.29
61.76 - 113.85	84.57	-1.1 ± 0.7	-0.76 ± 0.33
>113.85	1269	-0.39 ± 0.28	-0.39 ± 0.26

Table 6.5: Identified $\chi^2_{\rm IP}$ (D^*) bins, corresponding $\chi^2_{\rm IP}$ (D^*) mean values and measured $\mathcal{A}^{raw}$ values and $\mathcal{A}^{raw}$ extracted form the monotonic fit, for the LD channel control sample.

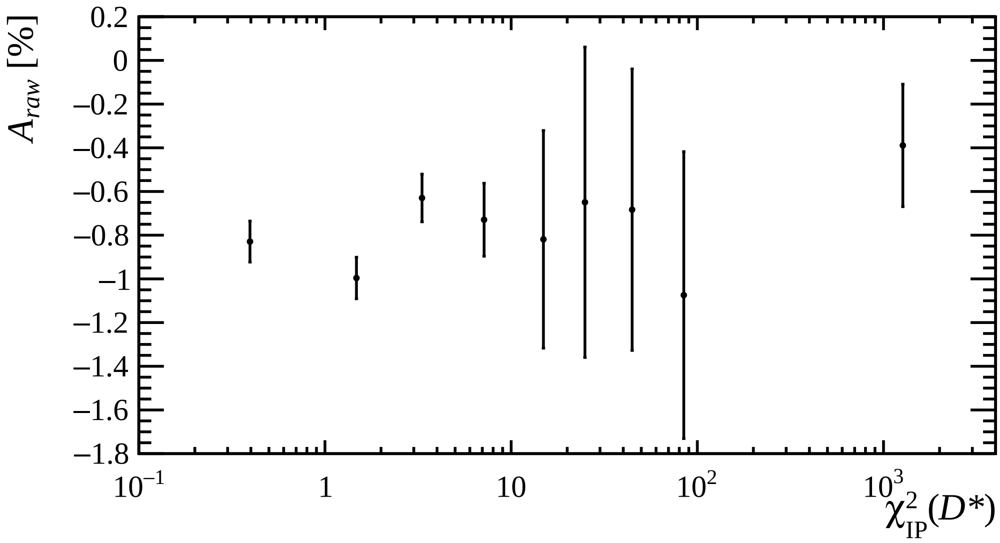

Figure 6.10: $\mathcal{A}^{raw}$ values in function of $\chi^2_{\rm IP}$ (D^*) for LD channel control channel.

than simply picking the extreme points of the plots as measured $\mathcal{A}^{raw}$ values, I devised a procedure to make use of the full information available in the plots via likelihood fit. However, the choice of a certain parametric function in the fit can bias the result, since the shape of the $\mathcal{A}^{raw}$ trend is not known. To avoid this, and exploiting the expected $\mathcal{A}^{raw}$ monotonicity, I decided to use a special procedure, generally known as *monotonic fit*. This is a procedure that, given an (x,y) dataset (in this case $\chi^2_{\rm IP}$ (D^*), $\mathcal{A}^{raw}$), returns the y values that represents the maximum likelihood estimate of the best monotonic increasing function that interpolate data. This is done through an algorithm that follows four steps:

- identification between y values of the *decreasing series*, defined as the sets of consecutive points where y assumes a decreasing value;
- if no decreasing series are present the y values corresponds to the maximum likelihood estimate;
- if decreasing series are present, y values of each series are replaced with the mean of the y values of the series;
- the three previous steps are repeated until no decreasing series is present.

The result obtained from the application of the monotonic fit to the LL and LD $\mathcal{A}^{raw}$ values are reported in Table 6.4 and 6.5. The uncertainties associated to the fitted values are expected to be smaller than the measured ones, since in the fit the monotonicity constrain is present. To estimate the uncertainties on the $\mathcal{A}^{raw}$ values extracted from fit, I performed a *bootstrap*. For each $\chi^2_{\rm IP}$ (D^*) bin I randomly generated a number, extracted from a Gaussian distribution with mean equal to the $\mathcal{A}^{raw}$ fitted value and standard deviation equal to the uncertainty on the corresponding measurement. I then applied the monotonic fit to the randomly extracted set, storing the result. I repeated this procedure one million times. The root mean square of the fitted $\mathcal{A}^{raw}$ values for each bin represents the uncertainty I associated to the fit results. In Figure 6.11 the distribution of the randomly extracted $\mathcal{A}^{raw}$ values is shown, for the bin at lowr $\chi^2_{\rm IP}$ (D^*) of the LD control sample.

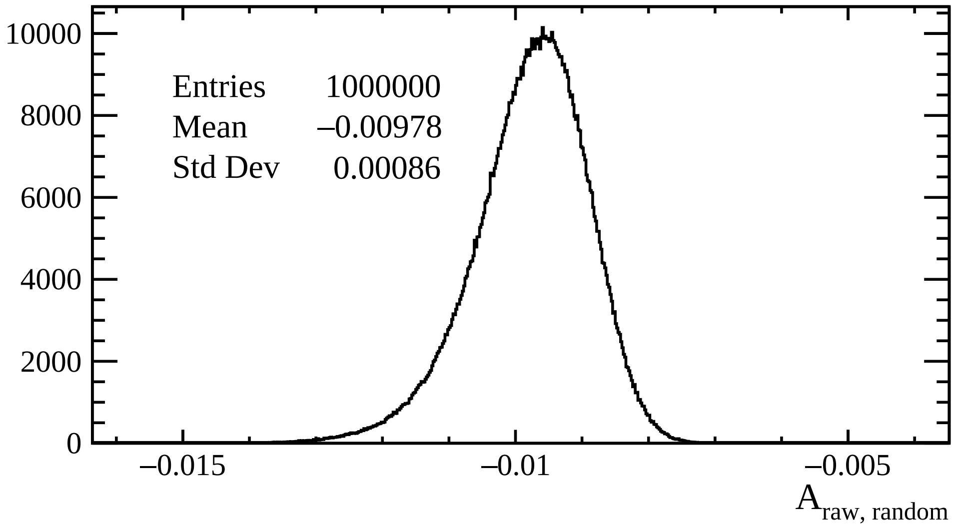

Figure 6.11: Randomly extracted $\mathcal{A}^{raw}$ values for the bin at smaller χ^2_{IP} (D^*) for LD control sample.

From this plot it is possible to see that the Gaussian distribution, from which data are extracted is modified by the applied fit, becoming clearly asymmetrical. Other bins are not shown for brevity.
From values reported in Table 6.4 and 6.5 it is possible to determine the Δ values, for LL and LD control channels:

$$\Delta_{LL} = (0.84 \pm 0.31)\% \tag{6.5}$$

$$\Delta_{LD} = (0.69 \pm 0.27)\% \tag{6.6}$$

At this point, it is necessary to observe that the extracted Δ values do not exactly correspond to the difference between the secondary and primary decays asymmetry. This because the $\mathcal{A}^{raw}$ even at χ^2_{IP} (D^*) is influenced by a residual fraction of secondary decays (ϕ_s). These are events for which the D^* momentum points toward the PV, that can not be discerned from prompt events. This implies that the measured difference between secondary and primary decays asymmetry, defined as $\tilde{\Delta}$, is different form Δ.These quantities are related as:

$$\Delta = \frac{\tilde{\Delta}}{1 - \phi_s} \tag{6.7}$$

The determination of ϕ_s is possible, but it is easy to see that it can be neglected in our case. In fact, even if it takes a value up to $\sim 10\%$ (is expected to be smaller), it does not modifies Δ in a significant way for our analysis purposes. In fact, as will be shown in the following sections, the $\mathcal{A}^{raw}$ (K^+K^-) correction is expected to be much smaller than the $\mathcal{A}^{CP}$ $(K^0_{\mathrm{S}}K^0_{\mathrm{S}})$ uncertainty, and its estimate does not need to be extremely precise, and the effect of a ϕ_s different from zero can be neglected.

Measurement of $f'_s - f_s$

The other quantity needed to compute the $\mathcal{A}^{raw}$ (K^+K^-) correction is the difference between the fraction of secondary decays in the sample, with and without the τ_{BPV} (D^0) cut. To extract f'_s and f_s I exploited the τ_{BPV} (D^0) distribution, already shown in

Figure 6.8, to get an estimate for the number of the prompt and secondary decays events that rejected by the cut. This is done by identifying two bins, near the cut: in bin(a) are present events for which $\tau_{BPV}(D^0) \in [0.25, 0.375]$ ps, for bin(b) $\tau_{BPV}(D^0) \in [0.375, 0.5]$ ps. From the number of entries in each bin it is possible to determine $f'_s - f_s$. This is possible assuming a known distribution for the two components. For prompt events is reasonable to assume an exponential distribution with a mean value equal to the D^0 lifetime ($\tau(D^0) = 0.41$ ps), since, as already discussed, the trigger adopted to collect the sample was designed to apply the lowest possible bias to the lifetime distribution. For secondary decays I assumed a constant distribution, at least in the region at small τ_{BPV} (D^0), where the cut affects the events. This is plausible since D^0 coming from secondary decays are expected to have a larger τ_{BPV}, because of the b-hadron decay time. These assumptions are confirmed by the plots shown in Figure 6.12. The prompt events distribution (identified appliyng to the complete sample the already adopted χ^2_{IP} (D^0) and χ^2_{IP} (D^*) cuts) is only slightly different from the expected distribution, represented in figure. The distribution for secondary decays is obtained through the subtraction between the complete sample and prompt events distributions; its shape confirms the goodness of the constant approximation near the cut.

Knowing the number of entries in the two identified bins it is possible to determine number of prompt events present in the sample if the τ_{BPV} cut was not present (N_p) and the number of secondary decays in the constant approximation (N_s), solving the two equations system:

$$N_a = N_p(e^{-0.25\,\mathrm{ps}/\tau_{D^0}} - e^{-0.375\,\mathrm{ps}/\tau_{D^0}}) + N_s \tag{6.8}$$

$$N_b = N_p(e^{-0.375\,\mathrm{ps}/\tau_{D^0}} - e^{-0.5\,\mathrm{ps}/\tau_{D^0}}) + N_s \tag{6.9}$$

The entries in each bin, together with N_p and N_s, for the LL and LD control channels, are reported in Table 6.6. What emerges from the extracted number of events is that,

Sample	N_a	N_b	N_p	N_s
LL	2334.4 ± 1.5	1674.6 ± 1.3	17114 ± 52	-124 ± 2
LD	1412.1 ± 1.2	1047 ± 1	9687 ± 41	51 ± 1

Table 6.6: Entries in a and b bins and extracted number of prompt and secondary decays, for LL and LD control samples. All values are expressed in 10^3 units.

as already supposed, the prompt events rejected by the cut are three, or four, order of magnitude more than the secondary ones. Since events coming from the decay of a b-hadron are only $O \sim \%$ of the total at small τ_{BPV} (D^0), the extracted N_s in the present approximation is not significant, and shows only that are compatible with zero. Therefore the variation of secondary decays fraction can be attributed only to the rejection of prompt events, and in the calculation of f'_s and f_s they can be considered as a constant.

The fractions of secondary decays in the sample can then be extracted through:

$$f'_s = \frac{N_s}{N_s + N'_p} = \frac{N'_{tot} - N'_p}{N'_{tot}} = \frac{N'_{tot} - N_p e^{-(0.25\,\mathrm{ps}/\tau_{D^0})}}{N'_{tot}} \tag{6.10}$$

and:

$$f_s = \frac{N_s}{N_s + N_p} = \frac{N_{tot} - N_p}{N_{tot}} = \frac{N'_{tot} - N_p e^{-(0.25\,\mathrm{ps}/\tau_{D^0})}}{N'_{tot} + N_p(1 - e^{-(0.25\,\mathrm{ps}/\tau_{D^0})})} \tag{6.11}$$

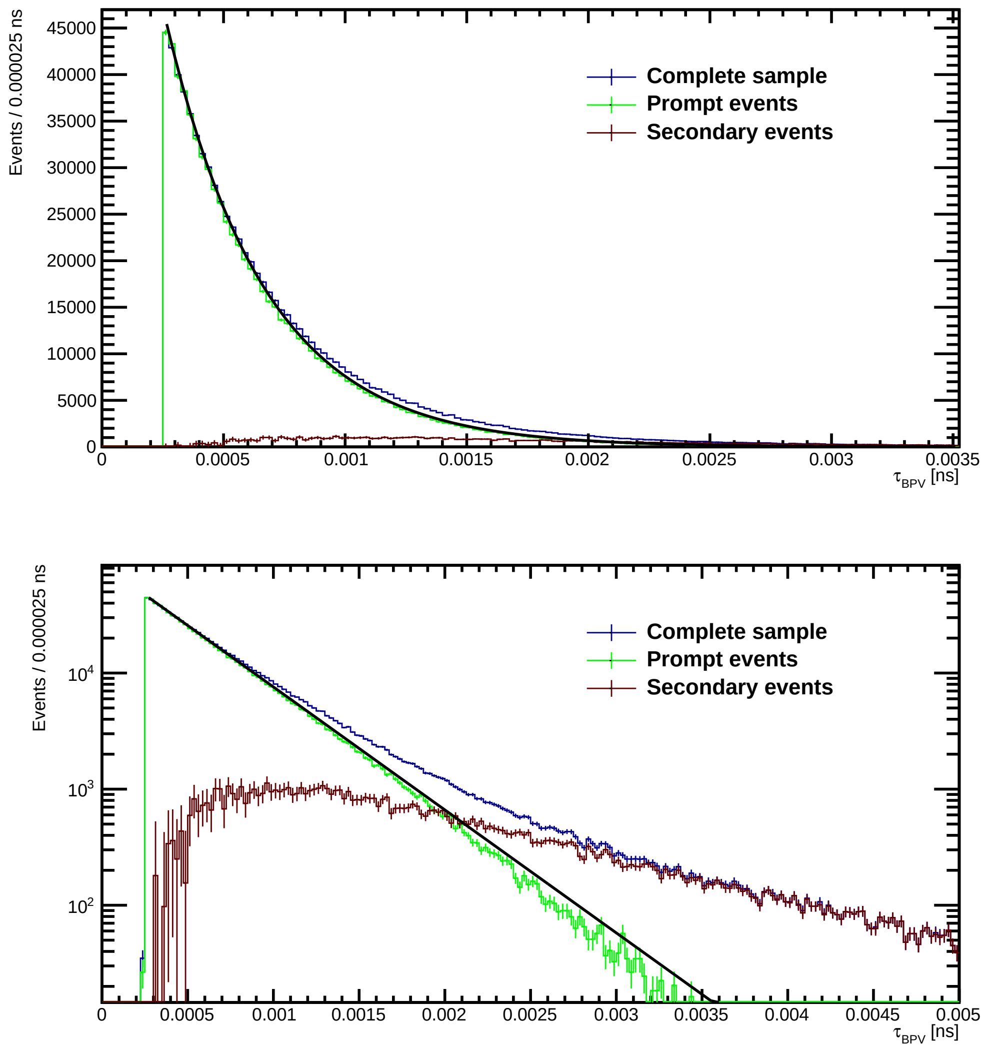

Figure 6.12: τ_{BPV} (D^0) distributions for prompt events, secondary decays and complete sample on the top, the same on logarithmic scale on the bottom. The black line represent an exponential distribution with a mean value equal to the D^0 lifetime. These distributions are extracted from a fraction of the LD-selected sample only, for simplicity. Events with $\Delta m \in [144, 147]\,\mathrm{MeV}/c^2$ are selected.

where primed variables refer to the configuration where the cut is applied and N_{tot} is the total events number in the sample. As can be seen every variable can be connected to known quantities, both measurable, as N'_{tot}, or previously extracted, as N_p.
The f'_s and f_s, together with N'_{tot} are reported in Table 6.7. Therefore the extracted difference between the fraction of secondary decays for a sample with and without the τ_{BPV} (D^0) cut are:

$$(f'_s - f_s)_{LL} = (1.48 \pm 0.34)\% \tag{6.12}$$

$$(f'_s - f_s)_{LD} = (5.9 \pm 0.4)\% \tag{6.13}$$

Now it is possible to determine the values of the searched corrections:

$$\Delta\mathcal{A}^{raw}(K^+K^-)_{LL} = (0.012 \pm 0.005)\% \tag{6.14}$$

Sample	N'_{tot}	f'_s [%]	f_s [%]
LL	$(9468 \pm 3) \times 10^3$	3.3 ± 0.3	1.77 ± 0.16
LD	$(5877.2 \pm 2.4) \times 10^3$	13.7 ± 0.4	7.8 ± 0.2

Table 6.7: Number of events in the sample where the cut is applied, fraction of secondary decays with and without the application of the τ_{BPV} (D^0) cut, for LL and LD control samples.

$$\Delta\mathcal{A}^{raw}(K^+K^-)_{LD} = (0.041 \pm 0.016)\% \tag{6.15}$$

6.2.4 Correction in case of $\Delta\chi^2$ splitting

The extracted values can be exploited to adopt the correct $\mathcal{A}^{raw}$ (K^+K^-) in the $\Delta\chi^2$ method previously discussed. Here in fact the sample is split in two halves, the ones for which the D^* vertex is compatible with the PV and the ones for which is not. It has to be noticed that the two samples are highly asymmetric, in particular the first one contains most of the statistics, in both LL and LD channels. For this subsample, it is possible to apply the already computed corrections, without risking the introduction of any significant bias on $\mathcal{A}^{CP}$ $(K^0_S K^0_S)$, since it is only slightly different from the complete sample, and considering the small value of the computed corrections ($O \sim 10^{-4}$). In the other subsample, where the D^* is not compatible with the PV, it is possible to assume an asymmetry for the $\mathcal{A}^{raw}$ (K^+K^-) sample equal to the one of a sample of pure secondary decays, known thanks to the monotonic fit value at higher χ^2_{IP} (D^*). This again introduces only a really small error on the $\mathcal{A}^{CP}$ $(K^0_S K^0_S)$ determination, since the maximum difference between the $\mathcal{A}^{raw}$ (K^+K^-) real value and the approximated one is, at maximum, a fraction of Δ ($\sim$fraction of percent), and additionally this has a minimum effect in the result, but because of the smallness of the sample at $\Delta\chi^2$ over threshold.

6.2.5 Final kinematics comparison

From this point the selections that has been identified in the previous chapters will not be anymore modified. It is therefore the time to compare the two samples D^* and π_{tag} kinematic distributions, since these will not be influenced by additional cuts. This comparison is crucial for the analysis, since $\mathcal{A}^{prod}$ (D^*) and $\mathcal{A}^{det}$ (π_{tag}) can depend on the events kinematics and the presence of significant discrepancies between signal and control sample can bias the $\mathcal{A}^{CP}$ $(K^0_S K^0_S)$ result, through an imperfect cancellation of production and detection asymmetries in $\Delta\mathcal{A}^{CP}$.
The variables considered to perform this test are p (D^*) and p (π_{tag}), $\eta(D^*)$ and $\eta(\pi_{tag})$ distributions. These are two uncorrelated variables, that describe the events kinematics. To produce these distributions for the signal sample I selected signal events by performing a sideband subtraction procedure, while in the control channel I simply selected the $144 - 147\,\mathrm{MeV}/c^2$ Δm window. For both samples the distributions are normalized to have an integral equal to one, in order to coherently compare them.
p and η distributions for signal and control sample are shown in Figure 6.13 and 6.14. From these plots a slight difference in the distributions emerges, especially for η, showing that the signal sample events have, on average, a larger η. It can be partially due to the difference between $K^0_S K^0_S$ and K^+K^- trigger selections found in 6.1.1. These can in

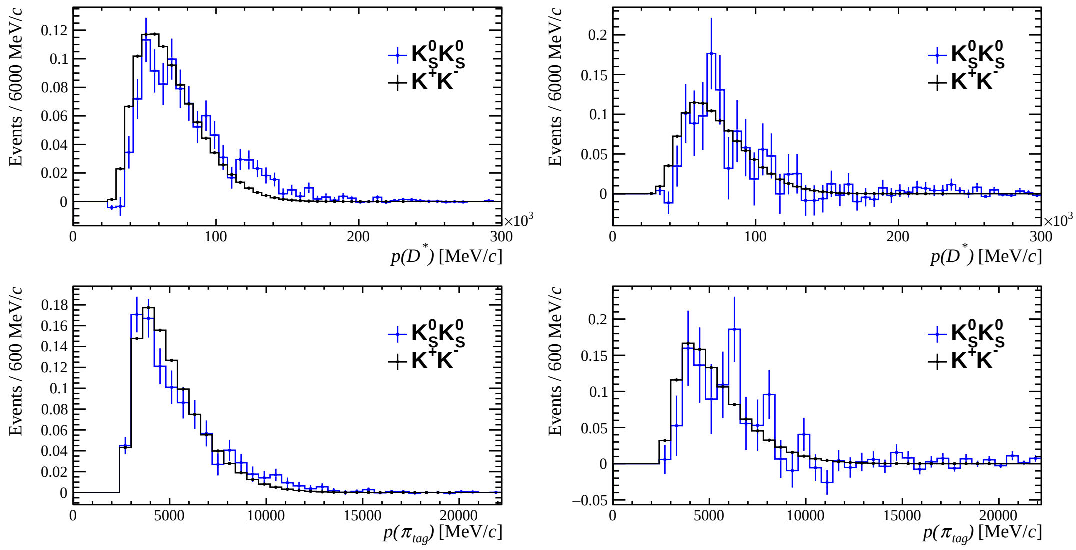

Figure 6.13: D^* (up) and π_{tag} (down) momentum distributions, for LL (left) and LD (right) signal and control channels.

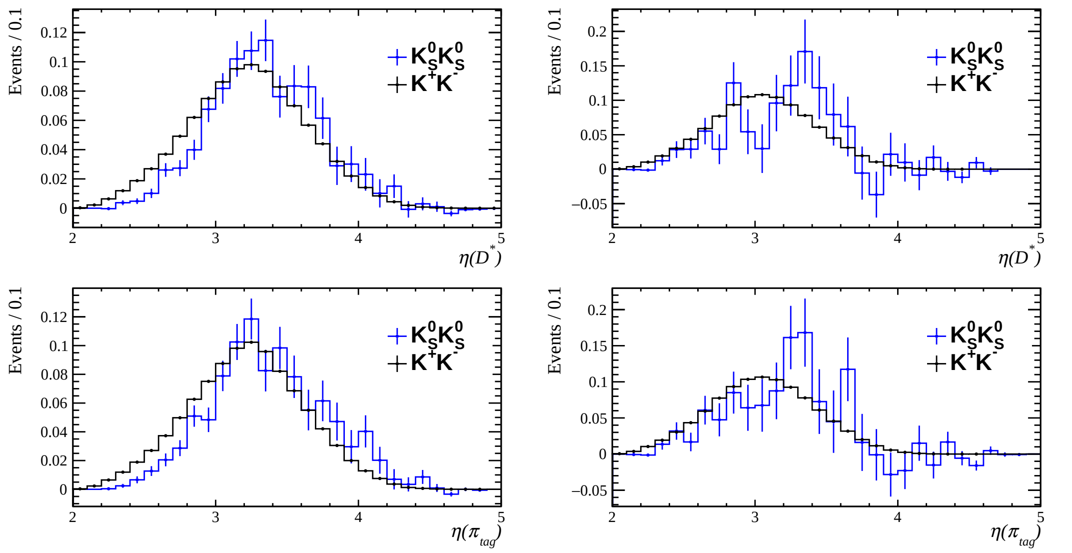

Figure 6.14: D^* (up) and π_{tag} (down) η distributions, for LL (left) and LD (right) signal and control channels.

fact introduce discrepancies in the signal and control sample event kinematics, since they are applied on $K^{\pm}$ transverse momentum. The application of the same cuts on the K^0_Ss present in the signal sample can help to equalize the p and η distributions. I therefore tested the effect of applying two additional cuts to the $K^0_SK^0_S$ signal sample:

- p_T (K^0_S)>800 MeV/c
- $p_{T\ max}(K^0_S)$>1200 MeV/c

The kinematic distributions for signal and control sample, after the application of these cuts, are shown in Figure 6.15 and 6.16. From these plots emerges that it is not the presence of these cuts in control channel that provokes the observed discrepancies, since

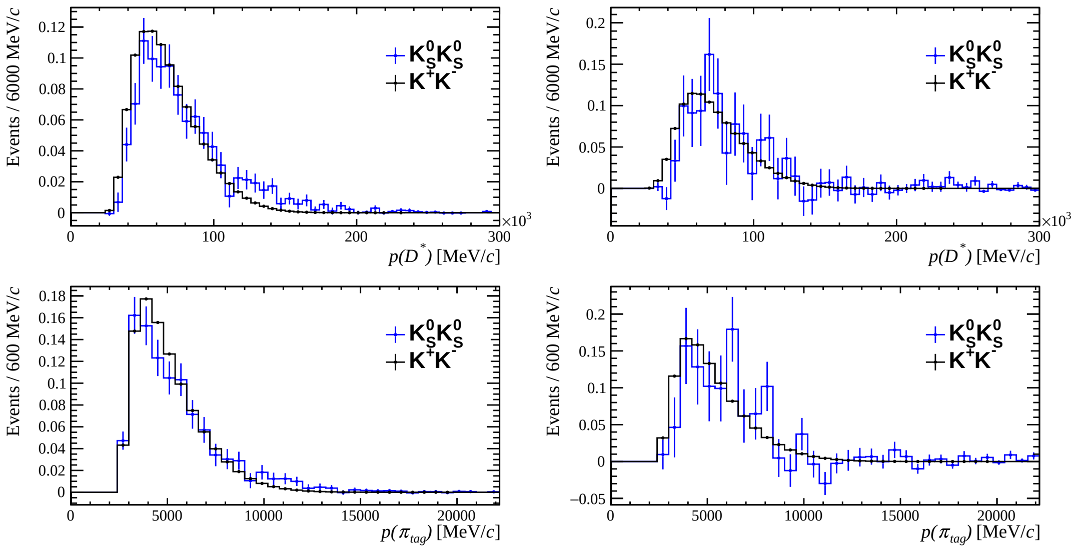

Figure 6.15: D^* (up) and π_{tag} (down) momentum distributions, for LL (left) and LD (right) signal and control channels.

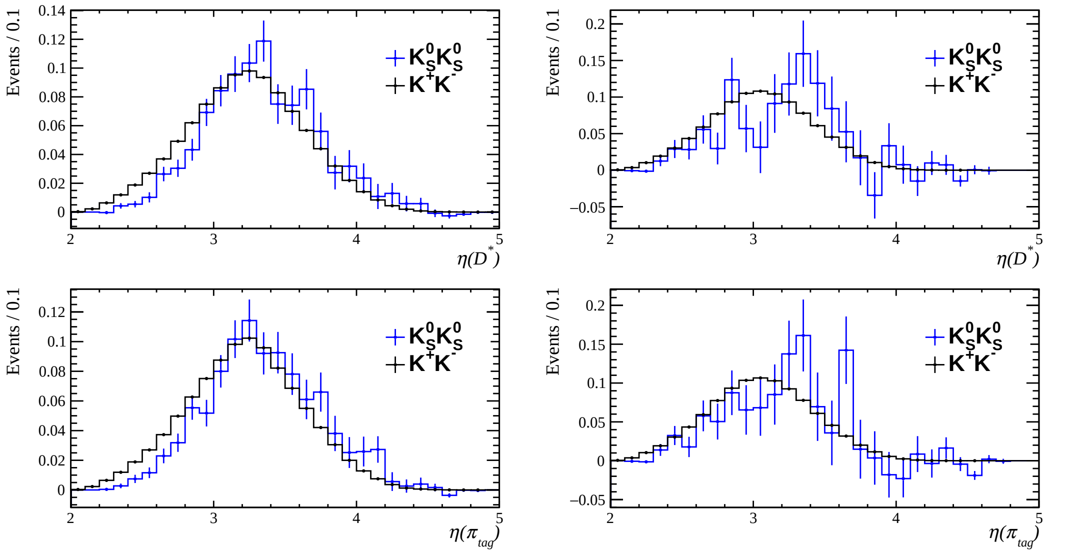

Figure 6.16: D^* (up) and π_{tag} (down) η distributions, for LL (left) and LD (right) signal and control channels.

these are still present after the cuts equalization. Seen that, I preferred to do not apply the p_{T} cuts to the signal sample, to do not further reduce its size. Therefore, the distributions that will be considered are the one present in Figure 6.13 and 6.14.
Seen that, it is possible to assume that the present discrepancies can be caused by another effect, in particular by the different detector acceptance for $K^0_S K^0_S$ and K^+K^- final states. This can happen because the four pions present in the $K^0_S K^0_S$ final state are contained in a cone that is, on average, larger than the one occupied by the K^+K^- events. Therefore, to be detected with the same acceptance, signal events have to have a larger η, and this corresponds to the observed effect.
The correction of these effects is not trivial and therefore I analyzed the $\mathcal{A}^{raw}$ variation as a function of π_{tag} momentum and η, before applying any additional procedure necessary

to equalize kinematics distributions, as for example a re-wighting procedure. I studied the $\mathcal{A}^{raw}$ variation for the K^+K^- sample only; this because, in case of the application of any correction, this will be done on the control channel, that has high statistics and where the resolution will not be significantly affected. The analysis of the $\mathcal{A}^{raw}$ variation is done for the π_{tag} variables only, since its detection asymmetry is the one that mostly influences the $\mathcal{A}^{raw}$ value and depends on its kinematics.
I divided the p and η distributions in bins, and extracted the $\mathcal{A}^{raw}$ in each one; results are shown in Table 6.8 and 6.9 and in Figure 6.17 and 6.18. The compatibility and the

p (π_{tag}) [GeV/c]	$\mathcal{A}^{raw}$ (K^+K^-) [%]	n_{sig}
0-3.5	-0.93 $\pm$ 0.16	$1.229 \cdot 10^6$
3.5-5	-0.69 $\pm$ 0.08	$3.376 \cdot 10^6$
5-6.5	-0.9 $\pm$ 0.1	$2.111 \cdot 10^6$
6.5-8	-0.7 $\pm$ 0.1	$1.037 \cdot 10^6$
>8	-0.96 $\pm$ 0.16	$0.639 \cdot 10^6$

$\eta(\pi_{tag})$	$\mathcal{A}^{raw}$ (K^+K^-) [%]	n_{sig}
2-2.6	-0.8 $\pm$ 0.1	$0.632 \cdot 10^6$
2.6-3.2	-0.71 $\pm$ 0.07	$3.091 \cdot 10^6$
3.2-3.8	-0.81 $\pm$ 0.08	$1.839 \cdot 10^6$
3.8-5	-0.9 $\pm$ 0.2	$0.318 \cdot 10^6$

Table 6.8: $\mathcal{A}^{raw}$ values as extracted for different p (π_{tag}) and $\eta(\pi_{tag})$ bins, for the LL control sample. n_{sig} is the number of signal events present in that bin.

p (π_{tag}) [GeV/c]	$\mathcal{A}^{raw}$ (K^+K^-) [%]	n_{sig}
0-3.5	-1.0 $\pm$ 0.2	$0.663 \cdot 10^6$
3.5-5	-0.75 $\pm$ 0.09	$2.221 \cdot 10^6$
5-6.5	-0.8 $\pm$ 0.1	$1.505 \cdot 10^6$
6.5-8	-0.6 $\pm$ 0.1	$0.769 \cdot 10^6$
>8	-0.9 $\pm$ 0.2	$0.518 \cdot 10^6$

$\eta(\pi_{tag})$	$\mathcal{A}^{raw}$ (K^+K^-) [%]	n_{sig}
2-2.6	-0.8 $\pm$ 0.1	$0.632 \cdot 10^6$
2.6-3.2	-0.73 $\pm$ 0.07	$3.091 \cdot 10^6$
3.2-3.8	-0.9 $\pm$ 0.1	$1.839 \cdot 10^6$
3.8-5	-1.5 $\pm$ 0.4	$0.115 \cdot 10^6$

Table 6.9: $\mathcal{A}^{raw}$ values as extracted for different p (π_{tag}) and $\eta(\pi_{tag})$ bins, for the LD control sample. n_{sig} is the number of signal events present in that bin.

low variation of the shown values demonstrates how the asymmetry does not significantly depends on the π_{tag} kinematic variables. This implicates that the application of any other procedure necessary to equalize the kinematic distributions will have an effect smaller than the statistic uncertainty, and it will therefore not applied to the sample.

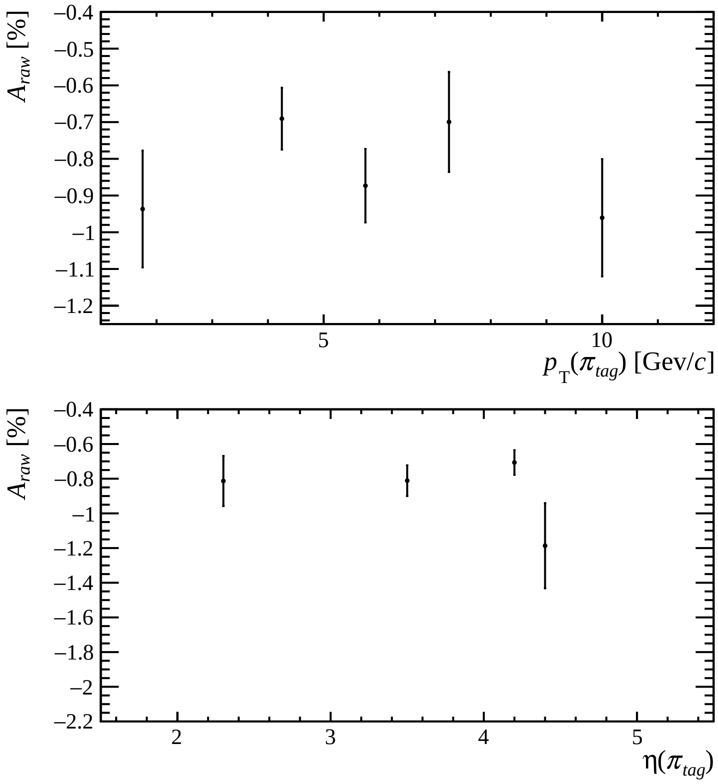

Figure 6.17: $\mathcal{A}^{raw}$ value in each p_{T} and η π_{tag} bin, for the LL control sample.

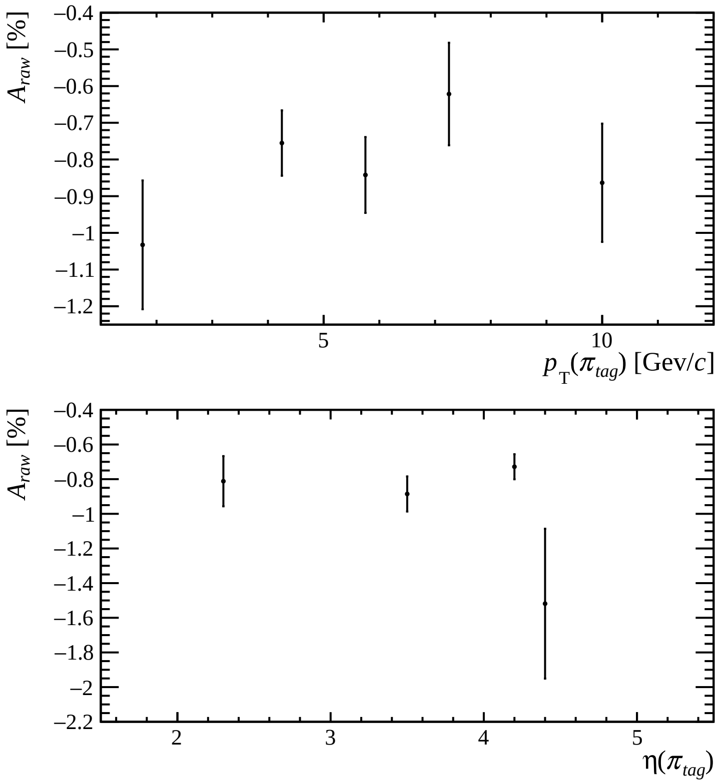

Figure 6.18: $\mathcal{A}^{raw}$ value in each p_{T} and η π_{tag} bin, for the LD control sample.

Chapter 7

Results and conclusions

In this chapter I extract the $\mathcal{A}^{CP}$ $(K^0_S K^0_S)$ *and* $\mathcal{A}^{CP}$ (K^+K^-) *results, understanding the resolution that can be achieved with the developed analysis approach. This is done through a separate fit for events tagged with opposite-sign pions.*

After identification of the selections and equalization of trigger cuts, discussed in the previous chapter, it is possible to perform the measurement of $\mathcal{A}^{CP}$ $(K^0_S K^0_S)$.
The fit is done here dividing each sample in two sub-samples, depending on the π_{tag} sign, and fitting the Δm distributions to extract $\mathcal{A}^{raw}$. This is done separately for the LL and LD channels, and also the results are then combined. The fit is also performed on the corresponding control samples. Extracting *CP* raw asymmetry in both, it is possible to compute $\Delta\mathcal{A}^{CP}$ and extrapolate the $\mathcal{A}^{CP}$ $(K^0_S K^0_S)$.

7.1 Fit model

In this analysis step I decided, for signal events fit, to employ a different fit strategy from the one already adopted in the previous chapter for the control channel to measure $\mathcal{A}^{raw}$. Instead of separately extracting the yields, from the opposite sign-tagged events, and than compute the $\mathcal{A}^{raw}$ value, I simultaneously fit the two Δm distributions, using a likelihood function parametrized in terms of $\mathcal{A}^{CP}$ and N_{exp}:

$$\mathcal{L} = \frac{e^{-N_{exp}}}{N_{obs}} \prod_{i=1} \left[n_{sig} \frac{1 + q_i \mathcal{A}^{CP}{}_{sig}}{2} f^{q_i}_{sig}(x) + n_{bkg} \frac{1 + q_i \mathcal{A}^{CP}{}_{bkg}}{2} f^{q_i}_{bkg}(x) \right] \tag{7.1}$$

where $\mathcal{A}^{CP}{}_{sig}$ and $\mathcal{A}^{CP}{}_{bkg}$ are free parameters and correspond here to the raw asymmetries, q_i is the charge of the pion in the event (in electron charge units), and the adopted *p.d.f.*s are:

$$f_{sig}(x) \propto \frac{1}{\sqrt{2\pi\sigma^2}} \exp\left\{ \frac{(x-\mu)^2}{2\sigma^2} \right\} \tag{7.2}$$

and:

$$f_{bkg}(x) \propto \sqrt{x - m_\pi}[1 + a \cdot (x - m_\pi) + b \cdot (x - m_\pi)^2] \tag{7.3}$$

Doing this, allows me to force signal and background shape to be the same for the two opposite sign-tagged samples, allowing only the presence of a difference between the number of events, represented by $\mathcal{A}^{CP}{}_{sig}$ and $\mathcal{A}^{CP}{}_{bkg}$. This is reasonable, since no difference is expected in the signal and background shapes. This strategy leads to improved resolution on $\mathcal{A}^{raw}$, as it decreases the systematic effect, due to the variability of the fit on the opposite sign-tagged events, that can appear in case of low statistics. The variables used in this part of the analysis are the ones obtained from the use of the DTF, where the K_S^0 mass constrain is applied, helping in the resolution improvement. For the control channel sample I adopted the same method reported in 6.1.4, for simplicity, since the resolution on $\mathcal{A}^{raw}$ (K^+K^-) does not need to be improved anymore for the analysis purposes.

7.1.1 $D^0 \to K_S^0 K_S^0$ blind result

For the $D^0 \to K_S^0 K_S^0$ sample we made sure not to learn about the $\mathcal{A}^{CP}$ result, until the analysis reached its final configuration and it will not be anymore modified. This reflects on the necessity to maintain unknown the $\mathcal{A}^{raw}$ $(K_S^0 K_S^0)$ value, since from this, when the $\mathcal{A}^{raw}$ (K^+K^-) will be measured, it will be possible to determine $\mathcal{A}^{CP}$ $(K_S^0 K_S^0)$. This type of *blinding* strategy is often applied in order to avoid any bias that, on purpose or not, the experimenter can might impose on fit result. The blinding is here done by adding to the fitted $\mathcal{A}^{raw}$ value an unknown random number, extracted from a pseudorandom generator. This procedure is not necessary for the $D^0 \to K^+K^-$ sample, since $\mathcal{A}^{CP}$ (K^+K^-) is not the target of the analysis and only the $\mathcal{A}^{raw}$ (K^+K^-) will be shown, and no information are provided to extract the $\mathcal{A}^{CP}$ (K^+K^-) value. To keep the result blind, it will not be possible to show the Δm distributions and the related fits, since, from these, it is possible to infer the $\mathcal{A}^{raw}$ $(K_S^0 K_S^0)$ value. To understand if the fits performed on signal sample reached convergence and how they describes data I extrapolate and show the pull distributions, for both subsamples. These distributions, in reality, could in principle allow anyway to determine $\mathcal{A}^{raw}$ $(K_S^0 K_S^0)$, since signal and background shapes are known; but I decided to show pulls distributions because unblind the result with these is not immediate as can happen for the Δm distributions.

7.1.2 Signal sample

The first considered sample is the signal, extracting the $\mathcal{A}^{raw}$ values for LL and LD channels with the discussed fit strategy. Doing this, I introduced a difference between the fits performed on the two channels. In fitting LD sample distributions I decrease the number of free parameters; this because of the small statistics of that sample, that when divided in two different subsamples (for opposite charges), can cause large statistical fluctuations. These can influence the $\mathcal{A}^{raw}$ resolution, not only because of larger the statistical uncertainty, but because of the systematic one, too, due to the uncertainty on the fit model. Therefore, in the fit to the LD channel distributions, I fix the signal shape parameters, hence the mean and standard deviation of the Gaussian *p.d.f.*, to the values extracted from the fit performed on the complete sample, shown in Figure 5.18. This does not bias the result, since I do not expect any difference between mass resolutions in opposite charge-tagged events.
The same procedure is not necessary for the LL channel sample, because of the higher statistics.
Parameters extracted from fits to LL and LD channels are shown in Table 7.1 and the pull distributions for the relative fits in Figure 7.1 and 7.2. No discrepancy emerges from the comparison between these parameters and the one extracted through the fit to the

	LL channel	LD channel
n_{sig}	1348 ± 77	373 ± 47
n_{bkg}	10995 ± 125	7413 ± 96
μ [MeV/c^2]	145.40 ± 0.03	145.45
σ [MeV/c^2]	0.593 ± 0.035	0.66
a [(MeV/c)$^{-1}$]	(-1 ± 1)·10^{-2}	(-3 ± 1)·10^{-2}
b [(MeV/c)$^{-2}$]	(-0.6 ± 6.7)·10^{-4}	(1.0 ± 0.7)·10^{-4}

Table 7.1: Summary of parameters obtained from the fits to LL and LD channels, for $D^0 \rightarrow K^0_S K^0_S$ sample. μ and σ for the LD channel are fixed and not extracted from the fit.

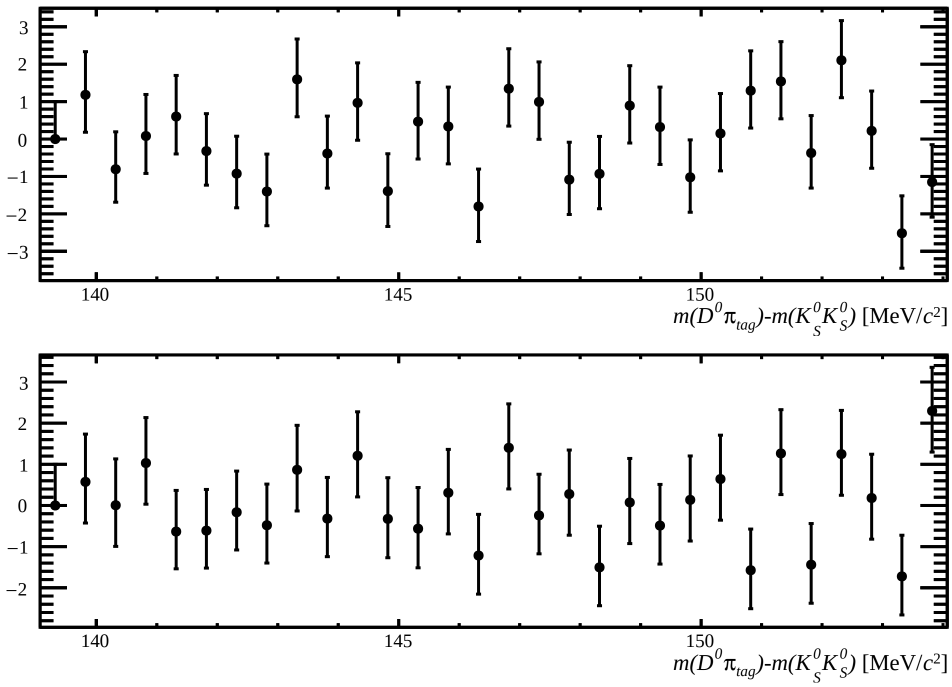

Figure 7.1: Positive (up) and negative (down) tagged events pull distributions, obtained from the signal events histogram and the *p.d.f.* functions extracted from the fit, for LL channel.

complete sample, shown in Figure 5.18. This comparison, together with the shown pull distributions suggest that the fit converged to a valid result.
The $\mathcal{A}^{raw}$ $(K^0_S K^0_S)$ blind results, extracted from the fits are:

$$\mathcal{A}^{raw}(K^0_S K^0_S)_{LL} = (50.6 \pm 4.3)\% \tag{7.4}$$

$$\mathcal{A}^{raw}(K^0_S K^0_S)_{LD} = (77.4 \pm 11.8)\% \tag{7.5}$$

7.1.3 Control channel

The same procedure is repeated for the control channels. The parameters extracted from the fit to the LL and LD control samples are summarized in Table 7.2. The Δm histograms and the relative fits are shown in Figure 7.3 and 7.4. The $\mathcal{A}^{raw}$ (K^+K^-) values, extracted from the fits are:

$$\mathcal{A}^{raw}(K^+K^-)'_{LL} = (-0.79 \pm 0.05)\% \tag{7.6}$$

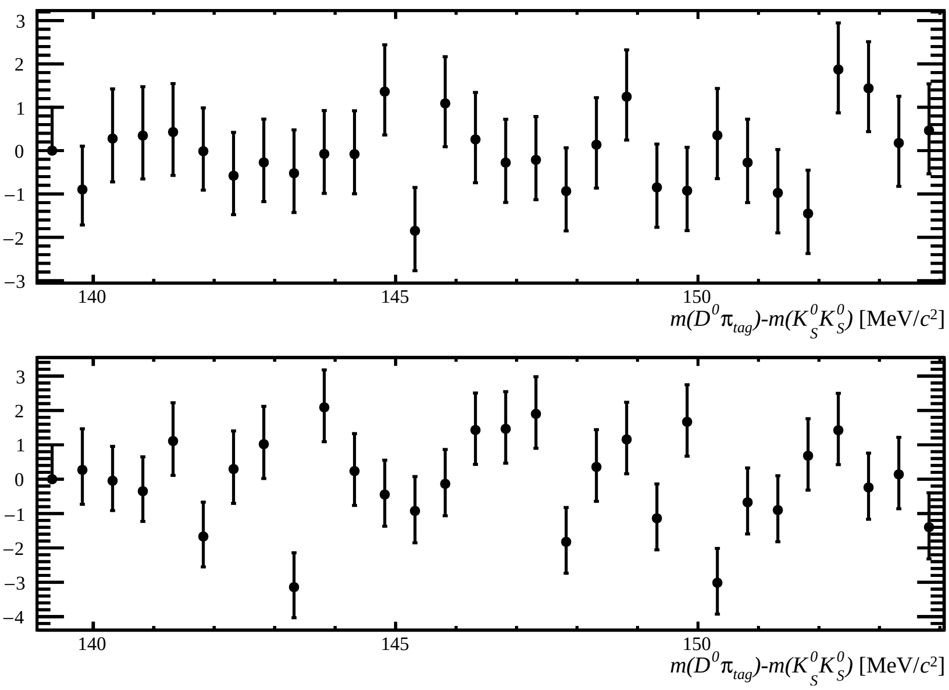

Figure 7.2: Positive (up) and negative (down) tagged events pull distributions, obtained from the signal events histogram and the *p.d.f.* functions extracted from the fit, for LD channel.

	LL channel	LD channel
n_{sig}	(8394 ± 4)·10^3	(5677 ± 3)·10^3
n_{bkg}	(7960 ± 3)·10^3	(2486 ± 2)·10^3
a [(MeV/c)$^{-1}$]	(1.8 ± 0.1)·10^{-2}	(-0.99 ± 0.15)·10^{-2}
b [(MeV/c)$^{-2}$]	(-10.0 ± 0.7)·10^{-4}	(-5 ± 1)·10^{-4}

Table 7.2: Summary of parameters obtained from the fits to LL and LD control samples.

$$\mathcal{A}^{raw}(K^+K^-)'_{LD} = (-0.80 \pm 0.05)\% \tag{7.7}$$

I adopted here the same notation used in 6.2.3, where the primed variables are referred to the sample where the effect of the τ_{BPV} (D^0) cut is present, and have to be corrected.

7.1.4 $\mathcal{A}^{raw}$ (K^+K^-) correction

The extracted $\mathcal{A}^{raw}$ $'(K^+K^-)$ values are not the ones that will be used in the $\Delta\mathcal{A}^{CP}$ calculation. In fact, as explained in 6.2.3, these have to be corrected with the computed parameters through (6.4). The $\mathcal{A}^{raw}$ (K^+K^-) values turn out as:

$$\mathcal{A}^{raw}(K^+K^-)_{LL} = (-0.80 \pm 0.05)\% \tag{7.8}$$

$$\mathcal{A}^{raw}(K^+K^-)_{LD} = (-0.84 \pm 0.05)\% \tag{7.9}$$

7.1.5 $\mathcal{A}^{CP}$ $(K^0_S K^0_S)$ extraction

With the $\mathcal{A}^{raw}$ extraction for both signal and control sample, it is finally possible to compute the $\mathcal{A}^{CP}$ $(K^0_S K^0_S)$ value. This is done through two subsequent steps. In the first

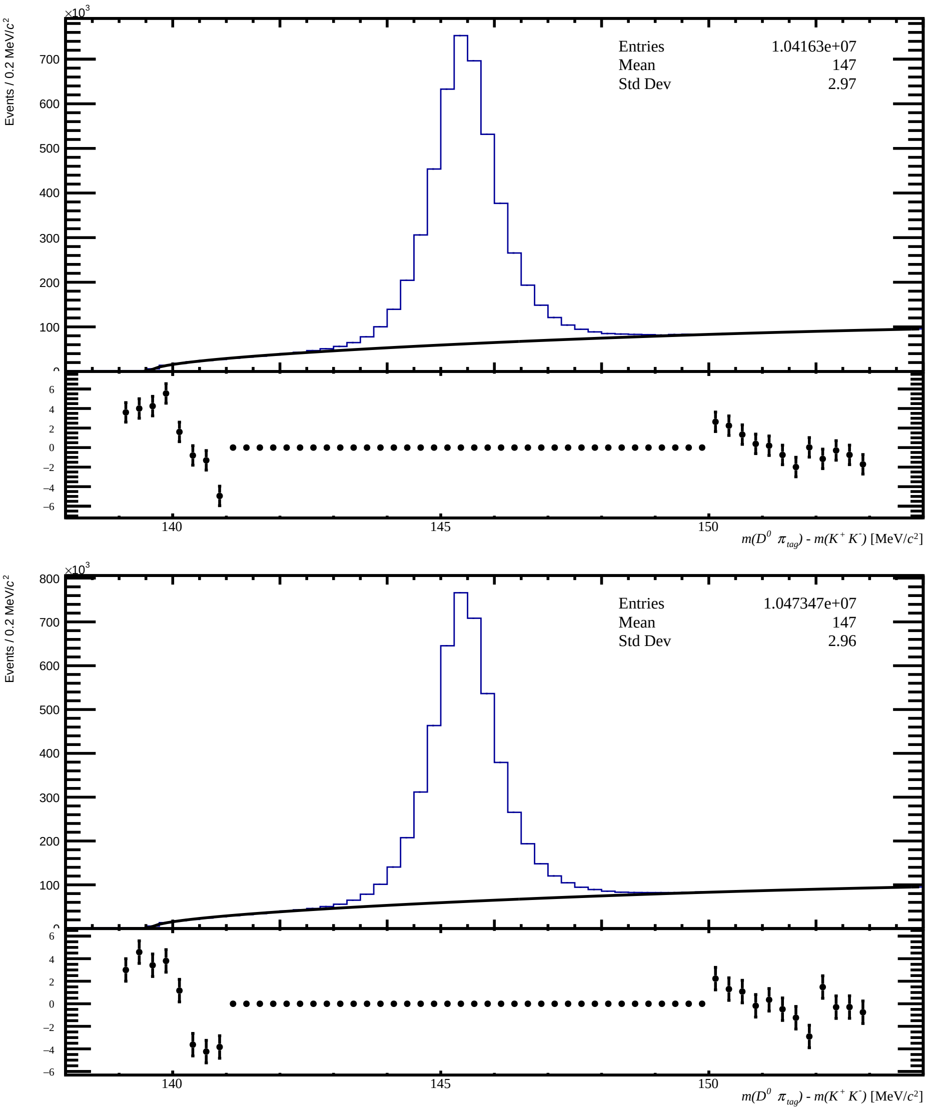

Figure 7.3: Positive (up) and negative (down) tagged events Δm distributions, with the relative fit, for the LL control channel.

$\Delta\mathcal{A}^{CP}$ is extracted from the difference between the measured $\mathcal{A}^{raw}$ $(K^0_S K^0_S)$ and $\mathcal{A}^{raw}$ (K^+K^-).
After this the world-average value for $\mathcal{A}^{CP}(K^+K^-)(= (0.04 \pm 0.12\ (\text{stat.}) \pm 0.10\ (\text{syst.}))\%)$ is added to the computed $\Delta\mathcal{A}^{CP}$ value, to determine $\mathcal{A}^{CP}$ $(K^0_S K^0_S)$.
Doing this separately for both LL and LD channels, the obtained $\mathcal{A}^{CP}$ $(K^0_S K^0_S)$ results are:

$$\mathcal{A}^{CP}(K^0_S K^0_S)_{LL} = (xx \pm 4.3\ (\text{stat.}) \pm 0.05\ (\text{syst.}) \pm 0.16\ (\text{syst.}))\% \tag{7.10}$$

$$\mathcal{A}^{CP}(K^0_S K^0_S)_{LD} = (xx \pm 11.8\ (\text{stat.}) \pm 0.05\ (\text{syst.}) \pm 0.16\ (\text{syst.}))\% \tag{7.11}$$

where the $\mathcal{A}^{CP}$ $(K^0_S K^0_S)$ central value it kept blind, the first uncertainty is statistical, the second is the systematic given by the statistical uncertainty on the $\mathcal{A}^{raw}$ (K^+K^-) measurement and the third is the systematic given by the uncertainty on the $\mathcal{A}^{CP}$ (K^+K^-) world average. The overall systematic effect here quoted is dominated by the second considered effect. Now it is possible to combine the two results, extracting the final $\mathcal{A}^{CP}$

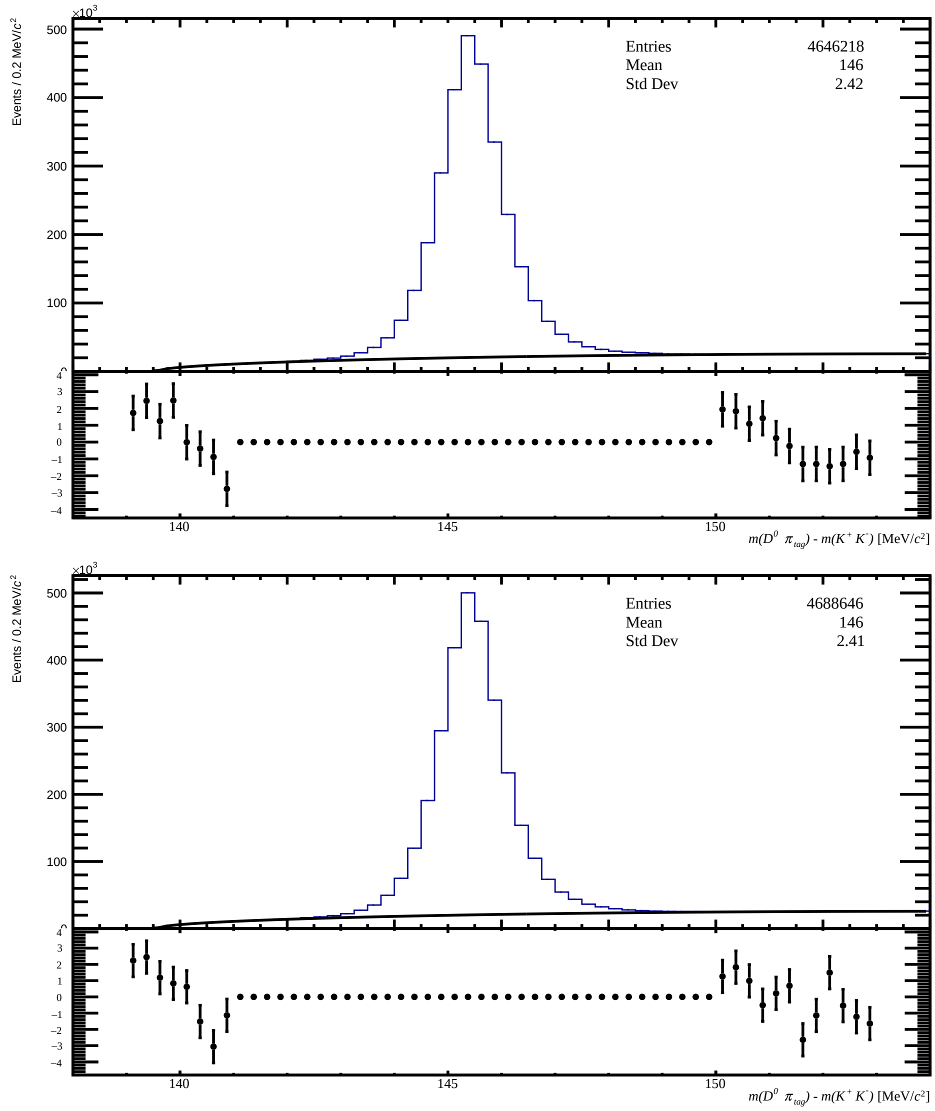

Figure 7.4: Positive (up) and negative (down) tagged events Δm distributions, with the relative fit, for the LD control channel.

$(K^0_S K^0_S)$ measurement. In computing the $\mathcal{A}^{CP}$ $(K^0_S K^0_S)$ uncertainty I considered the statistical uncertainties as completely uncorrelated, since are extracted from two different samples. On the other hand, I consider the systematic uncertainty as completely correlated; this is assumed because these are given by the $\mathcal{A}^{raw}$ (K^+K^-) for LL and LD channels, that are extracted from the same sample, and by the exploiting of the same $\mathcal{A}^{CP}$ (K^+K^-) measurement.
The overall statistical sensitivity on the combined $\mathcal{A}^{CP}$ $(K^0_S K^0_S)$ result is:

$$\sigma(\mathcal{A}^{CP}) = \sqrt{\frac{1}{\sigma(\mathcal{A}^{CP}{}_{LL})^2} + \frac{1}{\sigma(\mathcal{A}^{CP}{}_{LD})^2}} \tag{7.12}$$

while, the systematic one is the same quoted in the results of the two channels.
Therefore, the overall result that can be achieved on the $\mathcal{A}^{CP}$ $(K^0_S K^0_S)$, with the application of our newly developed analysis is:

$$\mathcal{A}^{CP}(K^0_S K^0_S) = (xx \pm 4.0 \text{ (stat.)} \pm 0.16 \text{ (syst.)})\% \tag{7.13}$$

where I merged the two systematic effects.

7.1.6 Comparison with the 2015-16 analysis

It is interesting to make a comparison between the result that can be obtained with the novel analysis approach, and the one obtained by the past $\mathcal{A}^{CP}$ $(K^0_S K^0_S)$ measurement performed by LHCb, on 2015-16 sample. To make a coherent comparison, I will consider the results obtained in 2015-16 analysis, applying only rectangular cuts, shown in [39]. The resolution achieved in this way, and without the application of the PV constrain, is equal to 4.6% and 11.3% for the LL and LD channel, respectively. The overall result, given by the combination of these, corresponds to:

$$\sigma(\mathcal{A}^{CP})_{2015-16} = 4.3\% \tag{7.14}$$

This resolution has been achieved exploiting a sample of $1.98\,\mathrm{fb}^{-1}$. The result that will be achieved applying the novel analysis to a sample of equal size of the 2015-2016 one is:

$$\sigma(\mathcal{A}^{CP}) = \frac{\sigma(\mathcal{A}^{CP})_{2017}}{\sqrt{1.98/1.7}} = 3.7\% \tag{7.15}$$

The comparison between these resolutions shows that, the analysis here set up allows to achieve a better statistical sensitivity, being the sample size equal. The result here achieved is partially due to the changes introduced in the trigger in 2017, but it demonstrates anyway that it is possible to perform an analysis without applying any cut on variables related to the vertex reconstruction, and therefore including secondary decays in the sample, and that this new approach lead to a resolution that is comparable to the achieved with the usual analysis strategy. In this comparison I am not considering the systematic uncertainty, because the overall uncertainty was dominated by the statistical one in the most recent LHCb measurement, and it can be assumed that the situation will remain the same in our analysis.

7.1.7 Further improvement

The achieved result does not represent the absolute best resolution that can be achieved with the current analysis approach. The first method that can be exploited to improve the result is the one discussed in 5.4.1. For simplicity it will not be directly applied here, but it is possible to give an estimate about the resolution improvement that it allows to achieve, looking at the results shown in 5.4.1. The sample division based on the $\Delta\chi^2$ value allowed to improve the resolution from 5% (14.2%) to 3.5% (8.7%) for the LL (LD) channel, considering results extracted from the charge integrated fits. Therefore the overall resolution has improved by $\sim$ 30%, going from 4.7% to 3.2%. Assuming a similar trend for resolution extracted from separate charge fits performed in this chapter, the adoption of the considered method should allow to obtain a significant improvement for the resolution, going from the 4% shown in (7.13), to a value $\sim$ 2.8%.
Another step that can be thought of is the application of a cut on the output of a multivariate classifier, trained on signal and background events, eventually exploiting a Monte Carlo sample for the former. This should allow to further improve the $\mathcal{A}^{CP}$ $(K^0_S K^0_S)$ statistical sensitivity with respect to the one obtained with the selection identified in 5. The

improvement that can be achieved can be estimated from [39]. There, the application of a similar method allowed to improve the resolution of $\sim 7\%$ ($\sim 1\%$), going from a value of 4.4% (8.3%) to a value of 4.1% (8.2%) for the LL (LD) channel. The overall resolution has therefore decreased by 5%, going from a value of 3.9% to 3.7%. Assuming a similar effect on the selection here identified, after the application of the $\Delta\chi^2$ splitting method, the statistical sensitivity that can be achieved with the application of the method here identified goes from 2.8% to 2.7%, that is the best achievable result with the current analysis method.
I expect that the systematic uncertainty affecting this improved result will be the equal to the one quoted in 7.13, since it is dominated by the uncertainty on the $\mathcal{A}^{CP}$ (K^+K^-) measurement, that will be in the same way exploited. It will be therefore a small correction with respect to the overall resolution, given principally by the statistic uncertainty.

7.2 Conclusions and prospects

The analysis method developed in this work, together with the further improvement that can still be applied, can be directly extended to 2018 data, as this sample was collected with the same trigger algorithm adopted in 2017 data-taking, and no difference is expected between the two samples. The integrated luminosity collected during 2018 corresponds to $2.2\,\mathrm{fb}^{-1}$, that added to the 2017 sample ($1.7\,\mathrm{fb}^{-1}$) gives a total amount of data of $3.9\,\mathrm{fb}^{-1}$. It is therefore possible to extrapolate the result to the overall $3.9\,\mathrm{fb}^{-1}$ sample:

$$\sigma(\mathcal{A}^{CP})_{2017-18} = \frac{\sigma(\mathcal{A}^{CP})_{2017}}{\sqrt{3.9/1.7}} = \frac{2.7\%}{\sqrt{3.9/1.7}} = 1.8\% \tag{7.16}$$

Here, as explained before, I expect that the systematic uncertainty will remain of the same order of magnitude, not significantly influencing the overall result.
This result can be combined with the one obtained in [40], where combining the result of the analyses performed on Run-1 and first two years of Run-2, the achieved resolution (given by both statistical and systematic uncertainty) corresponds to $\sigma(\mathcal{A}^{CP}) = 2.9\%$. From this value and the results determined in (7.16), the overall LHCb result on $\mathcal{A}^{CP}$ $(K^0_S K^0_S)$ measurement is expected to have a resolution:

$$\sigma(\mathcal{A}^{CP})_{Run-1/2} = 1.5\% \tag{7.17}$$

This is the same as the best existing single measurement, obtained by Belle in [25], and therefore can significantly contribute to the world average. However, the final world average would still not be very likely to show a non-zero effect in this channel, and it is worth asking whether LHCb can contribute any further to this important measurement.
LHC will start a new data-taking period in 2021, called Run-3. During this period, LHCb is expected to collect an overall integrated luminosity of about $25\,\mathrm{fb}^{-1}$. Before Run-3 starts, LHCb will undergo several major changes, for both detector and trigger, significantly modifying the experiment trigger structure, removing the L0 step and performing a 30 MHz event reconstruction [15]. This allows implementation of more sophisticated algorithms already at the first level of triggering, but significantly decreases the available processing time for each detected event. This can be counterproductive in case of K^0_S, since their reconstruction is highly computing demanding and the K^0_S detection efficiency can be significantly reduced. But there is another investigated possibility, that aims to

perform triggering exploiting only Downstream tracks [33]. This would have the opposite effect on the K^0_S detection, making possible an increase of efficiency for the collection of K^0_S decaying after the vertex detector (LD and DD events in our analysis). These possibilities are still under study and at the present time it is difficult to predict the K^0_S detection efficiency that will be available. A rough prediction for the statistical sensitivity that can be achieved exploiting data collected during next LHC run can be made on the basis of the nominal expectations in the proposal [15] with an expected increase in hadron decays LHCb detection efficiency by a factor ~ 2. Assuming these conditions, and simply extending the performed analysis to the full Run-3 statistics, one can expect a result with a precision of the order of:

$$\sigma(\mathcal{A}^{CP})_{Run-3} = \frac{\sigma(\mathcal{A}^{CP})}{\sqrt{2 \cdot 25/1.7}} = \frac{2.7\%}{\sqrt{2 \cdot 25/1.7}} = 0.5\% \tag{7.18}$$

This result enters an interesting sensitivity range. Clearly, an improvement in the sensitivity of the currently least exploited part of the sample (Downstream K^0_S) could be very important in the future. In this work I have tried at least to show that the LD sample can be effectively used in the measurement, keeping systematic uncertainty under control in spite of the limited capability of discriminating secondary decays. This could provide some encouragement to the current efforts specifically aimed at increasing the trigger efficiency for this type of events in future runs.

Bibliography

[1] LHCb VELO TDR: Vertex locator. Technical design report. 2001.

[2] Search for time-dependent CP violation in $D^0 \to K^+K^-$ and $D^0 \to \pi^+\pi^-$ decays . Technical Report LHCb-CONF-2019-001. CERN-LHCb-CONF-2019-001, CERN, Geneva, May 2019.

[3] LHCb: Outer tracker technical design report. 2001.

[4] R. Aaij et al. LHCb Detector Performance. *Int. J. Mod. Phys.*, A30(07):1530022, 2015.

[5] R. Aaij et al. Measurement of the time-integrated CP asymmetry in $D^0 \to K^0_S K^0_S$ decays. *JHEP*, 10:055, 2015.

[6] R. Aaij et al. Measurement of B^0, B^0_s, B^+ and Λ^0_b production asymmetries in 7 and 8 TeV proton-proton collisions. *Phys. Lett.*, B774:139–158, 2017.

[7] R. Aaij et al. Measurement of CP asymmetry in $D^0 \to K^-K^+$ decays. *Phys. Lett.*, B767:177–187, 2017.

[8] R. Aaij et al. Measurement of the CP violation parameter A_Γ in $D^0 \to K^+K^-$ and $D^0 \to \pi^+\pi^-$ decays. *Phys. Rev. Lett.*, 118(26):261803, 2017.

[9] R. Aaij et al. Observation of CP Violation in Charm Decays. *Phys. Rev. Lett.*, 122(21):211803, 2019.

[10] M. Adinolfi et al. Performance of the LHCb RICH detector at the LHC. *Eur. Phys. J.*, C73:2431, 2013.

[11] A. A. Alves et al. Performance of the LHCb muon system. *Journal of Instrumentation*, 8(02):P02022–P02022, feb 2013.

[12] A. A. Alves, Jr. et al. The LHCb Detector at the LHC. *JINST*, 3:S08005, 2008.

[13] I. M. and. Current status and performance of the LHCb electromagnetic and hadron calorimeters. *Journal of Physics: Conference Series*, 293:012052, apr 2011.

[14] R. Arink et al. Performance of the LHCb Outer Tracker. *JINST*, 9(01):P01002, 2014.

[15] I. Bediaga et al. Framework TDR for the LHCb Upgrade: Technical Design Report. (CERN-LHCC-2012-007. LHCb-TDR-12), Apr 2012.

[16] R. Bernhard. The lhcb silicon tracker. *Nuclear Instruments and Methods in Physics Research Section A: Accelerators, Spectrometers, Detectors and Associated Equipment*, 596(1):17 – 20, 2008. Proceedings of the 8th International Conference on Large Scale Applications and Radiation Hardness of Semiconductor Detectors.

[17] S. Bianco, F. L. Fabbri, D. Benson, and I. Bigi. A Cicerone for the physics of charm. *Riv. Nuovo Cim.*, 26N7:1–200, 2003.

[18] G. Bonvicini et al. Search for CP violation in $D^0 \to K^0_S\pi^0$ and $D^0 \to \pi^0\pi^0$ and $D^0 \to K^0_S K^0_S$ decays. *Phys. Rev.*, D63:071101, 2001.

[19] J. Brod, A. L. Kagan, and J. Zupan. Size of direct CP violation in singly Cabibbo-suppressed D decays. *Phys. Rev.*, D86:014023, 2012.

[20] F. Buccella, M. Lusignoli, G. Miele, A. Pugliese, and P. Santorelli. Nonleptonic weak decays of charmed mesons. *Phys. Rev.*, D51:3478–3486, 1995.

[21] N. Cabibbo. Unitary symmetry and leptonic decays. *Phys. Rev. Lett.*, 10:531–533, Jun 1963.

[22] H.-Y. Cheng and C.-W. Chiang. Direct CP violation in two-body hadronic charmed meson decays. *Phys. Rev.*, D85:034036, 2012. [Erratum: Phys. Rev.D85,079903(2012)].

[23] H.-Y. Cheng and C.-W. Chiang. SU(3) symmetry breaking and CP violation in D -> PP decays. *Phys. Rev.*, D86:014014, 2012.

[24] J. H. Christenson, J. W. Cronin, V. L. Fitch, and R. Turlay. Evidence for the 2π Decay of the K^0_2 Meson. *Phys. Rev. Lett.*, 13:138–140, 1964.

[25] N. Dash et al. Search for CP Violation and Measurement of the Branching Fraction in the Decay $D^0 \to K^0_S K^0_S$. *Phys. Rev. Lett.*, 119(17):171801, 2017.

[26] M. Golden and B. Grinstein. Enhanced cp violations in hadronic charm decays. *Physics Letters B*, 222(3):501 – 506, 1989.

[27] Y. Grossman, A. L. Kagan, and Y. Nir. New physics and CP violation in singly Cabibbo suppressed D decays. *Phys. Rev.*, D75:036008, 2007.

[28] Y. Grossman, A. L. Kagan, and Y. Nir. New physics and CP violation in singly Cabibbo suppressed D decays. *Phys. Rev.*, D75:036008, 2007.

[29] T. Head. The LHCb trigger system. *Journal of Instrumentation*, 9(09):C09015–C09015, sep 2014.

[30] W. D. Hulsbergen. Decay chain fitting with a kalman filter. *Nuclear Instruments and Methods in Physics Research Section A: Accelerators, Spectrometers, Detectors and Associated Equipment*, 552(3):566 – 575, 2005.

[31] M. Kobayashi and T. Maskawa. CP-Violation in the Renormalizable Theory of Weak Interaction. *Progress of Theoretical Physics*, 49(2):652–657, 02 1973.

[32] W. K. Lai, A. K. Leibovich, and A. A. Petrov. $D^{\pm}$ production asymmetry at the lhc from heavy quark recombination. *Phys. Rev. D*, 90:054022, Sep 2014.

[33] F. Lazzari. Development of a real-time tracking device for the LHCb Upgrade 1b, Nov 2017. Presented 13 Dec 2017.

[34] S. Müller, U. Nierste, and S. Schacht. Topological amplitudes in D decays to two pseudoscalars: A global analysis with linear $SU(3)_F$ breaking. *Phys. Rev.*, D92(1):014004, 2015.

[35] U. Nierste and S. Schacht. CP Violation in $D^0 \to K_S K_S$. *Phys. Rev.*, D92(5):054036, 2015.

[36] A. D. Sakharov. Violation of CP Invariance, C asymmetry, and baryon asymmetry of the universe. *Pisma Zh. Eksp. Teor. Fiz.*, 5:32–35, 1967. [Usp. Fiz. Nauk161,no.5,61(1991)].

[37] A. Soni. Resonance enhancement of Charm CP. 2019.

[38] M. Tanabashi et al. Review of particle physics. *Phys. Rev. D*, 98:030001, Aug 2018.

[39] G. Tuci. Measurement of the time-integrated CP asymmetries in $D^0 \to K_S^0 K_S^0$ decays. 2017. http://www.infn.it/thesis/PDF/getfile.php?filename=11761-Tuci-magistrale.pdf.

[40] G. Tuci. Measurement of the time-integrated CP asymmetry in $D^0 \to K^0_{\mathrm{S}} K^0_{\mathrm{S}}$ decays with LHCb. *PoS*, BEAUTY2018:061, 2018.

[41] L. Wolfenstein. Parametrization of the kobayashi-maskawa matrix. *Phys. Rev. Lett.*, 51:1945–1947, Nov 1983.

[42] C. S. Wu, E. Ambler, R. W. Hayward, D. D. Hoppes, and R. P. Hudson. Experimental Test of Parity Conservation in Beta Decay. *Phys. Rev.*, 105:1413–1414, 1957.

Ringraziamenti

Il primo dovuto ringraziamento va al Prof. Giovanni Punzi e a Giulia Tuci, che mi hanno guidato con dedizione e pazienza durante il percorso di tesi di questi ultimi mesi, senza i quali sarebbe stato impossibile realizzare il lavoro qui esposto, fonte per me di grande orgoglio e soddisfazione.
Questo rappresenta anche la conclusione del mio personale percorso di laurea, che sono riuscito ad affrontare solo grazie a tutti coloro che ho avuto vicino in questi anni e che meritano dunque un pensiero speciale.
Le prime persone che voglio ringraziare sono quelle a cui questa tesi è dedicata, cioè i miei genitori; se sono riuscito a raggiungere questo traguardo e a crescere fino a diventare la persona che sono è in gran parte merito loro. Li ringrazio per avermi permesso di seguire le mie più alte aspirazioni senza mai opporre alcuna opposizione, nonostante ciò mi portasse lontano da casa e da loro; li ringrazio per avermi sempre accolto a braccia aperte e con il sorriso a qualunque ora del giorno e per aver sopportato i miei continui malumori, dandomi sempre il sostegno di cui avevo bisogno. Li ringrazio soprattutto per aver fatto tutto ciò senza mai lasciar trasparire il peso dei loro sforzi e sacrifici. Un grazie speciale non può essere negato ai sempre invidiabili pasti portati ad ogni ritorno a Pisa (dedica a cui credo vogliano aggiungersi i miei coinquilini).
Questi pensieri vanno estesi anche a mio fratello Jacopo, a Silvia e alla piccola Sofia, per avermi sempre fatto sentire il calore di casa ogni volta che fossi tornato e soprattutto a distanza di molti chilometri, grazie alle loro parole e ad ogni piccolo gesto.
Un gigantesco grazie va a Laura, che mi tiene per mano da prima dell'inizio di questo percorso e che considero ormai una parte integrante di quello che sono. La ringrazio per essermi stata vicina ed avermi aiutato ad affrontare gli infiniti ostacoli che mi sono trovato a dover superare, per aver sopportato con pazienza la distanza che ci ha tenuti separati per lunghi periodi e per essere sempre stata la mia prima confidente e fidata compagna di viaggio, senza la quale sarei stato, e sarei tutt'ora, perso.
Sono in debito anche con i ragazzi con i quali ho convissuto durante questi anni, Luca e Matteo, e poi Donato, Matteo e Paolo, che con la loro compagnia sono sempre riusciti ad alleggerire qualunque pessima giornata mi fosse toccata e senza i quali questo periodo sarebbe indubbiamente stato più grigio e vuoto.
Lo stesso si può dire per tutti coloro che sono stati miei colleghi e amici durante tutto il percorso universitario. Li ringrazio per aver condiviso, a tratti in completa simbiosi, le innumerevoli ore di studio, di lezione e di laboratorio, i molti traguardi raggiunti, le continue corse a mensa e le bellissime serate passate fra quattro mura, ma con le persone giuste. Sentirò la mancanza di tutto ciò e mi sento fortunato ad averli incontrati.
Gli altri compagni di viaggio che voglio ringraziare sono quelli che sono stati miei colleghi al Fermilab, che in brevissimo tempo si sono subito trasformati in preziosi amici. Nei due mesi passati insieme si è creata un'atmosfera magica e non c'è stato un giorno in

cui non mi abbiano fatto crescere; li ringrazio per avermi insegnato come sia possibile e semplice, essere intraprendenti, caparbi, ottimisti e soprattutto per avermi regalato quello che, senza dubbio, rimarrà uno dei periodi più belli della mia vita.
Ultimo ringraziamento, ma non meno importante, va a tutti i miei amici, sparsi per Gualdo, Perugia, Roma, Firenze, Pisa, Venezia, Delft, con i quali sono cresciuto e continuo a condividere i momenti più belli e importanti; a loro va un grazie di cuore semplicemente per essere miei amici e per regalarmi divertimento, conforto e calore ad ogni occasione.